Supramolecular Self-Assembly with Precisely Control and Potential Biological Application

by

HENG LI

A thesis submitted to the University of Birmingham

for the degree of DOCTOR of PHILOSOPHY

School of Chemistry
College of Engineering and Physical Sciences
University of Birmingham
January 2022

Abstract

Self-assembly is one of the most interesting phenomena in the field of life science. Inspired by life system, taking advantage of non-covalent interaction to construct artificial self-assembly systems with different functions has become a hot topic in interdisciplinary research. This work is devoted to the design and synthesis of new building blocks based on BCPs or amino acid to build 1D chiral and 2D platelet micelles with controllable morphology and exploring the potentially biology and optoelectronics application.

In chapter 2 and 3, block copolymers of PPV-*b*-P2VP were employed as building units for supramolecular self-assembly. By the introduction of chlorine, morphological transformation from rod-like micelles to diamond-like micelles was achieved by the thermally induced nucleation process that lets the kinetically trapped 1D nanostructures to transform as the 2D nanostructures in the thermodynamic state. Then the crystalline groups as TIPS group was introduced into the copolymers, which caused the morphology transition from 2D square to rectangular or rod-like micelles with controllable aspect ratios. These nanomaterials with controllable shapes that possess fluorescent and semiconducting properties could be potential candidates for biological and optoelectronics applications.

Chapter 4 and 5 describes the study of amino acid derivatives based on thiophene core with different amino acid arms as building blocks. After supramolecular self-assembly, the helices with controllable chirality and 2D rectangular microsheets were obtained. In addition, by utilizing co-assembly, helicity appearance and inversion were observed for the TDAP-MA system, which was used to provide a feasible detection approach for melamine.

Acknowledgments

My first and deepest thanks go to my two supervisors, Prof. Feng He and Dr. Paco Fernández-Trillo, who supported my journey during these four years. Both of you have provided me with much discrete guidance, appreciated support, and helpful advice. Your help were significant for stopping me from following some of my wrong ideas, and for keeping me on track. It's been a pleasure to work with both of you.

I also want to thank my colleagues and particularly Liang Han for enduring my various questions and weird ideas. Your detailed advices and the frequent discussions between us helped me in broadening my research thought and attempting a lot of novel experiments, and for that I sincerely thank you. I want to express my gratitude to all the other colleagues in Feng's group for all the three challenging years we've spent together, your detailed suggestions and kind help no matter in the lab and daily life, including Yulin Zhu, Qing Li, Hengtao Wang, Hanjian Lai, Yan Li, Pu Tan, Mingrui Pu, Hui Chen, Chunxian Ke, and Tingxing Zhao. It was a pleasure to have you all alongside me during my PhD journey.

Moreover, I would also like to thank the colleagues from Paco's group in UK, Oliver, Sameh, Zelu, Carlos, Tom, Alex, and Teyfik. You make me feel easier to work and live in UOB, and I'm profoundly grateful to you all for the help given to me in our time spent together.

I am grateful to the SUSTech for the funding for my PhD tuition and research. In the same way I owe acknowledgements to the SUSTech Core Research Facilities for the AFM, TEM and SEM measurements.

At last, I want to express the deepest gratitude to my family, the one I was born within and my future one. I could not finish at the end of the journey without the support of my parents, who have been always encouraging and supportive throughout the whole PhD path. At last, I want to

thank Mrs. Jiajing, who always help me deal with the illustrated figure in the paper and helped me go through the difficulties of life and work during these last four years.

List of Publications

Published

1. **Li, H**.; Han, L.; Zhu, Y.; Fernández-Trillo, P.; He, F., **Transformation from Rod-Like to Diamond-Like Micelles by Thermally Induced Nucleation Self-Assembly**. *Macromolecules* 2021, 54 (11), 5278-5285.

2. **Li, H.**, Han, L., Li, Q., Lai, H., Fernández-Trillo, P., Tian, L. and He, F., **Hierarchical Chiral Supramolecular Nanoarchitectonics with Molecular Detection: Helical Structure Controls upon Self-Assembly and Coassembly.** *Macromol. Rapid Commun*. 2021, 2100690.

Submitted

1. **Li, H**.; Han, L.; Zhu, Y.; Zheng, N.; Fernández-Trillo, P.; He, F., **Morphological Transition and Transformation of 2D Platelets by Controlling Balance of π−π Stacking Interaction and Crystalline Driven Force**. *Mater. Horizons* Major revised 2022.

In preparation

1.**Li, H.**, Han, L., Li, Q., Lai, H., Fernández-Trillo, P., Tian, L. and He, F., **Morphologically Tunable Rectangular Microsheets and Microsaws Constructed by Hierarchical Self-assembly based on Hydrogen Bonds.** *Macromol. Rapid Commun*. Accepted 2022.

Table of Contents

Chapter 1 Introductions……...…1

1.1 Overview of self-assembly……...1

1.1.1 Self-assembly behavior in solutions…….....1

1.1.2 Self-assembly of BCPs…….…2

1.1.3 Challenge and significance of 2D materials by assembly of BCPs…..…5

1.2 Preparation of assemblies based on BCPs……...7

1.2.1 Preparation approaches based on the amphiphilic polymer……....7

1.2.2 Influence factors of assembled morphology……...8

1.3 Supramolecular self-assembly based on small molecules…….…….……13

1.3.1 Overview of supramolecular self-assembly……...…...…….13

1.3.2 The driving force of supramolecular assembly…….14

1.4 Chiral supramolecule based on self-assembly…….……..18

1.4.1 Introduction of chirality……18

1.4.2 Approaches to obtain supramolecular chirality…….20

1.4.2.1 Chiral assembly by chiral molecules.....22

1.4.2.2 Chiral co-assembly with chiral molecules and achiral molecules.23

1.4.2.3 Chiral assembly by achiral molecules……..24

1.5 Aim and outline of the thesis……..26

1.6 Reference……...28

Chapter 2 Transformation from Rod-like to Diamond-like Micelles by Thermally Induced Nucleation Self-assembly…….38

2.1 Abstract……39

2.2 Introduction……..40

2.3 Materials and methods……43

2.3.1 Materials……..43

2.3.2 Experimental methods……....43

2.4 Results and discussion…….49

2.4.1 Formation of 1D rod-like micelles and preparation of fragment micelles……..49

2.4.2 Formation of 2D diamond-like micelles by thermally induced nucleation self-assembly…….……50
2.4.3 Energetics of the transformation from 1D rod-like micelles to 2D diamond-like micelles……...55
2.4.4 Tuning the scale of the diamond-like micelles by varying the unimer/seed ratio……59
2.5 Conclusions……..62
2.6 Reference…….62
Chapter 3 Morphological Transition and Transformation of 2D Platelets by Controlling Balance of π−π Stacking Interaction and Crystalline Driven Force…….…..67
3.1 Abstract……68
3.2 Introduction……..69
3.3 Materials and methods…….71
2.3.1 Materials……..71
2.3.2 Experimental Methods……...71
3.4 Results and discussion…….75
3.4.1 Design and preparation of PPV-TIPS BCP micelles……75
3.4.2 Effect of the P2VP chain length on the morphology transition……77
3.4.3 Tuning the morphology of the 2D micelles by varying solution concentrations……79
3.4.4 Growth process and mechanism of the formation of the 2D platelet micelles……..82
3.4.5 Heterogenous co-assembly based on crystallization and π−π interaction……..87
3.5 Conclusions……..90
3.6 Reference…….90
Chapter 4 Hierarchical Chiral Supramolecular Nanoarchitectonics with Molecular Detection: Helical Structure Controls upon Self-Assembly and Co-Assembly……..…94
4.1 Abstract……95
4.2 Introduction……..96
4.3 Materials and methods…….98

4.3.1 Materials……....98
4.3.2 Experimental methods……...98
4.4 Results and discussion……...101
4.4.1 Hierarchical self-assembly of TDAP……101
4.4.2 Spectroscopic characterization of the chiral helices……103
4.4.3 Exploring the mechanism and stoichiometry of chiral assembly…...…104
4.4.4 Molecular detection of melamine……...106
4.5 Conclusions……....109
4.6 Reference……...109
Chapter 5 Morphologically Tunable Rectangular Microsheets and Microsaws Constructed by Hierarchical Self-assembly based on Hydrogen Bonds……112
5.1 Abstract……..113
5.2 Introduction……114
5.3 Materials and methods……...116
5.3.1 Materials……116
5.3.2 Experimental methods……..116
5.4 Results and discussion……...119
5.4.1 Synthesis and self-assembly of TDAV……..119
5.4.2 Tuning the morphology of 2D micelles by controlling water content ……....121
5.4.3 Effect of chirality on the morphology 2D platelet……..123
5.5 Conclusions……..…..126
5.6 Reference……..126
Appendix A Supplementary Information for Chapter 2……131
A.1 Supplementary data……...131
Appendix B Supplementary Information for Chapter 3……140
B.1 Supplementary methods……140
Appendix C Supplementary Information for Chapter 4……150
C.1 Supplementary data……...150
Appendix D Supplementary Information for Chapter 5……160
D.1 Supplementary data……...160

List of Figures

Figure 1.1.1 Typical structures of block copolymers containing two types of blocks.....3
Figure 1.1.2 Schematic illustration of BCP self-assembly to form various core–shell nanoparticles with morphologies that are dependent on the self-assembly conditions and polymer composition.....5
Figure 1.1.3 Schematic representation and probable molecular packing of the 2D square micelles formed by self-assembly of BCPs based on PPV……..….7
Figure 1.3.1 Self-assembly of monomer with a UPy unit via complementary quadruple hydrogen bonding.....15
Figure 1.3.2 Energy-minimized models (molecular mechanics with charge-equilibration)…….16
Figure 1.3.3 Schematic illustration for the formation of hydrogel and nanovesicle from multiple noncovalent interactions.....17
Figure 1.4.2 Method for obtaining supramolecular chirality in supramolecular assembly system…….....22
Figure 1.4.3 Nucleation-elongation of one type of chiral molecule to form 1D helical to super-helical structures.....23
Figure 1.4.4 Molecular model showing three dimers aligned end-to-end within the minor groove of a DNA template.....24
Figure 1.4.5 Alkylamines of different lengths are assembled into helical and massive structures with cyclodextrin through host-guest interaction……...25
Figure 1.4.6 The self-assembly supramolecular chirality of bent bridging ligands coordinated with silver ion.....26
Figure 1.4.7 Achiral C_3-symmetric monomer self-assembly into nanostructure with controlled homochiral by vortex mixing and ageing.....27
Figure 2.1 Transmission electron microscopy (TEM) images of 1D rod-like micelles of (PPV-$Cl_{20\%}$)$_{10}$-*b*-P2VP$_{20}$ prepared from isobutanol solutions with different concentrations……...51
Figure 2.2 Schematic representation and TEM images of thermally induced nucleation growth process formed at 50 °C after aging for different hours…….52

Figure 2.3 TEM images of 2D diamond-like micelles prepared from (PPV-$Cl_{20\%}$)$_{10}$-*b*-P2VP$_{20}$ at different annealing temperatures in isobutanol.……54
Figure 2.4. AFM height images of 2D diamond-like micelles formed at different annealing temperatures in isobutanol.…….……55
Figure 2.5 Proposed transformation from 1D rod-like micelles to 2D diamond-like micelles by the thermally induced nucleation self-assembly process involving (PPV-$Cl_{20\%}$)$_{10}$-*b*-P2VP$_{20}$, and the energetics schematic diagram of the self-assembly……....57
Figure 2.6 TEM images of 2D diamond-like micelles prepared from (PPV-$Cl_{20\%}$)$_{10}$-b-P2VP$_{20}$ formed from different m_{unimer}/m_{seed} ratios……..62
Figure 3.1 TEM images of 2D micelles prepared from 0.005 mg ml^{-1} isopropanol solution of PPV-TIPS-*b*-P2VP……..…79
Figure 3.2 TEM images of 2D rectangular micelles prepared from isobutanol solution of PPV$_5$-TIPS-*b*-P2VP$_{10}$…….….81
Figure 3.3 TEM images of 2D rectangular and rod-like micelles prepared from PPV$_5$-TIPS-*b*-P2VP$_{20}$ at different concentrations in isopropanol……82
Figure 3.4 AFM height images of 2D square and rectangular micelles formed from PPV-TIPS-*b*-P2VP with different block ratios in isobutanol.……..…..83
Figure 3.5 XRD patterns of PPV$_5$-TIPS-CHO, the optimized structures and calculated scales of PPV$_5$-TIPS-CHO by DFT calculations, and 2D GIWAXS patterns……..…85
Figure 3.6 Probable structures of the one-dimensional fiber-like PPV monolayer packing model, proposed growth process of 2D micelles by self-assembly process, and morphological transition by different growth rates……....87
Figure 3.7 TEM images of 2D circular disk-like micelles based on co-assembly with PPV$_{12}$-*b*-P2VP$_{12}$ and PPV$_5$-TIPS-*b*-P2VP$_{10}$ at a 0.005 mg·mL^{-1} solution……...90
Figure 4.1 SEM images of racemic, *R*-, *S*-, and *R*+*S*-TDAP assembled architectures prepared in isopropanol/H_2O mixtures……...…….……103
Figure 4.2 CD spectra for *S*-, *R*-, racemic, and *R*+*S*-TDAP……...104
Figure 4.3 Single-crystal structures of *S*-TDAP and *R*-TDAP……106
Figure 4.4 SEM images of MA/*R*-TDAP-COOH, *R*-TDAP-COOH and CA/ *R*-TDAP-COOH assembled architectures.…….…….……108
Figure 4.5 SEM images of TDAP/MA at different molar ratios……109

Figure 5.1 SEM images and contour length distributions of 2D micelles……....121
Figure 5.2 SEM images 2D and 1D micelles prepared from R-TDAV in 0.5 mg ml^{-1} cosolvents solution and single-crystal structures of S-TDAV……..…122
Figure 5.3 SEM images of different micelles and XRD pattern…….124

List of Abbreviations

1D	One dimensional
2D	Two dimensional
A_c	Area per corona chain on the core surface
AFM	Atomic force microscopy
BCP	Block copolymer
CA	Cyanuric acid
CD	Circular dichroic spectrum
CDSA	Crystallization-driven self-assembly
CMC	Critical micelle concentration
CWC	Critical water content
DFT	Density functional theory
DLS	Dynamic light scattering
DSC	Different scanning calorimetry
DMF	Dimethyl Formamide
G	Gibbs free energy
GIWAXS	Grazing Incidence Wide-angle X-ray Scattering
GPC	Gel Permeation Chromatography
LC-MS	Liquid chromatography-mass
MA	Melamine
N_{agg}	Number of aggregates、
NMR	Nuclear magnetic resonance

P2VP	Poly (2-vinyl pyridine)
PAA	Poly (acrylic acid)
P3HT	Poly (3-hexylthiophene)
PEG	Poly (ethylene glycol)
PFS	Polyferrocenylsilane
PS	Polystyrene
PPV	Poly (p-phenylenevinylene)
$\mathbf{R_{core}}$	Number-average core radius
SA	Self-assembly
$\mathbf{S_c}$	Stretching degree of Chains
SEM	Scanning electron microscopy
TIPS	Triisopropylsilyl
TEM	Transmission electron microscopy
THF	Tetrahydrofuran
UV-Vis	UV-Vis Absorption Spectra
XRD	X-ray diffraction

CHAPTER 1 INTRODUCTION

1.1 Overview of self-assembly

Self-assembly is used to indicate basic structural units spontaneously forming an ordered structure under non-covalent interactions.[1] Supramolecular self-assembly is universal in human life as well as nature. For example, the cell membrane of the organism is assembled by phospholipid molecules; the soap bubbles are formed by assembly with molecular surfactants when using soap. These interesting phenomena have stimulated people's interest in the self-assembly field. The structure of the material plays a decisive role in the application of the material, so it is very important to develop materials with new structures. The research on self-assembly is the basis of the development of new materials with specific properties and new applications.[2] Block copolymers (BCPs), biological small molecules, and homopolymers all can be considered as the building block, which can spontaneously assemble into supramolecular order architectures with various structures through non-covalent interactions under the certain conditions. Among them, different blocks with various properties of the BCPs have a wide range of applications in medicine, optical storage, energy, and other high-tech fields.[3-5] In addition, the study of supramolecular self-assembly based on small molecules has also attracted the attention of scholars in the domains of chemistry, physics, and material science in recent years. In this work, PPV-based BCPs and functional small molecules are used as the main building blocks, and we present a series of meaningful research works.

1.1.1 Self-assembly behavior in solutions

Although the synthesis of small molecules and macromolecules has reached an advanced state, preparing materials in the 10 nm to 100 μm size range with controlled scale, function, and hierarchical architecture is still interesting and promising. Self-assembly, as a significant approach, is applied to construct ordered and meaningful structures in nature and is gradually significant in the field of modern material science. Supramolecular self-assembly is based on noncovalent interactions, like hydrophobic interactions, hydrogen bonds, and π-π stacking to design functional materials with tailored properties.[3] In decades of researches, the molecular self-assembly based on amphiphilic molecules has been intensively studied, and the understanding of the assembly behavior has been very good. From the 1860s, people had begun to largely study self-assembly. So far, self-assembly of ontology based on BCPs has been widely known by people. There are a large number of professional books and literature reviews introduces the related content. [4-7] The research of self-assembly in the solution based on the BCPs started late. In 1995, Bisenberg's group from McGill University in Canada reported the solution self-assembly behavior of BCPs resulting in multiple morphologies for the first time.[8] Since then, self-assembly in the solution has attracted widespread attention and became a popular research area in these 20 years.

1.1.2 Solution self-assembly based on block copolymers

Using block copolymer to assembly in solution is a significant approach in the field of self-assembly.[2] Recently, this kind of macromolecular self-assembly is extensively and deeply researched, and assemblies with controllable structure, morphology, and performance could be achieved through effectively controlling molecular assembly behavior.[9-12] It was demonstrated that these assemblies have good application prospects in many fields such as drugs or biologically active substances, the loading of optical, electrical, magnetically active substances, and the preparation of nanomaterials.[13-20] Among these, self-assembly based on BCPs is a significant

research field. Block copolymers are usually synthesized through covalent bonding, and consist of two or more homopolymers with different properties which are usually chemically incompatible, such as hydrophily and hydrophobicity. Figure 1.1.1 shows the different structures of BCPs including several types of blocks, A and B, containing di-block AB copolymers, ABA or BAB tri-block copolymers, alternating copolymers, and tapered copolymers.[21] Among these, AB di-block copolymer can be considered as scaled-up small molecular surfactants. The principle of self-assembly based on these amphiphilic BCPs are similar to that of amphiphilic small molecules, which is the research focus of supramolecular self-assembly.

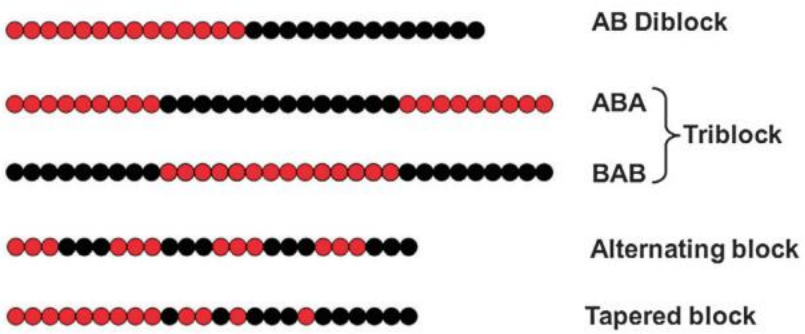

Figure 1.1.1 Typical structures of BCPs including two types of blocks, A and B.[21]

For the case of assembly behavior based on BCPs in solutions, when in a good solvent, BCPs consisting of hydrophilic block and hydrophobic block generally maintain their incompatibility of different segments. When adding the selective solvent such as water, hydrophobic interactions drive the hydrophobic block to aggregate and hydrophilic chains keep the stability of BCPs in the solutions. This aggregation process involves the morphological transformation of intermediate assemblies. Understanding the relationship between thermodynamics and kinetics in the polymeric self-assembly can help us achieve the intermediate aggregate in the morphological transformation of thermodynamic equilibrium, which will reveal the mechanism of morphological transformation. The entropy of some polymer chains will be consumed in the entire assembly process, but the

enthalpy of the interaction between the hydrophobic segment and water is reduced to a greater extent in the meantime, which reduces the Gibbs free energy of the system ($G<0$). For the case where polymer chains are not fixed in the self-assembly process, the resulting aggregation is thermodynamically controlled, so the standard thermodynamic variables are very important. In an aqueous solution, the polymer chain will undergo hydrophobic hydration, which means that the water molecules are arranged around the hydrophobic segment of the copolymer in an orderly manner. The ordered arrangement of water molecules is broken in the formation of aggregation based on the copolymer chain, resulting in the increase of entropy. The longer the hydrophobic chain, the more water molecules arranged around hydrophobic chains. Therefore, when the longer chain aggregates, more water molecules will be released and the increase of entropy will be more, leading to the decrease of totally free energy in the system.[22]

In most cases, amphiphilic BCPs easily undergo self-assembly to construct core-shell nanoparticle micelles when were added to a selective solvent for one specific block. [23-25] The core of the micelle consists of hydrophobic segments, and the hydrophilic segments have been solvated to form a shell around the core, in order to maintain the stable existence of the micelles in the solution.[26] These micelles are strong and have been very well-studied. Among these, polystyrene-*b*-poly (acrylic acid) (PS-*b*-PAA), as a classic case, has been shown in the formation of a series of micelles with different shapes, which have a PS core and a PAA corona in the solution system. These resultant structures include vesicles, spheres, 2D lamella assemblies, cylinders, and other examples on account of the assembled conditions and block ratio.[27] The important properties of the self-assembly based on BCPs are that the resulting nanoparticles are in the kinetically trapped state; exchange of BCP molecules among the micelles is slow or non-existent. Therefore, it is much harder to predict the formed morphologies of the nanoparticles because the packing

parameter approach cannot work well and they often belong to non-equilibrium structures.[28] In addition, because of the kinetically-trapped characteristics, the same BCP molecule can even result in various morphologies by using different assembled conditions.[29]

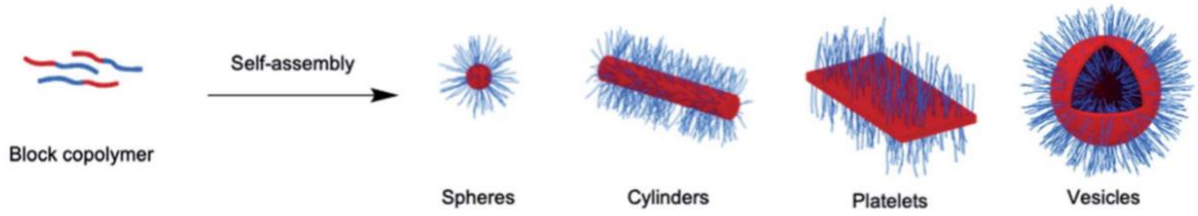

Figure 1.1.2 Schematic diagram of block copolymer self-assembly to form various core-shell nanoparticles with various morphologies under the different assembly conditions.[30]

1.1.3 Challenge and significance of 2D materials by the assembly of BCPs

Although micelles based on BCPs are very promising in many fields, efforts to realize their applications have been subjected to several problems. These issues include how to obtain micelles with non-spherical morphology, limited ability to form complex micellar particles from BCPs in a predictable and controlled fashion, and the scale-up of BCP micelles. Among these, the morphology of BCP assemblies as non-spherical is highly challenging.[28] Driven by thermodynamics, ordered architectures are spontaneously achieved through chemical incompatibility related to block size. Many attentions and experimental studies reveal that 2D micellar platelet can have important advantages over the hollow and solid spherical counterparts for a series of applications, such as using as support for catalysis, [31] nanowires in optoelectronic devices, [32] and the delivery of therapeutic agents. Among these intermolecular driven forces of assembly, crystallization-driven interactions play a key role in the self-assembly approaches to preparing 2D assembled structures, so the morphologies of the resulting 2D architectures are controlled through the symmetry of the unit cell. The assembly based on BCPs with the crystalline core inclines to form uniform 2D platelet structures with a range of morphologies, for example,

square,[33] equilateral triangular, diamond, hexagon,[34] and circular assemblies. Recently, a wide range of analogous BCPs have been employed for 2D self-assembly and 2D well-defined nanostructures were formed in solution. For example, the groups of Manners[35] and Winnik[36] have fabricated a variety of 2D nanomaterials with hierarchical structures through self-assembly by using polyferrocenylsilane (PFS)-based BCPs with crystalline. These classic BCPs were used to produce interesting 2D rectangular or lenticular platelet possessing semi-crystalline features through a seeded growth process.[36] In addition, achieving 2D uniform nanostructures of BCPs consisting of the core with low or zero crystalline properties through other driving forces, like hydrophilic or hydrophobic interactions, π–π interactions, Van der Waals' forces, and H-bonds, is also promising and challenging. For these copolymer blocks with amorphous core, non-spherical nanoparticle micelles are only produced under some specific self-assembly conditions or BCP compositions. Among this kind of polymers, poly(p-phenylenevinylene) (PPV), as a classic example of π-conjugated material, possesses fascinating optical and electronic properties. PPV with the long conjugated backbones tends to cause tight intermolecular stacking[37-38] with strong sheet-forming assembling inclination. Therefore, PPV-based BCPs have been widely used as building blocks for supramolecular self-assembled 1D cylinders or fibers.[39-40] Recently, He's group has reported using PPV-*b*-P2VP to fabricate 2D micelles with different morphologies of square, scarf, rhombic, and diamond micelles by SA methods.[33, 41-42] It revealed that different alkyl chains at PPV core and the length of P2VP cause the difference of morphology. Among these 2D micelles, the rhombic materials were applied in pressure sensing devices on rigid as well as flexible substrates with vertical tunneling, which showed high sensitivity, high on-state current density (6000 A cm^{-2}), and the on-off current ratio of more than 10^4. [42]

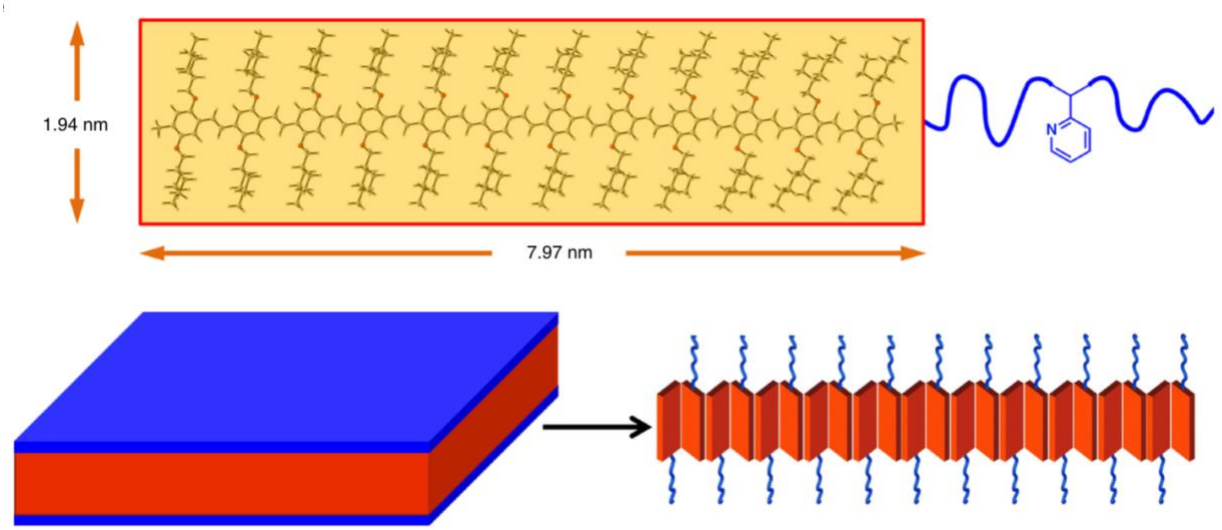

Figure 1.1.3 Schematic illustration of molecular packing of 2D platelets formed by bottom-up assembly with PPV.[33]

1.2 Preparation of assemblies based on BCPs

1.2.1 Preparation approaches based on the amphiphilic polymer

Preparation methods always lie on the nature and properties of the BCPs. For hydrophobic chains of BCPs whose glass transition temperature (the temperature corresponding to the transition from the glassy state to the highly elastic state) is higher than the room temperature, the cosolvent approach is usually applied to prepare the assemblies such as PS-*b*-PAA (glass transition temperature of PS is around 110℃).[21] Firstly, the diblock copolymer was dissolved in cosolvent at a low concentration (less than 2 wt%). The cosolvent should dissolve the hydrophobic and hydrophilic chains of BCPs and also dissolve the precipitant for the hydrophobic blocks (like water). Then the precipitant is slowly added, which would hinder the dissolution of the hydrophobic segment. When the water content increases to a certain concentration (the critical water content, CWC), PS segment begins to aggregate into the core of the micellar sphere, because of the existence of the hydrophilic segment preventing further increase of the micellar size. Usually,

when the water content is around 25 wt %-50 wt %, water is no longer added (water content depends on the cosolvent property). In this range of water content, for similar hydrophobic chains like PS, these chains in the hydrophobic part of the aggregate are "frozen", which means that the morphology will not change in the short term. Finally, the aggregation solution is quickly poured into a lot of water (usually 5-10 times the weight of the aggregation solution) to fix the final morphology, which is called quenching. Then the solvent is removed through the dialysis method, to achieve the pure aggregate of water solution.

The aggregation of amphiphilic BCPs will occur only above a certain concentration, which is regarded as the critical micelle concentration (CMC). The single polymeric molecule is dissolved in solution in the formation of a single molecular chain below the CMC. Molecular weight, relatively molecular length, and the property of BCPs all affect the CMC. For homopolymers, the higher the molecular weight, the higher the unit number of insoluble chains, the lower solubility limit is. When the length of the insoluble block increases, the interaction with the solvent is stronger, resulting in the precipitation of the polymer. The diblock BCPs have the similar effect. The higher the molecular weight with the same length of soluble chain, the lower the CMC is. When the insoluble chains begin to aggregate, the soluble blocks prevent the precipitation and the micellization process replaced the precipitate process.

1.2.2 Influence factors of assembly morphology

There are a variety of morphologies in the BCP aggregations. A large number of researches proved that the morphology of micelles based on BCPs is determined by the free energy of the system which is subject to three kinds of force balance, [13, 23] including the stretch extent of nucleation segment, interfacial energy between core and shell, and repulsion forces among the shell segment. So far, many factors have been found to affect the morphology of aggregates,

including the compositions of the BCPs, the concentration, the compositions and properties of the solvent, additive, and temperature. In this section, we take the PS-*b*-PAA system as an example to discuss the effects of these factors on the morphology of aggregation.

PS-*b*-PAA	PAA (mol%)	Morphology
410-*b*-46	10.1	Spheres
200-*b*-21	9.5	Spheres
200-*b*-15	7.0	Rods
410-*b*-25	5.9	Rods
410-*b*-20	4.7	Vesicles
200-*b*-8	3.8	Vesicles
200-*b*-4	2.0	LCMs

Table 1.2 Different morphologies based on PS-*b*-PAA copolymers in the cosolvent. [21]

Firstly, the composition of the BCPs is an important factor affecting the morphology of the aggregation in the BCP solution. Table 1-2 shows the common aggregation morphology of PS-*b*-PAA and the mole fraction (or volume fraction) of the PAA chain. With the decrease in mole fraction of the PAA chain segment, the morphology of aggregates transforms from spherical aggregates into cylindrical aggregates and vesicles, eventually into large composite micelles. Normally, PS-*b*-PAA copolymer with a larger volume fraction of PAA formed spherical micelles. In micelles, three parameters related to the degree of polymerization of BCP segments are the degree of stretching of PS chains (S_c), the number-average core radius (R_{core}), and the area per corona chain on the core surface (A_c), which play the key role in the resulting morphology. Based on experimental data, the relationship of these three parameters with the polymer composition are given by following equations, for micellar spheres with PS-*b*-PAA forming in mixtures of DMF and water.[11] In this situation, N_{PAA} and N_{PS} are the degrees of polymerization (the chain lengths) of both the PAA block and the PS block, respectively. The PS segments are stretched from the interface of corona-core to the center in the micelle core. In the case of micelles with the same PS

block length, S_c increases as the increasing R_{core}, which also is suitable for vesicles, cylinders, and lamellae. In general, the PS block in the micellar spheres is more stretched than the chain of cylindrical aggregates, in which they are more stretched than in the vesicle and lamellar micelles. In the case of BCPs with the longer chain length of PAA and the same length as PS, BCPs are easy to form spherical micelles, because of the larger A_c in the core-shell interface of spherical micelles. This means longer PAA chain has larger space in the shell resulting in the lesser repulsive force, which can reduce freedom energy of the system. When the length of PAA decreases, the core size and the S_c increase. However, the stretch of PS chain will be restricted by entropy and the decrease of A_c increase the repulsion between PAA chain, which increases the free energy of the system. Therefore, the increase in the radius of the micelle core will be reversely restricted by the S_c and A_c. The chain length of the PAA continues to decrease, then S_c and A_c become the dominant factor. To reduce the repulsion between the PAA chain and the extension of the PS segments, spherical micelles accordingly transform into cylindrical micelles, lamella structures, and even vesicles.

$$R_{core} \sim N_{PS}^{0.4} N_{PAA}^{-0.15}$$

$$S_c \sim N_{PS}^{-0.1} N_{PAA}^{-0.15}$$

$$A_c \sim N_{PS}^{0.6} N_{PAA}^{0.15}$$

Secondly, the concentration of copolymer in the cosolvent plays a key role in the resulting morphology. For example, as the concentration of the PS_{190}-*b*-PAA_{20} in DMF was changed from 1% to 3.5%, the architectures of the aggregations would transform from spherical micelles, to columnar micelles, to vesicles after adding the same amount of water.[43] The influence of concentration can be understood from the perspective of a number of aggregates (N_{agg}). The research based on the self-assembly of molecular surfactants proves that the relationship between N_{agg} and C (molecular concentration) is calculated by $N_{agg}=2(C/CMC)^{1/2}$, which also applies to

polymer. N_{agg} increases as the increasing concentration, which results in the increase of core size and extension of the chain in the core. Therefore, as the polymer concentration increases, the morphological transformation from spherical micelles to columnar micelles can be observed.

Thirdly, temperature also affects the morphology of aggregation. Like adding water into the assembly systems, changing the temperature has an obvious effect on the polymer-solvent parameter. Researchers used alcohols such as methanol, ethanol, 2-propanol, and butanol as studied objects.[44] When the system was heated above 140 ℃ under pressure, the solubility of the hydrophobic block increased with the increased temperature leading to the formation of aggregates at a particular temperature. In the case of decreasing temperature, the aggregation was frozen and the morphology was fixed. For example, PS_{386}-*b*-PAA_{79} was heated to 160 ℃ in butanol resulting in the spherical micelles, then cooled to 115 ℃ to form a mixture of microspheres and vesicles.[11]

In addition, the influence of the precipitant (like water) is also related to the N_{agg}.[45] When the water is added to reach a critical water content, BCPs usually become spherical micelles. At the point, the N_{agg} is lower, because the polymer is in the weak aggregation state. As the amount of water increases, the N_{agg} of the micelles will increase causing an improvement in the inner core size. The total amount of micelles in this system and the interfacial energy of the system between the micelle core and water all reduce during the process, while the stretch extent of the PS chain will increase.[45] When the amount of water increases to a certain value, the extension of PS reaches the upper limit and plays a leading role in the systematic free energy. To reduce the extension of PS in order to decrease the free energy, these aggregates will undergo the morphological transformation. For the BCPs containing the hydrophobic chain with high glass transition temperature, the influence of water content on the morphology of aggregates is only applicable to the range of water content where the hydrophobic chain segment can move. For example, for PS-

b-PAA, the limit of water percent is less than 12 wt%. The PS block can still move under low water content, which is necessary for the morphology transformation of the aggregates. In the case of the high content of water, the PS block will be frozen and the morphology will be fixed. This is also the reason why the dripping speed needs to be slower when the H_2O ratio is low. If the dripping is too fast, the morphology of the aggregates (such as spherical micelles) does not have time to change, and the amount of water reaches the range to freeze the PS blocks. So the morphology of aggregation can't transform, and the architectures before PS block freezing is finally obtained.

Moreover, the properties of cosolvents separately affect the size of hydrophobic and hydrophilic chain in the aggregates of BCPs, which leads to the influence on the morphology. For instance, in the self-assembly system of PS_{200}-*b*-PAA_{18}, increasing the ratio of THF/DMF in a mixed solvent would cause a series of morphological changes, while the spherical micelles were achieved in the pure DMF.[46] Then the coexistence of cylindrical micelles with other architectures was observed in the cosolvent with a small amount of THF (5-10%). During the process of adding water, the solvent molecules exist in the hydrophobic part of aggregation such as the core of sphere micelles. The size of the hydrophobic polymer chain of the aggregation relies on the solubility parameters between the polymer and solvent.[45] However, the intensity of repulsion forces of the hydrophilic chain is determined by the size and the charge density of the chain. For example, in DMF with high permittivity (ε= 38.2), the PAA chain segment is highly ionized, and the repulsion interaction is strong; in the THF (ε= 7.5) or dioxane (ε= 7.5) with low permittivity, the ionization can be ignored, so the repulsion interaction is weak. Therefore, similar effect to shortening chain length of PAA, the PS-*b*-PAA BCPs form spherical micelles in the solvent containing DMF, while columnar or vesicle micelles can be achieved in THF or dioxane. In general, the permittivity of

cosolvent can be adjusted by changing the solvents mixed, so the morphology of aggregation based on BCPs can be effectively controlled by using different mixed solvents with different composition.

1.3 Supramolecular self-assembly based on small molecule

1.3.1 Overview of supramolecular self-assembly

Supramolecular chemistry is the study of molecular recognition and molecular aggregates formed by non-covalent interactions. In 1978, for the first time, Lehn presented the concept of "supramolecular chemistry" which was defined as "chemistry beyond the molecule".[47] In 1987, the Nobel Prize of Chemistry was awarded to Lehn and others for their outstanding contributions to the field of supramolecular chemistry, which also made supramolecular chemistry a recognized chemistry discipline. Lehn proposed supramolecular chemistry is defined as follows: supramolecular chemistry is a science that studies the supramolecular system with the specific structure and function formed through two or more chemical species by intermolecular non-covalent interaction. Supramolecular chemistry is a chemical system in which molecular assemblies with specific structures are formed through non-covalent bond interactions between molecules, which is different from molecular chemistry based on covalent bonds. With the rapid development of research in this field, supramolecular chemistry has been enriched and expanded, and its research scope has also expanded from the initial macrocyclic chemistry to molecular recognition, molecular self-assembly, and supramolecular catalysis, devices, and materials. Therefore, supramolecular chemistry has become an irreplaceable part of the modern chemistry discipline.

As a significant part of the supramolecular chemistry area, molecular self-assembly shows its unique advantages and rapid development. The concept of molecular self-assembly was first

proposed by George Whitesides in the 1990s.[48] Molecular self-assembly is a supramolecular system in which building blocks (molecules or molecular clusters) spontaneously aggregate into an ordered architecture through intermolecular non-covalent bonds. Self-assembly is common in nature and technology. For example, the double helix in DNA is formed by intermolecular hydrogen bonds, biological membranes are formed through the assembly of phospholipid molecules, and protein microtubules and microfilaments, as the functional unit of intracellular interaction, are assembled by amyloid fibers. Inspired by biology, various biological and biomimetic materials are obtained through this kind of "bottom-up" method. [49-55]

1.3.2 The driving force of supramolecular assembly

The weak interaction based on intermolecular non-covalent bonds is the key to achieving supramolecular self-assembly, which can be divided into hydrogen bonding, π-π stacking, hydrophobicity, donor-acceptor, and metal-metal interaction. Among these interactions, the hydrogen bond is an attractive non-covalent interaction, which widely exists in nature and artificial systems. It consists of an electronegative heteroatom, including nitrogen, oxygen, or fluorine, bonded to a hydrogen atom and a single pair of electrons on an adjacent molecule and functional group. If the hydrogen bond is formed by two atoms belonging to different types of molecules, the bond is referred to as the intermolecular hydrogen bond. For such bonds, one molecule has a partially positively charged hydrogen as the acceptor atom, while the other molecule has a partially negatively charged hydrogen as the donor atom. When a hydrogen bond is formed by two atoms in the same molecule, it is called the intramolecular hydrogen bond. This happens when two functional groups exist in the same molecule and they attract each other forming a hydrogen bond. For example, in salicylic acid, the intramolecular hydrogen bond will form between the adjacent phenolic hydroxyl group and the carboxylic acid group. In general, the bonding strength of

hydrogen bonds (5-10 kcal mol^{-1}per bond) is much lower than the bonding strength of covalent bonds. In addition, a hydrogen bond is also significant in biology. For instance, the intracellular replication of DNA is on account of a special arrangement of hydrogen bonds between complementary bases on the DNA strand. In artificial supramolecular systems, hydrogen bonds also play an extremely important role. Meijer[56] designed and synthesized 2-ureido-4[1*H*]-pyrimidinone (UPy), which can self-assemble into the long-range orderly assemblies through quadruple H-bonds. (Figure 1.3.1)

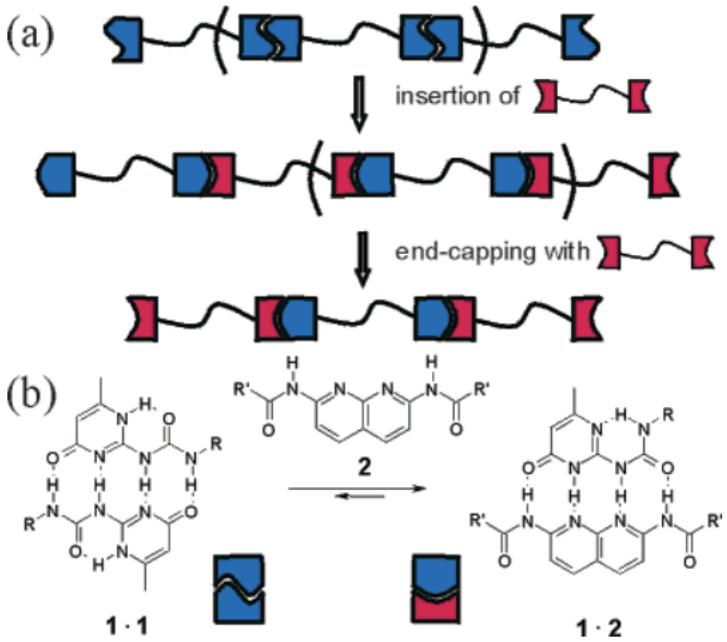

Figure 1.3.1 Self-assembly of monomer with a UPy unit via complementary quadruple H-bonds.[56]

π-π stacking interactions, as the non-covalent interactions among aromatic groups, also open an efficient approach for many supramolecular systems. It refers to the interaction between aromatic rings including π orbitals, whose centroid-centroid spacing is generally about 3.5 Å. According to the geometry of aromatic molecules, the π-π interaction can be formed in the intermolecular face-to-face stacking, and the side-to-face stacking. This kind of weak interaction widely exists in various artificial supramolecular systems. Colquhoun[57] reported an oligomer of

naphthalene diimide, which can form a triple or quadruple π-π stacking effect with the pyrene ring to enhance the healability and toughness of the system, thereby forming a tweezer-type supramolecular material. Nevertheless, the strength of the π-π interaction without directionality is weaker than the hydrogen bond, so it is usually used to construct supramolecular polymer materials by combination with other non-covalent interactions, such as hydrogen bonds.

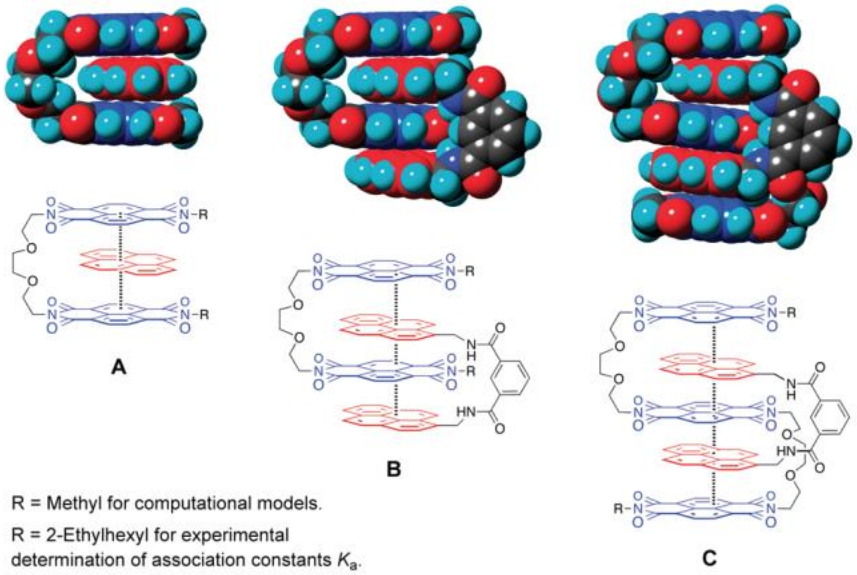

Figure 1.3.2 Schematic illustration of the minimized energy models based on π-π stacking.[57]

Hydrophobic interaction describes the relationship between water and hydrophobic molecules (low water-solubility molecules), which is considered as the repulsive force between water and other molecules. The mixture of lipids and water is a good example of this special interaction. This kind of hydrophobic interaction is very weak, while it is very important in nature, such as forming lipid bilayers, protein folding, and protein-protein recognition.[58] In addition, the host-guest interaction is also the common driving force in supramolecular self-assembly. It occurs between the supramolecular host and guest molecules. Generally, the guest molecules are contained in the cavity of the host molecule with hydrophilic or hydrophobic properties through intermolecular non-covalent interactions, resulting in a kind of complex. In the host-guest system,

a variety of non-covalent forces are always involved, such as hydrogen bonds, hydrophobic interactions and so on. Host molecules such as cyclodextrin recognize the guest molecules through the synergistic effect based on non-covalent interactions and then form large supramolecular aggregates.

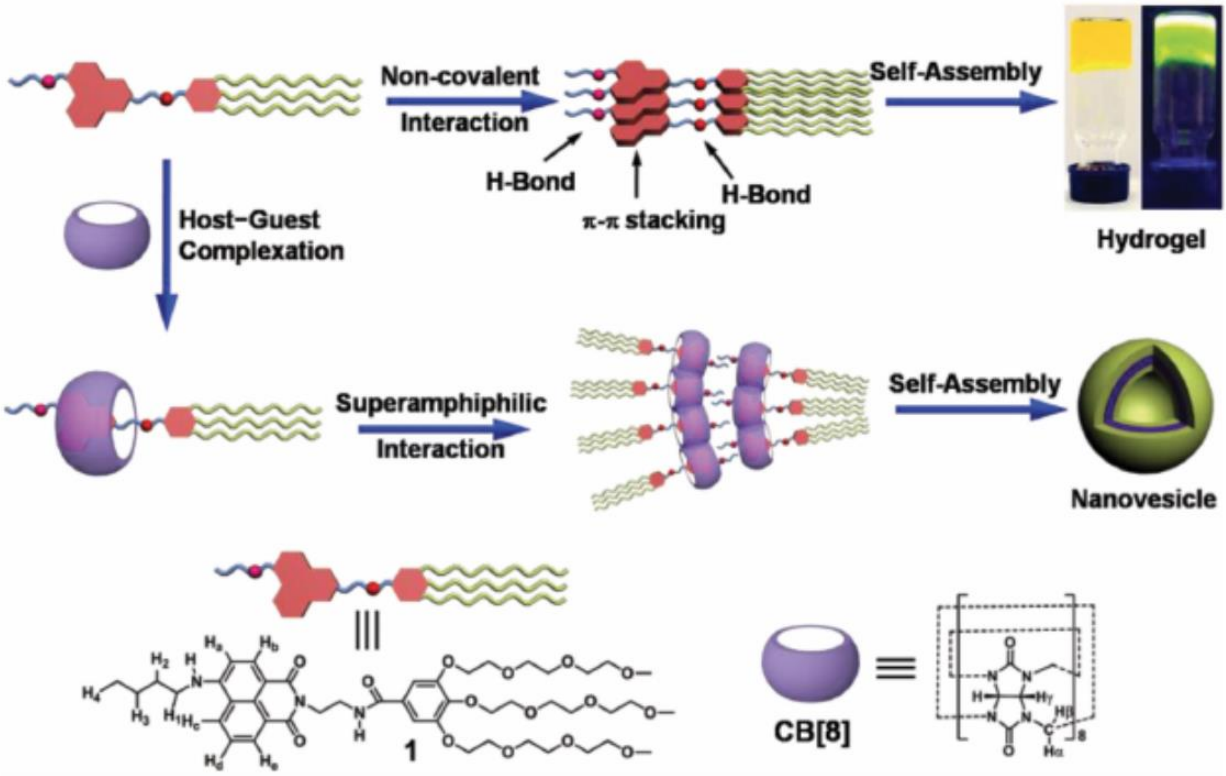

Figure 1.3.3 Schematic diagram of forming nanovesicle and hydrogel based on multiple noncovalent interactions.[59]

Zhao[59] employs cucurbiturils and naphthalimide as raw materials to prepare a supramolecular recognition system: through the host-guest interaction, these two molecules can complex into an amphiphilic complex, and then assemble to form supramolecular vesicles and hydrogels. (Figure 1.3.3) Moreover, a variety of nano drug-carrying systems have been successfully prepared by using these two supramolecular polymers, which has potential applications in the medical field. Metal coordination refers to the combination of some metal ions,

such as transition metal ions, and organic ligands, whose important feature is highly directional. In addition, due to the diversity of organic ligands, the applications of different metal ions can effectively control the value of the interaction and the spectral characteristics. Therefore, metal coordination has broad application prospects in the construction of supramolecular polymers.

1.4 Chiral supramolecule based on self-assembly

1.4.1 Introduction of chirality

Chirality is a basic characteristic of life and nature. In the process of the evolution of creatures on the earth, it is more inclined to the existence of chirality in nature. For example, sugars and amino acids are regarded as typical examples found in biological systems, which have D- and L-enantiomers. On the other hand, from subatomic, molecular to supramolecular, nano, and micro levels, chirality is universal in all these scales. At the molecular level, chiral molecules are universal in nature, including amino acids, sugars, terpenoids, nucleic acids, and so on, while many artificial compounds are also designed with chirality. In addition, many biologic supramolecular systems, and microorganisms are also chiral structures like spiral shapes, such as helicobacter pylori. On larger scales, we can find the vines of many plants and the shells of snails with a single spiral direction.

Among these different chiral levels, supramolecular or molecular chirality is very important. This is because molecular and supramolecular chirality contributes to solving problems in atomic, molecular, and supramolecular scales, which is closely related to physics, chemistry, biology, and materials. [60,61] Chirality based on small molecule plays a leading role in the design of functional molecules or drugs. Due to the rapid development of molecular self-assembly and supramolecular chemistry, chirality at the supramolecular level has also attracted extensive attention from researchers. Molecular chirality can be divided into center, plane, axial, and helical chirality. To

confirm whether a molecule possesses chirality, we should firstly check whether there is an asymmetric atom. Asymmetric carbon atoms or chiral carbon are sp^3 atoms that are linked with four different groups of atoms or different types of atoms. Moreover, one molecule, with two misaligned axes or two non-coplanar rings which are asymmetrically connected by chemical bonds, cannot overlap with its mirror image and these chemical bonds cannot be easily rotated or the substituent groups are arranged asymmetrically on the axis. Even if the molecule lacks asymmetric carbon atoms, the molecule is considered to be chiral. This situation of chirality is regarded as axial chirality and planar chirality, respectively.

Because of the noncovalent bond as the base of supramolecular chemistry, supramolecular chirality is obtained through the asymmetric arrangement of noncovalent structures, which can be achieved by chiral molecules, only achiral molecules, or the combination of chiral and achiral molecules. The assembled approaches of the molecules largely decide supramolecular chirality and the molecular chirality is important in the assembled approaches of the supramolecular system. Generally, chiral molecules are inclined to become supramolecular architectures with specific chirality. In the case of the combination of different molecules, when there is a robust interaction between these molecules, the achiral molecules will be induced into chiral architectures. Mostly, the supramolecular chirality based on the assembled system has been confirmed, which should be consistent with the chirality of chiral molecules. In addition, supramolecular chirality based on achiral molecules can be obtained by forming the supramolecular assembly system, but it is usually racemic in the achieved macroscopic system. The chirality of the supramolecular assembly can be characterized by the circular dichroic spectrum (CD), while the morphology of the assemblies can be characterized by AFM, SEM, and TEM. If the chiral center is away from the location of a chromophore, the CD signal in its monomer state or free state is silent in the chromophore area.

However, after self-assembly, the entire assemblies express the chirality that can be detected by CD. In the assembled process of chiral architectures, the chromophores incline to the spatially asymmetric or the chiral arrangement through various non-covalent bonds, to minimize the energy of the system. In most cases, this type of assembly exhibits the chiral structure, which can be observed by AFM or SEM. For a chiral system with CD signals, chiral transfer depends on the structural characteristics of the chiral molecule instead of components of chiral nanostructures.

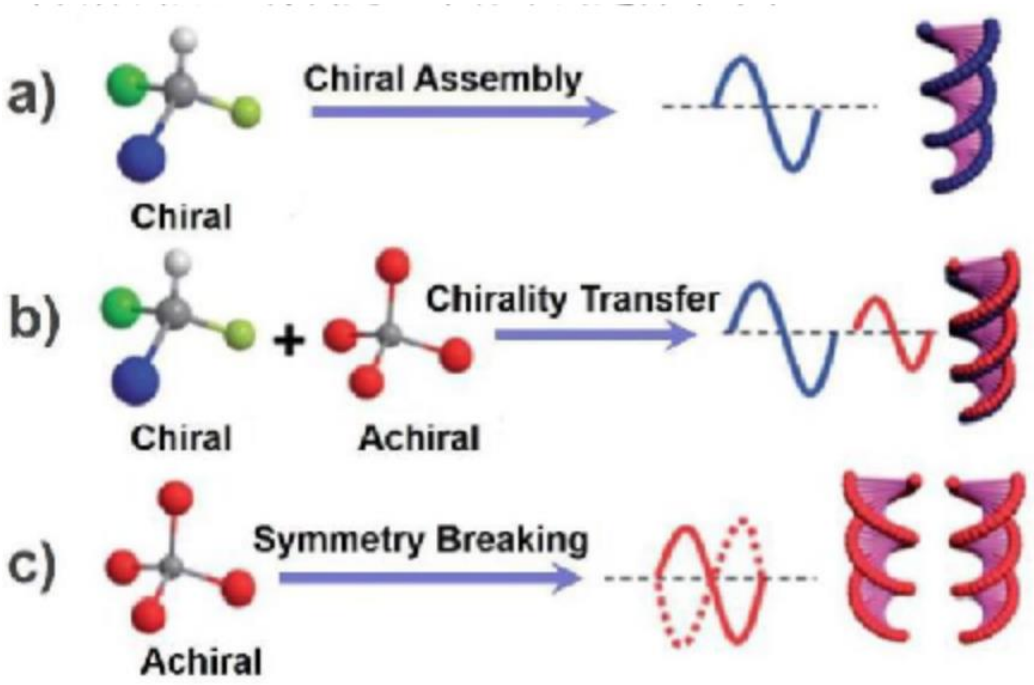

Figure 1.4.2 Method for obtaining supramolecular chirality in supramolecular assembly system. a) Self-assembly based on chiral molecules; b) Chiral molecules co-assembly with achiral molecules; c) Self-assembly based on completely achiral molecules

1.4.2 Approaches to obtain supramolecular chirality

There are usually three approaches to obtaining supramolecular chirality through the molecular assembly. First, through the interaction of non-covalent bonds, chiral molecules assemble into supramolecular architectures with the specific component or ordered structures

revealing chiral characteristics. Then the other approach to obtaining supramolecular chirality is through the co-assembly with achiral molecules and chiral molecules. Through the co-assembly method, achiral molecules are induced to obtain chirality under the chiral environment, expressing supramolecular chirality. The third type to obtain supramolecular chirality is using achiral molecules by self-assembly. In this way, the obtained supramolecule express chirality through the structural characteristics. As shown in Figure 1.4.2, during the process of obtaining supramolecular chirality, three important principles should be followed. The first rule is spontaneous symmetry breaking, which means that molecules are arranged asymmetrically in the process of assembly leading to the destruction of the symmetry of the assembled structure, resulting in exhibiting chirality. The second concept is the "general-soldier principle". It means that the introduction of a few chiral elements determines the supramolecular chirality of the entirely achiral assembly system. Next, the "majority principle" is that, in the assembly process based on the enantiomeric mixture, the addition of a small amount of a single enantiomer will determine the supramolecular chirality.

1.4.2.1 Supramolecular assembly by chiral molecules

It is the common method to obtain supramolecular chirality is self-assembly based on chiral molecules. In the process of chiral assembly, the chirality generally transfers from the chiral center to resulting assemblies. This kind of transfer relies on many factors, including the strength of non-covalent bonds, the distance between the chiral center to the assembly location, and the balance between chiral and achiral interactions. So far, a lot of works based on fiber aggregates based on amphiphilic chiral molecules have been reported.[62] These amphiphilic molecules include diacetylene phospholipids, diglycolipids with open or cyclic sugars or side chains containing

various numbers and types of unsaturated bonds, amino acid-based amphiphiles, amphiphiles with hexamethylene diamine, and so on.[63-68] Ihara's group and Liu's group respectively reported a range of amphiphilic molecules based on enantiomeric glutamine. [69-73] Liu has also conducted in-depth research on the chiral transfer from molecules to supramolecules in assembled nanostructures. Chiral assembled nanostructures are usually achieved through the gelation process. Amphiphilic molecules are dissolved in a specific solvent through heating or ultrasonic treatment, and then the solution in the transparent state is cooled to the specified temperature or room temperature, resulting in assembled gel with chirality and various chiral nanostructures. Normally, to obtain enantiomeric assembled structures, molecules with different chirality need to be assembled separately. Interestingly, the self-assembly of homochiral molecules can also achieve supramolecular structures with different chirality. For example, Ajayaghosh reported a chiral oligophenylene ethylene derivative, which can assemble into the spiral structure with opposite chirality.[73] At lower concentrations, the pure enantiomer can be assembled into a 1D helical structure in a solvent, and the chirality of the helical structure is consistent with the chirality of the molecule. As the concentration increases, the 1D helical structure aggregates become the super helices, which exhibit the opposite chirality compared with the molecular chirality. The chiral reversion is closely related to the different enthalpy changes in the system when assembly at different concentrations.[73]

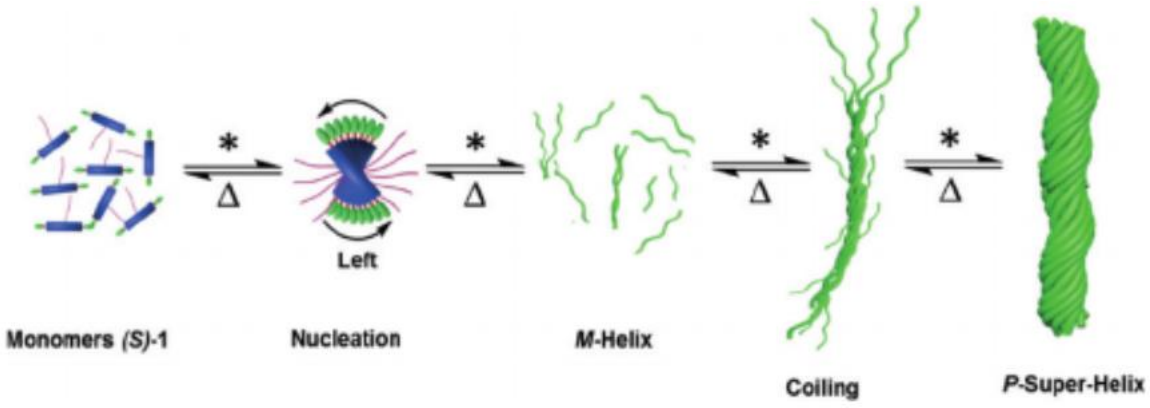

Figure 1.4.3 Nucleation-elongation of one type of chiral molecule to form 1D helical to super-helical structures, which showed opposite chirality. [73]

1.4.2.2 Chiral supramolecular co-assembly with achiral molecules and chiral molecules

Through the non-covalent bond between different molecules with or without chirality, the chirality of achiral molecules can be induced, so that the supramolecular system expresses chirality at the supramolecular level. In the assembly process of molecules without chirality, when the chiral reagents, chiral molecules, or chiral interactions are introduced, these factors may have a huge impact on the assembly process. This approach to obtaining supramolecular chirality complies with the "general-soldier principle" mentioned above. In general, achiral molecules can be induced to exhibit chiral optical activity through chiral templates, host-guest interactions, and helices. For example, Armitage reported the DNA as a chiral template to induce the chirality of cyanine dyes. [74] Various cyanine dyes can be co-assembled with DNA through electrostatic interaction. In the process of co-assembly, different dye molecules have different dimerization ways including head-to-tail and head-to-head aggregation. In addition, the assemblies of the cyanine dye match the size of the groove on the surface of the DNA, so that the interaction between the DNA and the dye

induces the chirality of the achiral cyanine dye. The intensity of the chiral signal depends on the aggregation tendency of the cyanine dye molecules in water.

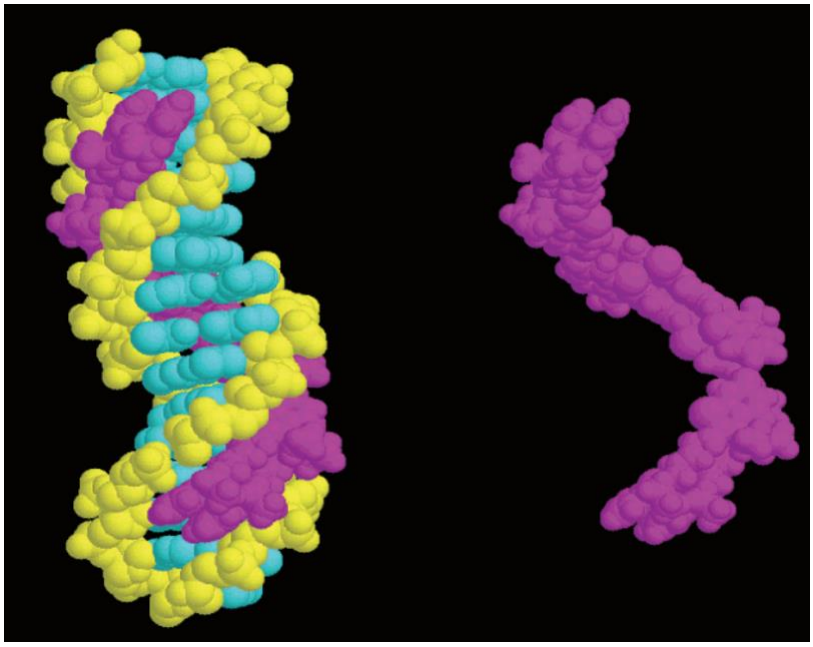

Figure 1.4.4 Molecular model reveals three dimers belonging to end-to-end within the minor groove of a DNA template. [74]

In addition, Yan's group reported supramolecular assembly systems based on β-cyclodextrin (β-CD) and alkyl amines ($CH_3(CH_2)_{n-1}NH_2$). [86] By the kinetics regulation of the assembly process, assemblies with opposite chiral signals were achieved. Because of the existence of amine, the chiral helices could be manipulated by controlling the ratio of amine and cyclodextrin. Meanwhile, changing the length of the alkyl chain could control the supramolecular architectures to affect supramolecular chirality. Furthermore, enzyme responsive supramolecular chirality is obtained as a result of shifting the molar ratio by enzyme triggered hydrolysis of β-CD. This work based on host-guest chemistry supplies a new strategy to open up an area of rationally designed chiral supramolecular materials.

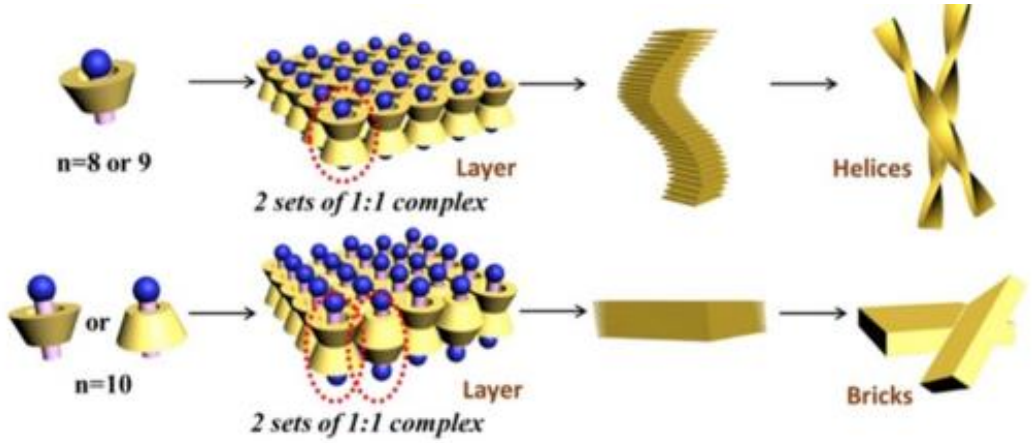

Figure 1.4.5 Alkylamines of different lengths are assembled into helical and massive structures with cyclodextrin through host-guest interaction.[86]

1.4.2.3 Chiral supramolecular assembly with achiral molecules

Achiral molecules also can achieve assemblies with supramolecular chirality through self-assembly without the involvement of any chiral factors. In the chiral assembly process based on achiral molecules, the symmetry is randomly broken and the assemblies composed of a certain enantiomer in the system take over or are excessive, resulting in supramolecular chirality. Generally, the necessary condition of symmetry breaking is the existence of an asymmetric environment. [75-76] Interestingly, under the achiral condition, some molecules can also break their symmetry during the assembly process to obtain supramolecular chirality.[77-79] In recent years, a series of achiral molecules have been utilized to fabricate chiral structures through spontaneous symmetry breaking to express chiral structures, such as amphiphilic assemblies,[80,81] liquid crystal,[82-84] dye aggregate,[79] supramolecular gel, [80] and other systems. For example, in 2008, You's research group first reported the symmetry breaking of an achiral assembly in the gel state.[80] They synthesized a series of imidazole derivatives that can complex with silver ions to form a polymeric gel. After gelation, the system showed a strong CD peak, which revealed that a symmetry break appeared in the formation process of the gel. However, they also found that gels

prepared in different batches showed opposite chiral signals, which showed that the chirality of the system is uncontrollable. Notably, the imidazole ligand with the rigid bending conformation and the silver ion adopted the linear complexing way to break the symmetry, resulting in the helical structure.

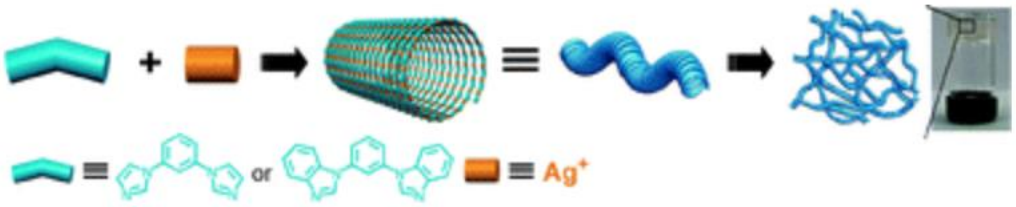

Figure 1.4.6 The self-assembly supramolecular chirality of bent bridging ligands coordinated with silver ion. [80]

Based on the currently obtained assembly systems with supramolecular chirality through symmetry breaking, generally, chiral nanostructures can be achieved by excessive enantiomers instead of pure enantiomers. In addition, in most cases, the choice of chirality is also random. Therefore, many approaches have been developed, such as using rotary evaporation, vortex by magnetic stirring, and using circularly polarized light to select and amplify the supramolecular chirality based on achiral assemblies. Liu reported that a gel system based on achiral molecules C_3 achieved controllable chirality through symmetry breaking.[85] In the mixed solvent, the C_3 molecules could assemble into a racemic gel. After the introduction of the vortex, in the process of forming gel, the molecules were arranged in an asymmetric way resulting in a gel with supramolecular chirality, but the chirality was not controllable. Therefore, the obtained chiral gel was used as a chiral seed, and, after mixing with the racemic gel and ageing, supramolecular assemblies with controllable chirality could be achieved.

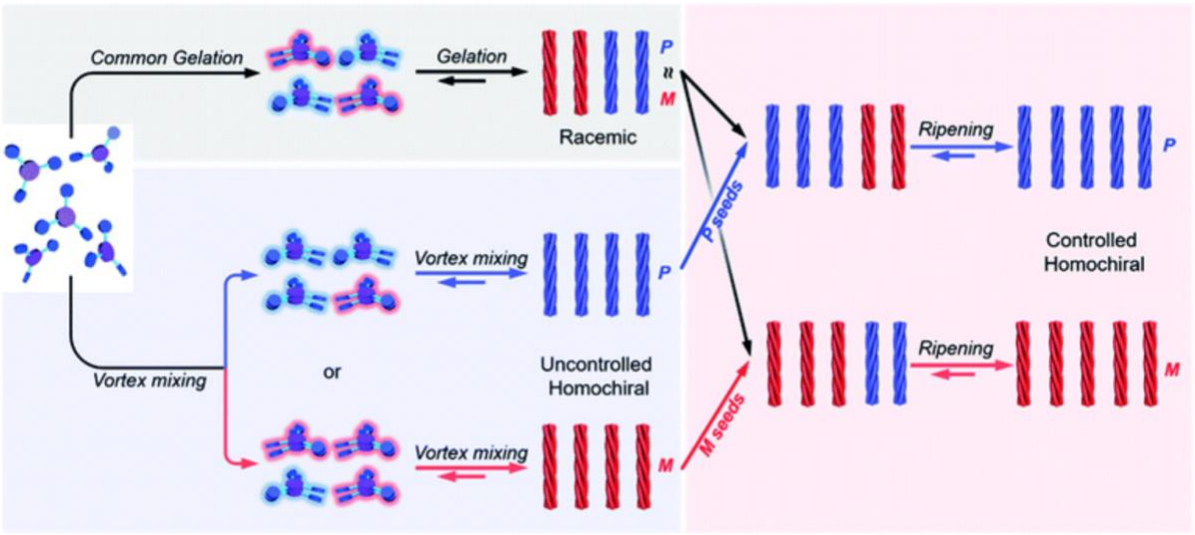

Figure 1.4.7 Achiral C_3-symmetric monomer self-assembly into nanostructure with controlled homochiral by vortex mixing and ageing. [85]

1.5 Aims and outline of the thesis

To sum up, with the rapid development of supramolecular chemistry, as an important part of supramolecular chemistry, chiral supramolecule and 2D supramolecular structure as non-spherical have attracted the attention of many researchers. The thesis mainly aims to understand the design and synthesis of PPV-based BCPs and amino acid derivatives which can be employed to construct 1D chiral and 2D non-spherical nanomaterials by the supramolecular assembly, and explore their resultant properties. Meanwhile, it's significant to develop new supramolecular architectures and approaches to achieve precise control as well as expand the application for biology and optoelectronics.

As discussed above, there are many factors affecting self-assembly properties including the block ratio of BCPs, the intermolecular interactions, the hydrophobicity, and the crystalline. To study the influence of increased intermolecular interactions on building 2D nanomaterials based on BCPs, Chapter 2 described the synthesis route of the introduction of chlorine at side chain of

PPV core as the building block. Through the heating-cooling self-assembly, new morphology as the rod-like micelle was obtained, compared with PPV with the alkyl chain[33]. By establishing the thermally induced nucleation self-assembly methods, morphological transformation to diamond micelles was achieved and we also tested the effect of the concentration, the annealing temperature, and the unimer on assemblies. Then we introduced the crystalline into the PPV-based BCPs by engineering the TIPs group at the side chain. The balance between the crystalline force and π−π stacking interaction caused the morphological transition from square to rectangular micelles with controllable aspect ratios and we also compared the effect of the block ratios or the concentration on final morphology. Based on the above balance, the heterogenous co-assembly by two different PPV-based BCPs was also achieved as new circular disk-like micelles.

Having successfully achieved different assemblies through the design of BCPs, we also build the new assembly model based on amino acid derivatives for supramolecular self-assembly by H-bonds. In Chapter 4, because of the properties of amino acid arms on TDAP, helices with controllable chirality were obtained through heating-cooling assembly in solutions, which was similar to the assembly behavior of peptides. Then we explored the biology application by using co-assembly based on intermolecular interactions. In this way, we could achieve molecular detection of melamine and test the limit of the detection. Next, we replaced the amino acid arms by using valine with a lower steric hindrance to assembly. In Chapter 5, the new H-bonding pattern of TDAV was obtained and a series of 2D platelets with controllable shapes were achieved and we also explored the effect of the water ratios on these 2D micelles.

1.6 References

[1] Whitesides, G. M.; Grzybowski, B., Self-assembly at all scales. Science 2002, 295, 2418.

[2] Service, R. F., How far can we push chemical self-assembly? Science 2005, 309, 95.

[3] Qi R.; Zhu Y.; Han L.; Wang M.; He F., Rectangular Platelet Micelles with Controlled Aspect Ratio by Hierarchical Self-Assembly of Poly(3-hexylthiophene)-b-poly (ethylene glycol). Macromolecules 2020, 53 (15), 6555-6565.

[4] Alexandridis P.; Lindman B., Amphiphilic Block Copolymers: Self-assembly and Applications. Amsterdam: Elsevier, 2000.

[5] Bates F. S.; Fredrickson G. H., Block copolymers-designer soft materials. Phys. Today 1999, 52: 32-38.

[6] Kim J. K.; Yang S. Y.; Lee Y.; Kim Y., Functional nanomaterials based on block copolymer self-assembly. Prog. Polym. Sci. 2010, 35(11): 1325-1349.

[7] Orilall M. C.; Wiener U., Block copolymer based composition and morphology control in nanostructured hybrid materials for energy conversion and storage: Solar cells, batteries, and fuel cells. Chem. Soc. Rev. 2011, 40(2): 520-535.

[8] Zhang L.; Eisenberg A., Multiple morphologies and characteristics of crew-cut micelle-like aggregates of polystyrene-b-poly (acrylic acid) diblock copolymers in solution. Science 1995, 268(5218): 1728-1731.

[9] Chen D.; Jiang M., Strategies for constructing polymeric micelles and hollow spheres in solution via specific intermolecular interactions. Acc. Chem. Res. 2005, 38 (6): 494-502.

[10] Cui H.; Chen Z.; Zhong S.; Wooley K.L.; Pochan D. J., Block copolymer assembly via kinetic control. Science 2007, 317 (5838): 647-650.

[11] Zhang L.; Eisenberg A., Multiple morphologies and characteristics of "crew-cut" micelle-like aggregates of polystyrene-b-poly (acrylic acid) diblock copolymers in aqueous, solutions. J. Am. Chem. Soc. 1996, 118 (13): 3168-3181

[12] Wang X.; Guerin G.; Wang H.; Wang Y.S.; Manners I.; Winnik A. M., Cylindrical block copolymer micelles and co-micelles of controlled length and architecture. Science 2007, 317 (5838): 644-647.

[13] Harada A.; Kataoka K., Chain length recognition: Core-shell supramolecular assembly from oppositely charged block copolymers. Science 1999, 283 (5398): 65-67.

[14] Förster S.; Antonietti M., Amphiphilic block copolymers in structure-controlled nanomaterial hybrids. Adv. Mater. 1998, 10 (3): 195-217.

[15] Gädt T.; leong N. S.; Cambridge G.; Winnik M. A.; Manners I., Complex and hierarchical micelle architectures from diblock copolymers using living, crystallization-driven polymerizations. Nat. Mater. 2009, 8 (2): 144-150.

[16] Gillies E. R.; Jonson T. B.; Fréchet J. M. J., Stimuli-responsive supramolecular assemblies of linear-dendritic copolymers. J. Am. Chem. Soc. 2004, 126 (38): 11936-11943.

[17] Goodwin A. P.; Mynar J. L.; Ma Y.; Fleming R. G.; Fréchet M. J. J., Synthetic micelle sensitive to IR light via a two-photon process. J. Am. Chem. Soc. 2005, 127 (28): 9952-9953.

[18] Hu J.; Liu G.; Nijkang G., Hierarchical interfacial assembly of ABC triblock copolymer. J. Am. Chem. Soc. 2008, 130 (11): 3236-3237.

[19] Qiu H.; Gao Y.; Boott C. E.; Gould O. E.; Harniman R. L.; Miles M. J.; Webb S. E. D.; Winnik M. A.; Manners I., Uniform patchy and hollow rectangular platelet micelles from crystallizable polymer blends. Science 2016, 352 (6286): 697-701.

[20] Kataoka K.; Harada A.; Nagasaki Y., Block copolymer micelles for drug delivery: Design, characterization and biological significance. Adv. Drug. Deliv. Rev. 2001, 47 (1): 113-131.

[21] Mai Y.; Eisenberg A., Chem. Soc. Rev. 2012, 41, 5969-5985.

[22] Shen H.; Zhang L.; Eisenberg A., Thermodynamics of crew-cut micelle formation of polystyrene-*b*-poly (acrylic acid) diblock copolymers in DMF/H_2O mixtures. J. Phys. Chem. B. 1997, 101(24):4697-4708.

[23] F¨orster S.; Antonietti M., Amphiphilic Block Copolymers in Structure-Controlled Nanomaterial Hybrids. Adv. Mater. 1998, 10, 195–217.

[24] Ganda, S.; Dulle, M.; Drechsler, M.; Förster, B.; Förster, S.; Stenzel, M. H., Two-Dimensional Self-Assembled Structures of Highly Ordered Bioactive Crystalline-Based Block Copolymers. Macromolecule*s* 2017, 50 (21), 8544-8553.

[25] Schacher F. H.; Rupar P. A.; Manners I., Functional block copolymers: nanostructured materials with emerging applications. Angew. Chem. Int. Ed. 2012, 51, 7898–7921.

[26] Riess G., Micellization of block copolymers. Prog. Polym. Sci. 2003, 28(7): 1107-1170.

[27] Cameron N. S.; Corbierre M. K.; Eisenberg A., Asymmetric amphiphilic block copolymers in solution: a morphological wonderland. Can. J. Chem. 1999, 77, 1311–1326.

[28] Tritschler U.; Pearce S.; Gwyther J.; Whittell G. R.; Manners I., Functional nanoparticles from the solution self-Assembly of block copolymers. Macromolecules 2017, 50, 3439–3463.

[29] Hayward R. C.; Pochan D. J., Tailored assemblies of block copolymers in solution: It is all about the process. Macromolecules 2010, 43, 3577–3584.

[30] Macfarlane L.; Zhao C.; Cai J.; Qiu H.; Manners I., Emerging applications for living crystallization- driven self-assembly, Chem. Sci. 2021,12, 4661-4682.

[31] Lin Y. Y.; Thomas M. R.; Gelmi A.; Leonardo V.; Pashuck E. T.; Maynard S. A.; Wang Y.; Stevens M. M., Self-Assembled 2D Free- Standing Janus Nanosheets with Single-Layer Thickness. J. Am. Chem. Soc. 2017, 139, 13592−13595.

[32] Zhuo M. P.; Tao Y. C.; Wang X. D.; Wu Y. C.; Chen S.; Liao L. S.; Jiang L., 2D Organic Photonics: An Asymmetric Optical Waveguide in Self-Assembled Halogen-Bonded Cocrystals. Angew. Chem., Int. Ed. 2018, 57, 11300−11304.

[33] Han L.; Wang M. J.; Jia X. M.; Chen W.; Qian H. J.; He F., Uniform two-dimensional square assemblies from conjugated block copolymers driven by pi-pi interactions with controllable sizes. Nat. Commun. 2018, 9, No. 865.

[34] Ganda S.; Dulle M.; Drechsler M.; Forster B.; Forster S.; Stenzel M. H., Two-Dimensional Self-Assembled Structures of Highly Ordered Bioactive Crystalline-Based Block Copolymers. Macromolecules 2017, 50, 8544−8553.

[35] Hudson Z. M.; Boott C. E.; Robinson M. E.; Rupar P. A.; Winnik M. A.; Manners I., Tailored hierarchical micelle architectures using living crystallization-driven self-assembly in two dimensions. Nat. Chem. 2014, 6, 893−898.

[36] Nazemi A.; He X. M.; MacFarlane L. R.; Harniman R. L.; Hsiao M. S.; Winnik M. A.; Faul C. F. J.; Manners I., Uniform "Patchy" Platelets by Seeded Heteroepitaxial Growth of Crystallizable Polymer Blends in Two Dimensions. J. Am. Chem. Soc. 2017, 139, 4409−4417.

[37] Wang M. J.; Han L.; Zhu Y. L.; Qi R.; Tian L. L.; He F., Formation of Hierarchical Architectures with Dimensional and Morphological Control in the Self-Assembly of Conjugated Block Copolymers. Small Methods 2020, 4, 1900470.

[38] Zhu C.; Liu L.; Yang Q.; Lv F.; Wang S., Water-soluble conjugated polymers for imaging, diagnosis, and therapy. Chem. Rev. 112, 4687–4735 (2012).

[39] Tao D.; Feng C.; Cui Y.; Yang X.; Manners I.; Winnik, M. A.; Huang, X., Monodisperse Fiber-like micelles of controlled length and composition with an oligo (p-phenylenevinylene) core via "living" crystallization-driven self-assembly. J. Am. Chem. Soc. 2017, 139, 7136−7139.

[40] Sun H.; Liu J.; Li S.; Zhou L.; Wang J.; Liu L.; Lv F.; Gu Q.; Hu B.; Ma Y.; Wang S., Reactive Amphiphilic Conjugated Polymers for Inhibiting Amyloid b Assembly. Angew. Chem., Int. Ed. 2019, 58, 5988−5993.

[41] Wang M.; Han L.; Zhu Y.; Qi R.; Tian L.; He F., Inky flower-like supermicelles assembled from π-conjugated block copolymers. Polym. Chem. 2020, 11, 61-67.

[42] Han L.; Fan H.; Zhu Y. L.; Wang M.J.; Pan F.; Yu, D. P.; Zhao, Y.; He, F., Precisely Controlled Two-Dimensional Rhombic Copolymer Micelles for Sensitive Flexible Tunneling Devices. CCS Chemistry 2020, 3 (5), 1399-1409.

[43] Schmelz J.; Schedl A. E.; Steinlein C.; Manners I.; Schmalz H., Length control and block-type architectures in worm-like micelles with polyethylene cores. J. Am. Chem. Soc. 2012. 134(34): 14217-14225.

[44] Desbaumes L.; Eisenberg A., Single-solvent preparation of crew-cut aggregates of various morphologies from an amphiphilic diblock copolymer. Langmuir 1999, 15(1): 36-38.

[45] Shen H.; Eisenberg A., Morphological phase diagram for a ternary system of block copolymer PS_{310}-*b*-PAA_{52}/dioxane/H_2O. J. Phys. Chem. B 1999. 103(44): 9473-9487.

[46] Yu Y.; Zhang L.; Eisenberg A., Morphogenic effect of solvent on crew-cut aggregates of amphiphilic diblock copolymers. Macromolecules 1998, 31(4): 1144-1154

[47] Lehn J. M., Supramolecular chemistry. Science 1993, 260(5115): 1762-1764.

[48] Whitesides G. M.; Grzybowski, B., Self-assembly at all scales. Science 2002, 295(5564): 2418-2421.

[49] Aizenberg J.; Fratzl P., Biological and biomimetic materials. Adv. Mater. 2009, 21(4): 387-388.

[50] Sanchez C.; Arribart H.; Guille M. M. G., Biomimetism and bioinspiration as tools for the design of innovative materials and systems. Nat. Mater. 2005, 4(4): 277-288.

[51] Palmer L. C.; Newcomb C. J.; Kaltz S. R.; Spoerke E. D.; Stupp S. I., Biomimetic systems for hydroxyapatite mineralization inspired by bone and enamel. Chem. Rev. 2008, 108(11): 4754-4783.

[52] Ariga K.; Hill J. P.; Lee M. V.; Vinu A.; Charvet R.; Acharya S., Challenges and breakthroughs in recent research on self-assembly. Sci. Technol. Adv. Mater. 2008, 9(1): 1468-1565.

[53] Nie Z.; Kumacheva E., Patterning surfaces with functional polymers. Nat. Mater. 2008, 7(4): 277-290.

[54] Ajayaghosh A.; Praveen V. K.; Vijayakumar C., Organogels as scaffolds for excitation energy transfer and light harvesting(J]. Chem. Soc. Rev. 2008, 37(1): 109-122.

[55] He Q.; Duan L.; Qi W.; Wang K.; Cui Y.; Yan X.; Li J., Microcapsules containing a biomolecular motor for atp biosynthesis. Adv. Mater. 2008, 20(15): 2933-2937.

[56] Ligthart G.; Ohkawa, H.; Sijbesma, R. P.;Meijer E. W., Complementary quadruple hydrogen bonding in supramolecular copolymers . J. Am. Chem. Soc. 2005, 127(3): 810-811.

[57] Burattini S.; Greenland B. W.; Hayes, W.; Mackay M. E.; Rowan S. J.; Colquhoun H. M., A supramolecular polymer based on tweezer-type π-π interactions: molecular design for healability and enhanced toughness. Chem. Mater. 2011, 23(1): 6-8.

[58] Ko I. K.; Kean T. J.; Dennis J. E. Targeting mesenchymal stem cells to activated endothelial cells. Biomaterials 2009, 30: 3702-3710.

[59] Xu X. D.; Li X.; Chen, H.; Qu Q.; Zhao L.; Agren H.; Zhao Y., Host-guest interaction-mediated construction of hydrogels and nanovesicles for drug delivery. Small 2015, 11(44): 5901-5906.

[60] Minakawa M. ; Nakagawa M.; Wang K. H.; Imura Y.; Kawai T., Controlling Helical Pitch of Chiral Supramolecular Nanofibers Composed of Two Amphiphiles. Bull. Chem. Soc. Jpn. 2020, 93 (10), 1150-1154.

[61] Ghosh D., Farahani A. D., Martin A. D.; Thordarson P.; Damodaran K. K., Chem. Mater. 2020, 32, 3517.

[62] Sorrenti A.; Illa O.; Ortuno R. M., Amphiphiles in aqueous solution: Well beyond a soap bubble[J]. Chem. Soc. Rev. 2013, 42(21): 8200-8219.

[63] Yui H.; Minamikawa H.; Danev R.; Nagayama K.; Kamiya S.; Shimizu T., Growth process and molecular packing of a self-assembled lipid nanotube: Phase-contrast transmission electron microscopy and XRD analyses. Langmuir 2008, 24(3): 709-713.

[64] Kamiya S.; Minamikawa, H.; Jung, J. H.; Yang B.; Masuda M.; Shimizu T., Molecular structure of glucopyranosylamide lipid and nanotube morphology. Langmuir 2005, 21(2): 743-750.

[65] Barclay T. G.; Constantopoulos, K.; Zhang, W., Fujiki M; Petrovsky N.; Matisons J. G., Chiral self-assembly of designed amphiphiles: Influences on aggregate morphology. Langmuir 2013, 29(32): 10001-10010.

[66] Fuhrhop J. H.; Helfrich W., Fluid and solid fibers made of lipid molecular bilayers. Chem. Rev. 1993, 93(4): 1565-1582.

[67] Fujita N.; Shinkai S., Design and function of low molecular-mass organic gelators (Imogs) bearing steroid and sugar groups. Molecular gels: materials with self-assembled fibrillar networks,

2006: 553-575.

[68] Shimizu T.; Masuda M.; Minamikawa H., Supramolecular nanotube architectures based on amphiphilic molecules. Chem. Rev. 2005, 105(4): 1401-1443.

[69] Wang X.; Liu M., Vicinal solvent effect on supramolecular gelation: Alcohol controlled topochemical reaction and the toruloid nanostructure. Chem. A Euro. J. 2014, 20(32): 10110-10116.

[70] Takafuji M. Kira Y.; Tsuji H., Sawada S.; Hachisako H.; Ihara H., Optically active polymer film tuned by a chirally self-assembled molecular organogel. Tetrahedron 2007, 63(31): 7489-7494.

[71] Shirosaki T.; Chowdhury S.; Takafuji M., Alekperov D.; Popova G.; Hachisako H.; Ihara H., Functional organogels from lipophilic 1-glutamide derivative immobilized on cyclotriphosphazene core. J. Mater. Res. 2006, 21(5): 1274-1278.

[72] Kira Y.; Okazaki Y.; Sawada T.; Takafuji M.; Ihara H., Amphiphilic molecular gels from omega-aminoalkylated I-glutamic acid derivatives with unique chiroptical properties. Amino Acids 2010, 39(2): 587-597.

[72] Jintoku H.; Sagawa T.; Sawada T., Takafuji M.; Hachisako H.; Ihara H., Molecular organogel-forming porphyrin derivative with hydrophobic 1-glutamide. Tetrahedron Lett. 2008, 49(25): 3987-3990.

[73] Hifsudheen M.; Mishra R. K.; Vedhanarayanan B., Praveen V. K.; Ajayaghosh A., The helix to super-helix transition in the self-assembly of pi-systems: Superseding of molecular chirality at hierarchical level. Angew. Chem. Int. Ed. 2017, 56(41): 12634-12638.

[74] Garoff R. A.; Litzinger E. A.; Connor R. E., Fishman I., Armitage B. A., Helical Aggregation of Cyanine Dyes on DNA Templates: Effect of Dye Structure on Formation of Homo- and Hetero aggregates. Langmuir 2002, 18(16):6330-6337.

[75] Crusats J.; El-Hachemi Z.; Ribo J. M.; Hydrodynamic effects on chiral induction. Chem. Soc. Rev. 2010, 39(2): 569-577.

[76] Micali N.; Engelkamp H.; van Rhee P. G., Chiristianen P. C. M.; Scolaro L. M.; Mann J. C., Selection of supramolecular chirality by application of rotational and magnetic forces. Nat. Chem. 2012, 4(3): 201-207.

[77] Ribo J. M.; Crusats J.; Sagues F., Claret J.; Rubires R., Chiral sign induction by vortices during the formation of mesophases in stirred solutions. Science 2001, 292(5524): 2063-2066.

[77] Yuan, J.; Liu, M. H., Chiral molecular assemblies from a novel achiral amphiphilic 2-(heptadecy) naphtha 2,3 imidazole through interfacial coordination. J. Am. Chem. Soc. 2003, 125(17): 5051-5056.

[78] Huang, X.; Li, C.; Jiang, S. G., Wang X.; Zhang B.; Liu M. H., Self-assembled spiral nanoarchitecture and supramolecular chirality in langmuir-blodgett films of an achiral amphiphilic barbituric acid. J. Am. Chem. Soc. 2004, 126(5): 1322-1323.

[79] Oiu Y.: Chen P.: Liu M., Evolution of various porphyrin nanostructures via an oil/aqueous medium: Controlled self-assembly, further organization, and supramolecular chirality. J. Am. Chem. Soc. 2010, 132(28): 9644-9652.

[80] Zhang S.; Yang S.; Lan J., Yang S.; You J., Helical nonracemic tubular coordination polymer gelators from simple achiral molecules. Chem. Commun. 2008, 46: 6170-6172.

[81] Song B.; Liu B.; Jin Y.; He X.; Tang D.; Wu G.; Yin S., Controlled self-assembly of helical nano-ribbons formed by achiral amphiphiles. Nanoscale 2015, 7(3): 930-935.

[82] Link D. R.; Natale G.; Shao R.; Maclennan J. E.; Clark N. A.; Korblova E.; Walba D. M., Spontaneous formation of macroscopic chiral domains in a fluid smectic phase of achiral molecules. Science 1997, 278(5345): 1924-1927.

[83] Hough L. E.; Spannuth M.; Nakata M.; Coleman D. A.; Jones C. D.; Danlgraber G.; Tschierske C.; Watanabe J.; Korblova E.; Walba D. M.; Maclennan J. E.; Glaser M. A.; Clark N. A., Chiral isotropic liquids from achiral molecules. Science 2009, 325(5939): 452-456.

[84] Dressel C.; Liu F.; Prehm M., Zeng X.; Ungar G.; Tschierske C., Dynamic mirror-symmetry breaking in bicontinuous cubic phases. Angew. Chem. Int. Ed. 2014, 53(48): 13115-13120.

[85] Sang Y.; Yang D.; Duan P.; Liu M., Towards homochiral supramolecular entities from achiral molecules by vortex mixing-accompanied self-assembly. Chem. Sci. 2019, 10(9): 2718-2724.

[86] Wang X.; Li M.; Song, P., Lv X.; Liu Z.; Huang J.; Yan Y., Reversible manipulation of supramolecular chirality using host-guest dynamics between beta-cyclodextrin and alkyl amines. Chem. Eur. J. 2018, 24(52): 13734-13739.

CHAPTER 2 TRANSFORMATION FROM ROD-LIKE TO DIAMOND-LIKE MICELLES BY THERMALLY INDUCED NUCLEATION SELF-ASSEMBLY

Published Article

Heng Li,[ab] Liang Han,[a] Yulin Zhu,[a] Paco Fernández-Trillo[b] and Feng He[ac]

Macromolecules, **2021**, 54 (11), 5278–5285

DOI: 10.1021/acs.macromol.1c00744

a. Shenzhen Grubbs Institute and Department of Chemistry, Southern University of Science and Technology, Shenzhen, 518055, China.
b. School of Chemistry, University of Birmingham, B15 2TT, UK.
c. Guangdong Provincial Key Laboratory of Catalysis, Southern University of Science and Technology, Shenzhen, 518055, China

Author contribution statement

H.L conceived and designed the study, prepared the samples, performed the experiments (unless otherwise stated), analyzed and interpreted the data, prepared and edited the manuscript. L.H edited the manuscript and confirmed synthesis by ^{1}H-NMR spectroscopy. Y.L.Z assisted in PPV synthesis. P.F.T and F.H conceived the study, interpreted the data, edited the manuscript and supervised H.L.

2.1 Abstract

Precisely controlled organic one-dimensional (1D) and two-dimensional (2D) materials with unique optoelectronic properties have attracted wide interests. By the introduction of chlorine into the poly(p-phenylenevinylene) (PPV) core, we produced a series of 1D rod-like micelles, whose sizes were controlled by the concentrations of solutions, using self-assembly (SA) of conjugated copolymers (PPV-$Cl_{20\%}$)$_{10}$-*b*-P2VP$_{20}$. The transformation from 1D rod-like micelles to 2D uniform diamond-like micelles was achieved by the thermally induced nucleation self-assembly. The sizes of the 2D diamond-like micelles could be tuned by the annealing temperature and the ratio of unimer to seed. It is demonstrated that the morphology transformation from rod-like micelles to diamond-like micelles was based on energetics including thermodynamic and kinetic points.

2.2 Introduction

The unique chemical reactivities and physical properties of one-dimensional (1D) and two-dimensional (2D) nanoscale materials have opened novel opportunities in the fields of catalysis,[1] biological nanomaterial,[2,3] and optoelectronic devices.[4,5] To achieve fascinating architectures in nanoscales, crystallization-driven self-assembly (CDSA) of block copolymers (BCP) is a widely used method, which is applied for fabricating 1D micelles[6] of cylinders, fibers, rods, and ribbons, as well as 2D platelet architectures with different shapes such as square,[7] rectangle,[8,9] hexagon,[10,11] raft,[12] and diamond. CDSA is a commonly used strategy to change nanomaterial dimensions,[13] especially living CDSA, which means that the addition of molecularly dissolved block copolymer (unimers) into seeds solution, leading to epitaxial growth and bypass spontaneous self-nucleation.[14] For example, BCPs based on polyferrocenylsilane (PFS)[15-17] have been reported over the past decade to fabricate unique 2D rectangular and lenticular platelet block co-micelles from 1D semicrystalline seeds by a living CDSA growth process.[18] Besides, copolymers with conjugated blocks have gradually become a promising foundation for the generation of functional 2D materials on account of the symmetry of the unit cell and relative structural rigidity.[19] For example, poly(p-phenylenevinylene) (PPV), as a classic π-conjugated polymer with attractive electronic and optical features, possesses conjugated backbones, resulting in an intense sheet-forming assembling tendency with tight π-π intermolecular packing.[20,21]

Recently, we demonstrated that 2D square and rhombic micelles with PPV-*b*-P2VP (P2VP= poly (2-vinyl pyridine)) could be achieved by the intermolecular π−π interactions between the conjugated PPV cores.[7,22] This has provided an approach to obtaining

platelets with low dispersion by a simple method. Using poly (3-hexylthiophene) (P3HT) based BCPs, 2D rectangular micelles could also be achieved, with their aspect ratios and sizes precisely controlled by the concentrations and the ratios of P3HT and PEG blocks.[8] From the perspective of the polymer structure design, we also successfully achieved 3D spiral architectures of PPV-*b*-PEG (PEG = poly (ethylene glycol)) BCPs by dislocation growth.[23] However, these self-assembly process driven by π–π interaction of conjugated blocks did not involve the morphology transformation of micelles in different dimensions, since it is still challengeable to obtain 1D and 2D micelles in the meantime.

Among most of the CDSA systems studied, morphology transformation from 1D to 2D and precise control over the shape and the size of the assembly architectures based on block copolymers could be well realized. Traditional CDSA utilizing heteroepitaxial growth with of different block ratios or different components by living seeded growth process showed good control over morphology change with hierarchical self-assembly.[17,19] However, it is difficult to transform the morphology when using the same copolymer molecule, which should involve the change of molecular arrangement. For driving molecular rearrangement to achieve homogeneous morphology change in different dimensions, external energy, as a key factor, should be induced into the self-assembly system.

From molecular design perspective, the introduction of chlorine into conjugated molecule improves intermolecular interactions and molecular crystallinity.[24] Herein, we reported the quantifiable introduction of chlorine to the side position of the PPV core and amphiphilic block copolymer based on them realized morphology transformation from 1D to the 2D structure by thermally induced nucleation self-assembly. Stable 1D rod-like

micelles were formed from the copolymers in isobutanol solution, and their sizes were controlled by the solution concentrations. Precise control over the scales of diamond-like micelles was realized by changing the annealing temperature or the ratio of unimer to seed. The transformation process of 2D diamond-like micelles from 1D micelles can be understood from the perspective of kinetic and thermodynamic points, which provides a new viewpoint for control over the morphology dimension between 1D and 2D nanomaterials.

2.3 Material and methods

2.3.1 Materials

Most of reagents and solutions were used as commercially received in synthesized procedures except dimethylformamide (DMF), potassium tert-butoxide (K*t*BuO), 1,1-diphenylethlene (DPE), 2-vinylpyridine (2VP), lithium chloride (LiCl), tetrahydrofuran (THF) and benzene. DMF was dried with molecular sieve before used. K*t*BuO and LiCl were heated at 120 °C under vacuum to remove water. DPE was titrated with n-BuLi until a red color sustained and then distilled under reduced pressure. 2VP was distilled with CaH_2 twice. THF and benzene was dried with Na and used as freshly distilled.

2.3.2 Experimental Methods

2.3.2.1 Characterization Equipment

^{1}H NMR spectra were measured on a Bruker AVANCE 400 MHz spectrometer with tetramethylsilane (TMS) as the internal standard. Molecular weights were determined by GPC measurements, which were carried out on a Waters ACQUITY APC System equipped with a UV detector (Waters ACQUITY TUV) and 3 series connected chromatographic columns (ACQUITY APC XT 450, 200, 45, 4.6 × 150 mm). Polystyrene standards (Aldrich) were used for calibration, and THF was used as the eluent with a flow rate of 0.5 ml min^{-1} at 40 °C. Matrix-assisted laser desorption/ ionization time of flight mass spectrometry (MALDI-TOF) mass spectrum were obtained on a Waters MICROMASS MALDI-TOF micro MX Mass Spectrometer. Small aliquots of sample solution (2 μL, 1.0 mg ml^{-1}) in chloroform were added to a sample plate for MOLDI-TOF. After drying in air at room temperature (about 10 min), an aliquot of α-cyano-4-hydroxy cinnamic acid (2 μL, 5.0 mg ml^{-1}) dispersed in a mixture of acetonitrile and water (acetonitrile/water = 1/1) was added and allowed to dry in air at room temperature.

2.3.2.2 Transmission electron microscopy

Transmission electron microscopy (TEM) photographs were taken by using a Hitachi HT7700 TEM instrument and operating at 100 kV. The samples were prepared by putting a drop of solution of assemblies on carbon-coated copper grids followed by solvent evaporated. For the statistical analysis, the achieved photos were analyzed by using Digital Micrograph software package developed by the US Gatan company. L_n is the number-average length and L_w is the weight-average length of 1D rod-like micelles, which were determined form the statistics of the length of 100 rod-like micelles with equation 2.1 and 2.2. The longer diagonal length was calculated to characterize the scale of the 2D diamond micelles. 100 2D diamond micelles from TEM images were traced by hand. D_{ln} (number-average length of the longer diagonal) and D_{lw} (weight-average length of the longer diagonal) of each sample of 2D diamond micelles were determined from these data by using equations 2.3 and 2.4, respectively (where D_l is the longer diagonal length of individual platelet 2D diamond micelles, N_i is the number of longer diagonal length).

$$L_n = \frac{\sum_{i=1}^{N} N_i L_i}{\sum_{i=1}^{N} N_i} \qquad \text{(Equation 2.1)}$$

$$L_w = \frac{\sum_{i=1}^{N} N_i {L_i}^2}{\sum_{i=1}^{N} N_i L_i} \qquad \text{(Equation 2.2)}$$

$$D_{ln} = \frac{\sum_{i=1}^{N} N_i D_{li}}{\sum_{i=1}^{N} N_i} \qquad \text{(Equation 2.3)}$$

$$D_{lw} = \frac{\sum_{i=1}^{N} N_i {D_{li}}^2}{\sum_{i=1}^{N} N_i D_{li}} \qquad \text{(Equation 2.4)}$$

2.3.2.3 Atomic force microscopy

The detected AFM samples were prepared by drop-coating about 15 μl of the 2-D assemblies' solution onto a pre-cleaned and treated silicon wafer followed by evaporating the solvent

isobutanol. The silicon wafers used as substrate were cleaned in piranha solution for 6 h, then ultrasound treated in ethanol, water, and ultrapure water in turn, and finally dried with blowing nitrogen. The images were gained using an Asylum Research AFM in AC mode under ambient conditions. The used sensor cantilevers were Silicon probe reflex coated with aluminum manufactured by Budget sensors Company. Images were analyzed with IGOR Pro software developed by WaveMetrics Inc.

2.3.2.4 UV-Vis Absorption Spectra (UV-Vis)

The PL spectra were recorded by a Shimadzu RF6000 spectrofluorometer. The samples were prepared by dissolving (PPV-$Cl_{20\%}$)$_{10}$-*b*-P2VP$_{20}$ in isobutanol under a concentration of 0.01 mg ml^{-1} and the prepared isobutanol solutions were heated at 90 °C for 1h, cooled to room temperature (25 °C), and aged for 24 h.

2.3.2.5 Grazing Incidence Wide-angle X-ray Scattering (GIWAXS)

The samples were prepared by drop-coating 60 μl of the solution onto the pre-cleaned and treated silicon wafer followed by evaporating the solvent for seven times. The silicon wafers were cleaned in piranha solution for 30 min, then ultrasound successively in ethanol, ultrapure water, and finally dried with blowing nitrogen dispersed.

2.3.2.6 Dynamic light scattering

Dynamic light scattering (DLS) measurements were performed by using a Brookhaven NanoBrook Omni laser light-scattering apparatus with a 635 nm red laser. The isobutanol solution of (PPV-$Cl_{20\%}$)$_{10}$-*b*-P2VP$_{20}$ was heated at 90 °C for 1 h and then spontaneously cooled to room temperature. After the sample solution was cooled to room temperature, the DLS was measured at 1h, 3h until aging for 24 h. On the other hand, the self-assembly sample was measured every day until 7 days.

2.3.2.7 Differential scanning calorimetry

Different scanning calorimetry (DSC) measurements were performed on a Discovery series thermal analyser at a scanning rate of 10 °C min^{-1} in N_2 atmosphere. The samples were heated from 30 to 150 °C, and then cooled back to 30 °C. The thermal cycles carried on twice, and the data of second cycle were used to analyse.

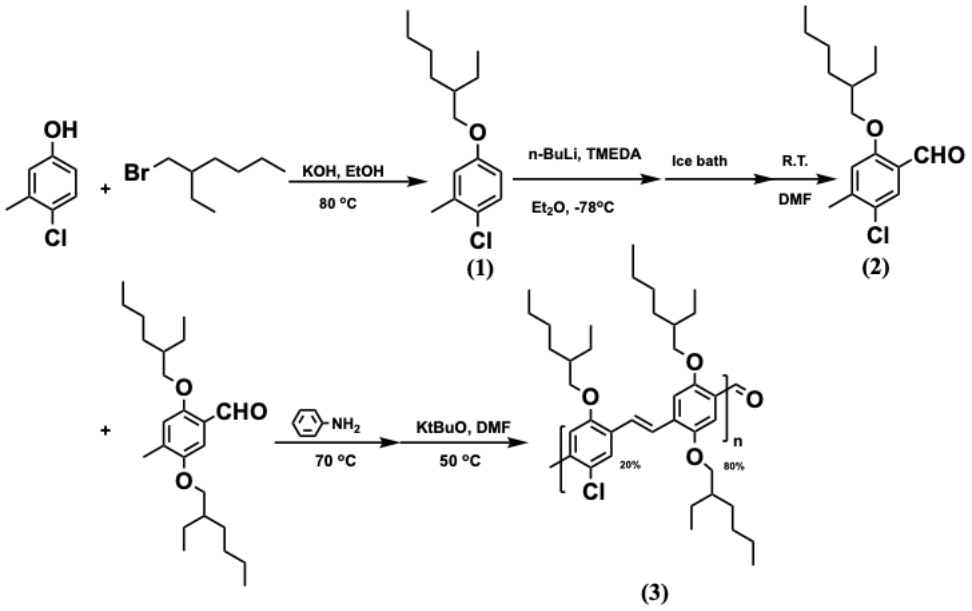

Scheme 2.1 Synthesis route of $(PPV\text{-}Cl_{20\%})_{10}$- CHO.

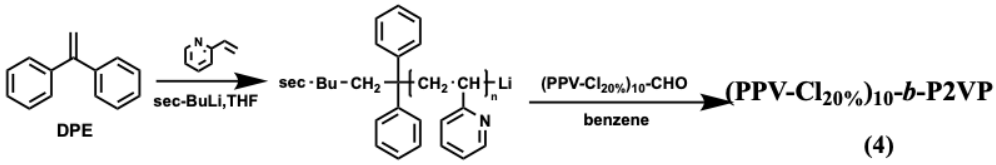

Scheme 2.2 Synthesis route for $(PPV\text{-}Cl_{20\%})_{10}$-*b*-$P2VP_{20}$.

2.3.2.8 Synthesis of 1-chloro-4-((2-ethylhexyl) oxy)-2-methylbenzene (1)

A mixture of 4-chloro-3-methylphenol (14.2 g, 0.1 mol) and KOH (16.42 g, 0.29 mol) in ethanol (170 ml) was refluxed at 80 °C for 1 h under Ar atmosphere. After that, 3-(bromomethyl) heptane (52 mL, 0.29 mol) was added to the stirring refluxing solution. The reaction was refluxed overnight. After cooling to room temperature, 700 mL water was added into mixture. The mixture was extracted with anhydrous ethyl acetate (3 × 100 mL), then the gathered organic phase was dried with $MgSO_4$, finally the solvent was removed by rotary evaporator. After purification by chromatography (silica gel, CH_2Cl_2/ petroleum ether 1:10), a yellow oil (**1**, 19.8 g, 0.078 mol, 77.89%) was obtained, which was determined by ^{1}H NMR (Appendix A, Figure A.1).

2.3.2.9 Synthesis of 5-chloro-2-((2-ethylhexyl) oxy)-4-methylbenzaldehyde (2)

1.61M hexanes solution of n-BuLi (2.7 ml, 6 mmol) was added to a -78ºC Diethyl ether solution (10 mL) of 1-chloro-4-((2-ethylhexyl) oxy)-2-methylbenzene (1.27g, 5 mmol) and TEMDA (1 ml, 6 mmol). After 0.5h at -78ºC, the mixture solution was transferred to an ice bath for 30 min. N, N-dimethylformamide (DMF, 4 ml) was added and maintained at room temperature for 3h. Then 6M aqueous HCl (aq) (1.7 ml, 10 mmol) was added and the mixture solution was extracted with ethyl acetate. Then the organic phase was washed with aqueous $NaHCO_3$. After dried by $MgSO_4$ and rotary evaporating, the obtained crude oil was purified by chromatography (silica gel, CH_2Cl_2: petroleum ether 1:7), a yellow oil (2, 1.12g, 3.95 mmol, 79%) was obtained, which was determined by ^{1}H NMR (Appendix A, Figure A.2).

2.3.2.10 Synthesis of PPV-$Cl_{20\%}$-CHO (3)

A mixture of 5-chloro-2-((2-ethylhexyl) oxy)-4-methylbenzaldehyde (compound 2, 1.12 g, 3.95 mmol), 2,5-bis(2-ethylhexyloxy)-4-methylbenzaldehyde (5.94 g, 15.8 mmol) and aniline (6.16 g, 66.06 mmol) was stirred for 2h at 50 °C under reduced pressure, then the temperature of

the mixture raised to 110 °C to remove excess aniline. The yielded deep yellow viscous oil. Next, the solution of yellow oil in 40 ml anhydrous DMF was added into round flask containing potassium tert-butoxide (2.25 g, 30 mmol) with 250 mL anhydrous DMF at 50 °C. After stirring for 1h at the same temperature, the mixture was poured into 250 mL 1M hydrochloric acid and stirred for 48 h. Then the reaction mixture was extracted with chloroform (3 × 10 ml), and the organic phase was successively washed by aqueous $NaHCO_3$ and water followed by dried with $MgSO_4$ and rotary evaporating. Product in low dispersity was successively collected and fractionated by methanol, acetone and hexane with Soxhlet extraction. The number-average degree of polymerization n = 10 for PPV-$Cl_{20\%}$-CHO was determined by ^1H NMR and mass (Appendix A, Figure A.3 and A.4). The polydispersity index was measured at 1.12 by GPC in THF (Figure A.5 and Table A.1).

2.3.2.11 Synthesis of PPV-$Cl_{20\%}$-P2VP (4)

In a glovebox filled with N_2, 86.9 μl of sec-BuLi (1.3 M in hexane) was quickly added to a stirring solution of dried LiCl (45.7 mg, 1.13 mmol) and 1,1-diphenylethylene (DPE, 20 μ, 0.113 mmol) in THF (2 ml) at -78 °C. Then maintaining -78 °C, 2-vinylpyridine (2VP) (296.75mg, 2.83 mmol) in THF (2 ml) was added to the mixture. After the reaction went on running for 2h at -78 ^oC, a solution of PPV-$Cl_{20\%}$-CHO (40 mg, 0.01mmol) in benzene (2 ml) was quickly added into the reaction mixture to quench the anion polymerization. Then the reaction temperature was increased to room temperature and stirred for additional 12 h. As the reaction stopped, the reaction mixture was poured into 25 ml chloroform and washed successively with aqueous HCl (pH = 3), water and aqueous $NaHCO_3$. After rotary evaporating, the crude residue was purified by chromatography (silica gel, eluent was changed from chloroform to chloroform/Et3N 9:1), and finally red solid (43.6 mg) was obtained. The conversion of P2VP is 80%. The block ratio of

produced (PPV-$Cl_{20\%}$)$_{10}$-*b*-P2VP$_{20}$ was determined by NMR (Figure A.6). The degree of polymerization of P2VP was 20 and $R_{PPV/P2VP}$ (the block ratio of PPV and P2VP) was ~1:2. After synthesis of diblock polymer, we performed GIWAXS experiments of EH-PPV-CHO and PPV-Cl-CHO (Appendix A, Figure A.7). It showed that the peak of PPV-Cl-CHO around 1.43 $Å^{-1}$ originating from π-π interactions was shaper and clearer than that of EH-PPV-CHO, which indicated that the introduction of Cl improved the molecular crystallinity.

2.4 Results and discussion

2.4.1 Formation of 1D rod-like micelles and preparation of fragment micelles

Self-assembly of (PPV-$Cl_{20\%}$)$_{10}$-*b*-P2VP$_{20}$ was carried out in isobutanol solution at concentrations of 0.01, 0.005, and 0.001 mg mL^{-1}. (PPV-$Cl_{20\%}$)$_{10}$-*b*-P2VP$_{20}$ was dissolved in the solvent by heating at 90 °C for 1 h then slowly cooled down to room temperature (RT) following by aging for 24 h. Uniform regular 1D rod-like micelles were formed in solutions at all three concentrations, observed by transmission electron microscopy (TEM) (Figure 2.1). The number-average length (L_n) of the micelles at 0.001 mg mL^{-1} was calculated to be 1833 nm and the length dispersity L_w/L_n = 1.05 (L_w = 1929 nm, L_w is the weight-average length), which was the most uniform among the three concentrations (Table A.3). As the concentration was increased, the lengths of the rod-like micelles clearly increased and the uniformity of the micelles diminished.

Then we explored the 2D self-assembly potential of (PPV-$Cl_{20\%}$)$_{10}$-*b*-P2VP$_{20}$ and chose the most uniform rod-like micelles formed in 0.001 mg mL^{-1} isobutanol for investigation. The micelle solution was sonicated at 0 °C for 10 min to obtain fragment solution. The sonication was performed at low temperature to avoid partial dissolution of the rod micelles due to the temperature increase of the solution. The fragment micelles were completely formed from 1D rod-like micelles observed after sonication (Figure A.9a).

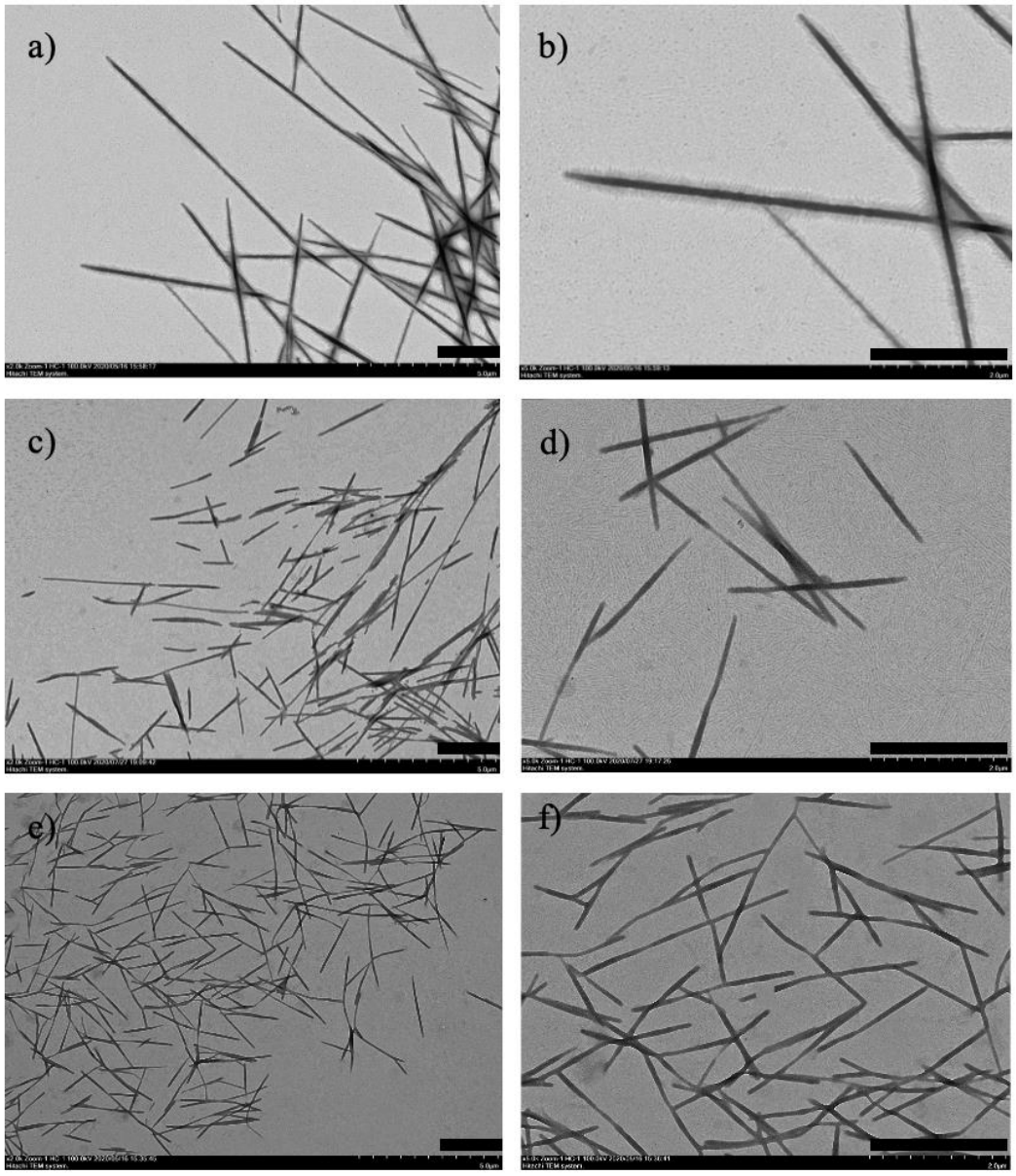

Figure 2.1 Transmission electron microscopy (TEM) images of 1D rod-like micelles of (PPV-$Cl_{20\%}$)$_{10}$-*b*-P2VP$_{20}$ prepared from isobutanol solutions with concentrations of (a, b) 0.01 mg ml^{-1}. (c, d) 0.005 mg ml^{-1}. (e, f) 0.001 mg ml^{-1}. Scale bars in the TEM images are 2 μm.

2.4.2 Formation of 2D diamond-like micelles by thermally induced nucleation self-assembly

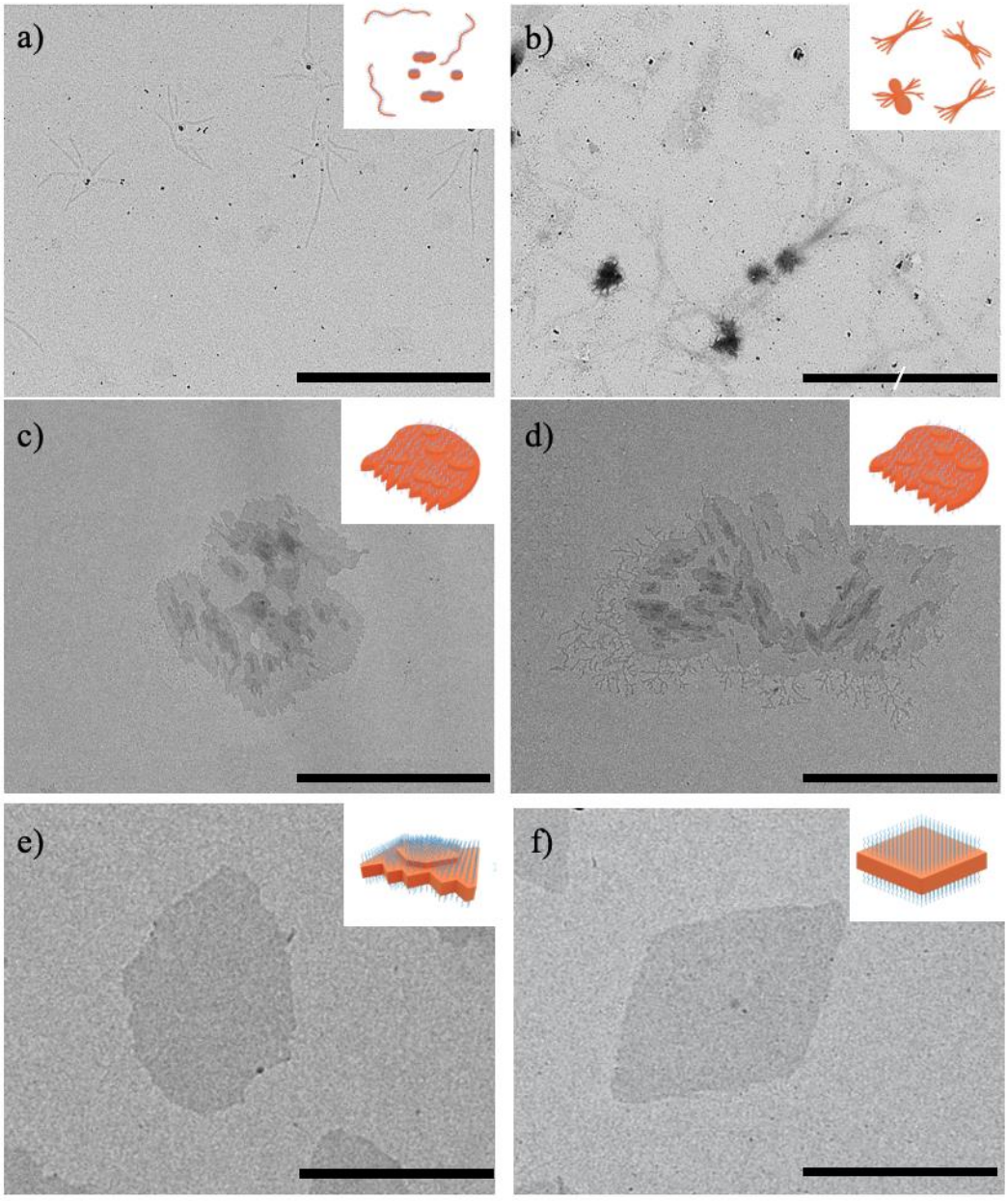

Figure 2.2 Schematic representation and TEM images of thermally induced nucleation growth process formed at 50 °C after aging for (a) 24 h; (b) 2 days; (c) 3 days; (d) 4 days; (e) 4.5 days; (f) 5 days. Scale bars in TEM photos are 2 μm.

Next, we attempted to reheat the solutions of (PPV-$Cl_{20\%}$)$_{10}$-*b*-P2VP$_{20}$ fragments of 0.001mg ml^{-1} in isobutanol at 40 °C, 50 °C and 60 °C, respectively, which are much lower than the initial heating temperature at 90°C for rod-like micelles. This aimed to avoid the arrangement of the

molecules in an original way as rod-like micelles. Then 10 μl THF solutions of $(PPV\text{-}Cl_{20\%})_{10}$-*b*-$P2VP_{20}$ unimers (0.025 mg) were added into the heated solutions. After shaking the solutions for 5 s, samples continued to be heated for an additional 1 h, cooled to RT. After aging for 1 day, some fiber- like structures appeared instead of original rod-like micelles while seed fragments still existed (Figure 2.2 a). However, when the blend solution was examined after aging for 48 h, it was found that the seed fragments and the fiber-like structures formed from unimers merged and grew, which gradually became a new nucleus. In 1-week, uniform 2D diamond-like micelles were produced and the morphology changing process was tracked by TEM. (Figure 2.2)

As shown in Figure 2.2, after aging for 24 h, the additional unimers showed the tendency to form 1D fiber-like micelles, while the seed fragments exhibited another kind of growth involving side-by-side attachment to each other at the same time (Figure 2.2a).[25] Subsequently, the fiber-like micelles began parallel stacking and acted as a glue with the spontaneous seed-to-seed attachment formed a larger nucleus (Figures 2.2b, c).[26] The larger nucleus with a new arrangement of molecule underwent epitaxial growth with a dim outline of 2D morphology (Figure 2.2d), and finally became the well-defined 2D diamond-like micelles (Figures 2.2e and 2.3). In all, to achieve morphology transformation of different dimensions, we introduced external thermal in the process combining self-seeding with seeded growth and tried to change molecular assembled states. Then we successfully obtained new assembled architecture and found that the significant step of transformation from rod-like to diamond-like micelles is thermally induced nucleation process, where the seeds suffered a re-activation stage at first and aggregated into activated nuclear with 2D growing tendency.

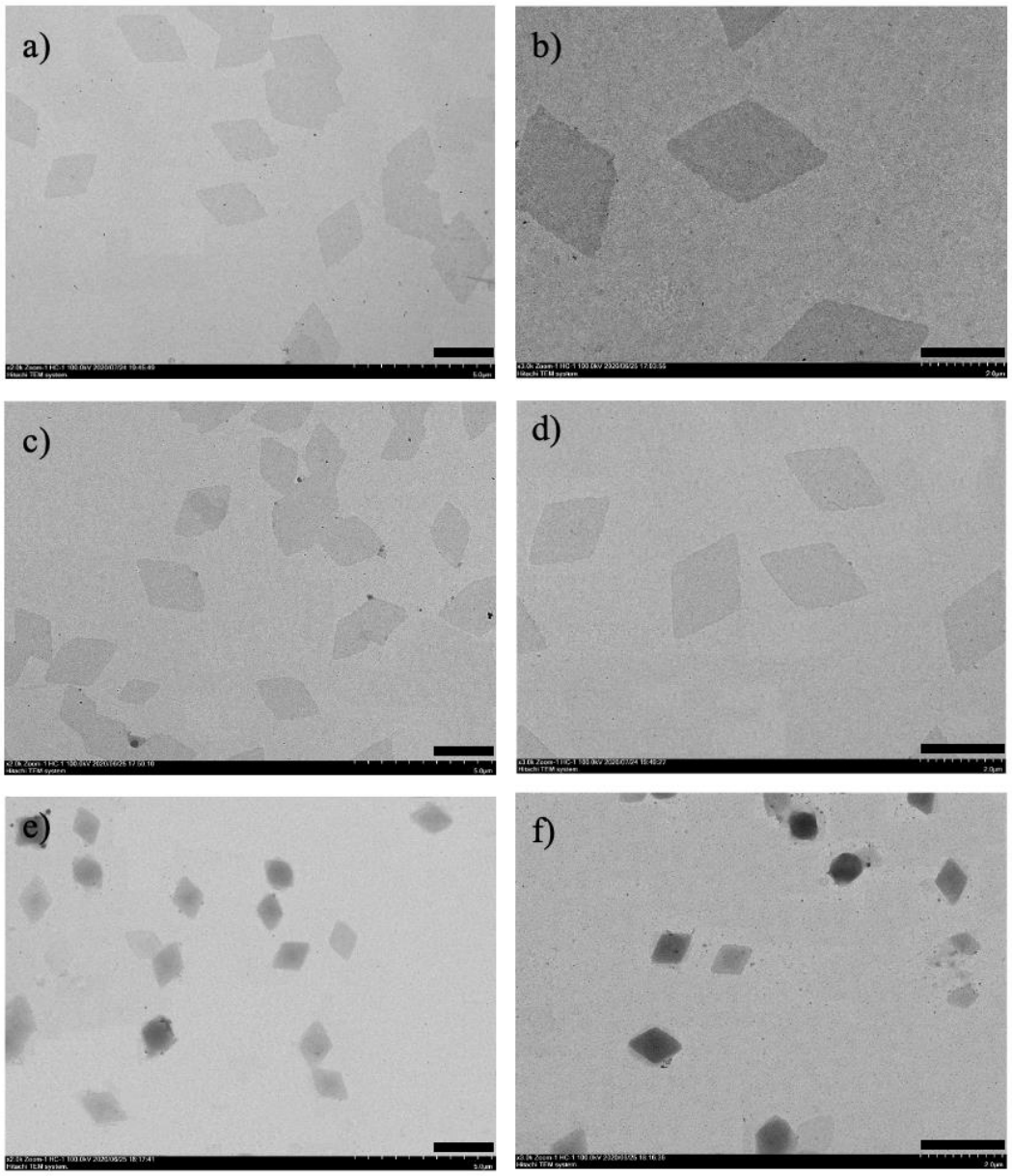

Figure 2.3 TEM images of 2D diamond-like micelles prepared from (PPV-$Cl_{20\%}$)$_{10}$-*b*-P2VP$_{20}$ at different annealing temperatures in isobutanol. (a, b) 40 ^{o}C; (c, d) 50 ^{o}C; (e, f) 60 ^{o}C. Scale bars in TEM photos are 2 μm.

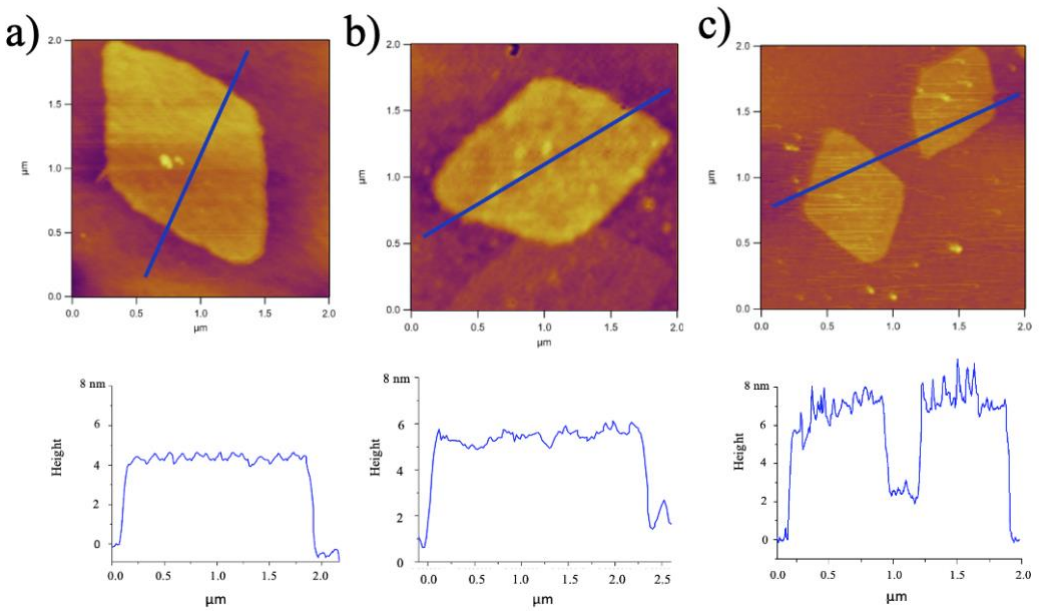

Figure 2.4 AFM height images of 2D diamond-like micelles formed at different annealing temperatures in isobutanol. (a) 40 ºC; (b) 50 ºC; (c) 60 ºC.

TEM analysis indicated that the scales of the diamond-like micelles depended on the temperature of nucleation. D_{ln} (the number-average diagonal length) of the formed diamond-like micelles annealing at 40 °C was calculated to be 2973 nm. The length dispersity D_{lw}/D_{ln} = 1.04 where D_{lw} (the weight-average diagonal length of the longer diagonal) was 3118 nm (Figure A.8a, Table A.3). In the case of diamond-like micelles formed at 50 °C, D_{ln} = 2316 nm and D_{lw} = 2406 nm. As the temperature was increased to 60 °C, the value of D_{ln} decreased continuously to 1535 nm. It was obviously observed that the size of the diamond-like micelles decreased and the uniformity of the micelles improved as the annealing temperature increased (Figure A.8d). Atomic force microscopy (AFM) characterization showed similar results to the TEM observation concerning the size of 2D diamond-like micelles formed at the different annealing temperatures. (Figure 2.4). However, it was clear that the thickness of the micelles formed at different annealing temperatures changed very little. Their height of 5-7 nm indicated that the molecules should adopt

monolayer packing in the new arrangement which was consistent with the previously reported PPV-based 2D sheet structures.[21]

2.4.3 Energetics of the transformation from 1D rod-like micelles to 2D diamond-like micelles

To understand more details of the thermally induced nucleation self-assembly process, the comparison experiment was carried out, in which a THF solution of the unimer was added to isobutanol at 50 °C in the absence of the seed fragments (Figure A.9c). However, in the absence of the seed fragments for the 2D nucleus, to provide growth sites, only poorly defined and highly aggregated 2D platelet structures were formed. In a second contrast experiment, seed fragment solutions of $(PPV\text{-}Cl_{20\%})_{10}$-b-$P2VP_{20}$ were heated at 50 °C without additional unimer but following the same procedure as the above thermally induced nucleation self-assembly approach of diamond-like micelles (Figure A.9b). In this experiment, the seed fragments simply aggregated to form star-like plane architectures by side-to-side attachment instead of the original rod-like morphology, which proved that the original molecular arrangement was broken. The tendency of side-to-side seed attachment led to the formation of the new nucleus and subsequent growth along the plane at the sides of the fragment micelles, rather than along the longitudinal axis at the end of seed fragments. Next, we examined the importance of reheating in the whole process. The unimer solution was added into the seed solution at RT without externally heating, and after aging for one week, the mixture of 1D fiber like micelles from the unimer and irregular aggregates probably formed from seed fragments were present (Figure A.9d). This result revealed that the seed fragments could not become nuclear and continue subsequent 2D growth without reheating process. In summary, the self-assembly method to achieve the transformation from 1D to the 2D structure is caused by thermally induced nucleation.

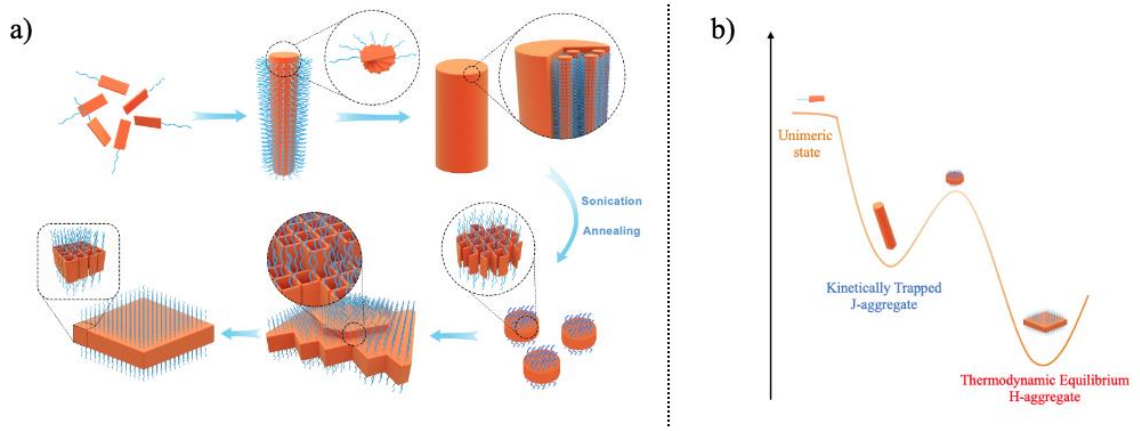

Figure 2.5 (a) Proposed transformation from 1D rod-like micelles to 2D diamond-like micelles by the thermally induced nucleation self-assembly process involving (PPV-$Cl_{20\%}$)$_{10}$-*b*-P2VP$_{20}$; (b) Energetics schematic diagram of the self-assembly of (PPV-$Cl_{20\%}$)$_{10}$-*b*-P2VP$_{20}$.

To understand more details of the morphology transformation process from 1D rod-like structure to 2D diamond-like micelles, we measured the variable UV-Vis absorption spectra (Figure A.10) and dynamic light scattering (DLS) (Figure A.11) during the self-assembly progress at different annealing temperatures. In the growth process of rod micelles formed in isobutanol solution at a concentration of 0.01 mg mL^{-1}, the UV-Vis spectra of (PPV-$Cl_{20\%}$)$_{10}$-*b*-P2VP$_{20}$ at 90 °C has a peak at 439 nm, where (PPV-$Cl_{20\%}$)$_{10}$-*b*-P2VP$_{20}$ were completely dissolved without aggregation. A slight redshift was observed during the cooling process, indicating that freely moving BCP molecules had begun to aggregate as a result of the hydrophobic interactions of the conjugated core and the side chains. Afterwards, there was an obvious redshift of 23 nm of the absorption maximum accompanied by the appearance of a shoulder peak at 477 nm during the aging time from 1 h to 3 h. Then no further change was shown in the spectra for the following aging time. The redshift of the absorption in the aging process could be attributed to a kind of slipped face-to-face stacking of conjugated cores, which was adopted to form the rod-like micelles,

resulting in the appropriate "J-aggregation" characteristics. (Figure 2.5a) This dislocation stacking mode between the conjugated cores in the rod micelles is quite different from the reported typical "H-aggregation" of the similar PPV cores[7] in 2D square micelles. This is because the introduction of chlorine to the side chain of PPV results in better crystallization, poorer solubility of BCPs, and a faster aggregation rate during the aging process. Meanwhile, the apparent hydrodynamic diameter (D_h) of the micelles was monitored by DLS, which treated the micelles as spherical particles.[25] From 3 h to 24 h, the increasing rate of the particle size was slower than that from 1 h to 3 h. In the 0.01 mg mL^{-1} solution, the aggregated particle gradually grew, and the size of the structure after aging for 24 h was much bigger than that in the 0.005 mg mL^{-1} solution (Figure A11a). Overall, freely moving molecules of (PPV-$Cl_{20\%}$)$_{10}$-*b*-P2VP$_{20}$ in the solution began to aggregate, driven by hydrophobic interactions during the cooling process. A faster aggregation rate due to the chlorine substitution caused an insufficient and slipped intermolecular π-π stacking between rigid conjugated PPV blocks to form 1D rod-like micelles, which should be the kinetically trapped state (Figure 2.5a). The UV-Vis absorption spectra were observed as a measure of the aging time in the thermally induced nucleation SA process in which the BCP solutions were annealed at 40 °C, 50 °C and 60 °C, respectively. For all three annealing temperatures, the spectra showed similar changes (Figures A10b-d). In the formation of 2D diamond-like micelles heated at 40 °C, after aging for 1 day, the UV–Vis spectra of (PPV-$Cl_{20\%}$)$_{10}$-b-P2VP$_{20}$ showed a maximum at 451 nm accompanied by a shoulder at 468 nm. This indicated that the additional unimers were starting to aggregate to form small 1D fiber-like micelles, consistent with the TEM image (Figure 2.2a). There was a significant decrease in the absorption intensity of the shoulder peak during the next 2 days. Finally, the shoulder peak completely disappeared and the spectral maximum showed

a slight blue shift. The phenomenon revealed that the BCPs aggregates have formed H-aggregation from initial J-aggregation.[7,21]

The variation of the UV-Vis spectra revealed that 1D fiber micelles continued to attach to the new nucleus and well-defined 2D diamond-like micelles were formed by epitaxial growth with new molecular packing in the face-to-face arrangement, which should be the thermodynamic equilibrium state.[7,8] Differential scanning calorimetry (DSC) measurement was also carried out to characterize the change of the molecular states (Figure A.12). (PPV-$Cl_{20\%}$)$_{10}$-CHO showed T_g (glass transition temperature) at 58 ℃ and T_c (crystalline transition temperature) at 107 ℃, respectively. Compared with (PPV-$Cl_{20\%}$)$_{10}$-CHO, (PPV-$Cl_{20\%}$)$_{10}$-*b*-$P2VP_{20}$ showed the same T_g (58 ℃) but Tc disappeared, which indicated that the crystallinity of (PPV-$Cl_{20\%}$)$_{10}$-*b*-$P2VP_{20}$ got decreased and the formation of the assembled structure seemed to suffer a phase transition dominated by PPV-$Cl_{20\%}$ blocks. The temperature of initial self-assembly (90 °C) is above the T_g, which represents that the polymer undergoes phase transition and the movement of polymer chains change. The temperature of forming diamond-like micelles is less than or near the T_g. It reveals that the formation of the 2D micelles is totally different from 1D rod-like micelles, without the phase transition and the movement of polymer chains changing. To achieve the morphology transformation, the thermal energy should be induced into the self-assembled system to re-activate.

From the above results, including the TEM, AFM, DLS, DSC and UV-Vis absorption spectra, the energetics schematic representation of the entire self-assembly process from 1D rod-like micelles to 2D diamond-like micelles is depicted in Figure 2.5b. According to the lowest energy principle, the more stable the system is, the lower the energy is. For our assembly system, the formed 1D or 2D architectures are stable states, so they should be in lower energy, while the molecular states in solvents with intense movement should be in higher energy in the energetics

schematic diagram (Figure 2.5b), but it should be noted that this displayed process represents an oversimplification of a complex situation.[14] Upon cooling the isobutanol solution from 90°C above the glass transition temperature (56 °C), polymers in the unimeric state started to rapidly aggregate as shown in Figure 2.5a due to the poor solubility and intermolecular forces between chlorine and oxygen of PPV-Cl. In this way, 1D rod-like micelles, which represent a kinetically trapped state were formed. After sonication and heating treatment on these 1D rod-like micelles, small fragments with an ordered core emerge and are capable of initiating further seeded (epitaxial) growth of unimers. As the unimer solution was blended into the seed solution at annealing temperature, the 2D nucleus gradually formed and the molecules should arrange in a new way. The tendency of subsequent growth based on the new nucleus should be a more ordered pathway in comparison with 1D morphology (Figure 2.5a), and 2D diamond-like micelles were ultimately formed, representing a thermodynamic equilibrium state. As the morphology transformation are achieved, the thermal energy inducing the self-assembled system to re-activate should be key factor. It seems there should be a metastable state during the morphology transformation, whose energy is between the molecular states dissolved in solvents and molecular states in the self-assembly structures. Therefore, the thermal should be induced into the self-assembled system to overcome an activation barrier, which resulted in the morphology transformation from 1D to 2D by thermally induced nucleation self-assembly.

2.4.4 Tuning the scale of the diamond-like micelles by varying the unimer/seed ratio (m_{unimer}/m_{seed})

As stated above, the 2D growth of the micelles is greatly affected by annealing temperatures. The morphology of the diamond-like micelles should be tuned by the change of m_{unimer}/m_{seed}. To realize more accurate control of the thermally induced nucleation self-assembly process, the self-

assembly system of $(PPV\text{-}Cl_{20\%})_{10}$-b-$P2VP_{20}$ heating at 60°C was chosen because of the good uniformity and morphology demonstrated by the TEM analysis (Table A.4). After sonication and heating, 10 μL of THF solutions containing different amounts of $(PPV\text{-}Cl_{20\%})_{10}$-b-$P2VP_{20}$ unimers (0.010, 0.025, 0.030, 0.040 mg) were respectively added into the seed fragment in 1 ml isobutanol solutions using the aforementioned approach. After 5 s shaking, all four solutions were allowed to anneal at 60°C for 1 h and then aged for one week. The TEM images in Figure 2.6 showed that the achieved micelles were all uniform with a narrow polydispersity ($1.01 < Đ\ (D_{ln}/D_{lw}) < 1.05$) (Table A.5). There was a linear relationship between their weight-average diagonal length D_{lw} and m_{unimer}/m_{seed} (Figure 2.6e), and the A_n (average area) of diamond micelles also increased as m_{unimer}/m_{seed} (Figure 2.6f). When $m_{unimer}/m_{seed} = 10$, the D_{ln} of 2D micelles reduced to 453 nm (D_{lw} = 463 nm, D_{lw}/D_{ln}=1.04), the scale of the formed nanostructures was clearly smaller than the original micelles (m_{unimer}/m_{seed} =25) (D_{ln} = 1535 nm), and part of morphologies tended to be 2D square structure. The reason for the slight change of the morphology of 2D nanostructure could be that the small amount of the unimers led to an insufficient process of epitaxial growth along both diagonals. This indicated that after thermally induced nucleation, additional unimers took a key role in the following epitaxial growth process as well as the final shaping process. On the other hand, the D_{ln} and D_{lw} values of the diamond-like micelles formed in the $(PPV\text{-}Cl_{20\%})_{10}$-b-$P2VP_{20}$ solution, when the ratio of unimer to seed was 30, were calculated to be 2306 nm and 2398 nm, respectively (Đ = 1.04). As the ratio of unimer to seed increased, the scales of the diamond-like micelles obviously increased and the integrity of the 2D micelles improved. When m_{unimer}/m_{seed} was increased to 40, the D_{ln} and D_{lw} of obtained diamond-like micelles were 2805 nm and 2858 nm and these larger diamond-like micelles packed together easily. Consequently, the weight-

average diagonal lengths D_{lw} of the platelet diamond-like micelles of $(PPV\text{-}Cl_{20\%})_{10}$-b-$P2VP_{20}$ can be linearly tuned by changing m_{unimer}/m_{seed}.

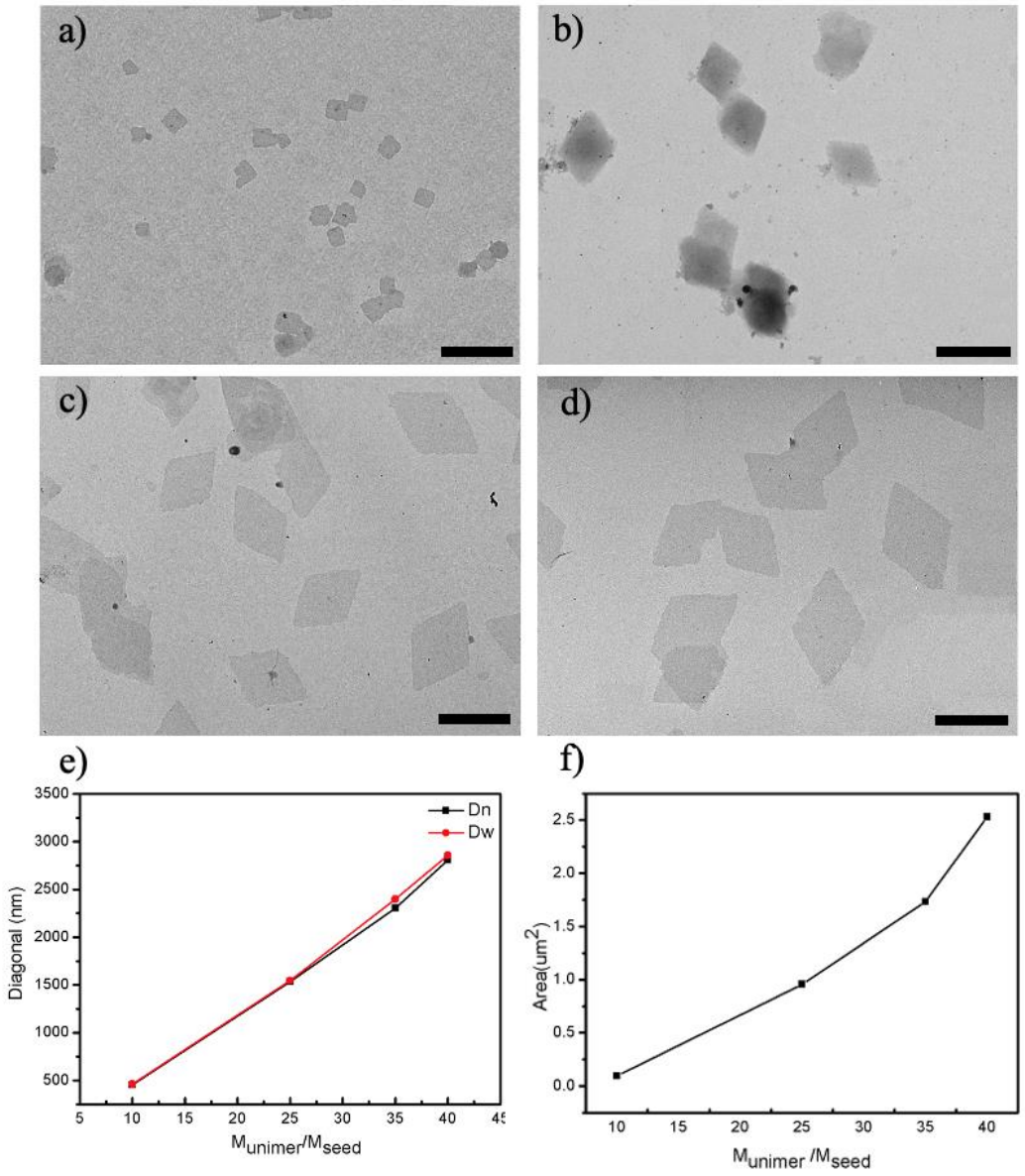

Figure 2.6 TEM images of 2D diamond-like micelles prepared from $(PPV\text{-}Cl_{20\%})_{10}$-*b*-$P2VP_{20}$ formed from m_{unimer}/m_{seed} ratios as (a)10 (b) 25 (c) 35 (d) 40. Scale bars in TEM photos are 2 μm. (e) Number-average length (D_{ln}) and weight-average diagonal length (D_{lw}) of diamond-like

micelles of (PPV-$Cl_{20\%}$)$_{10}$-*b*-P2VP$_{20}$ vs unimer to seed ratio (m_{unimer}/m_{seed}) formed at 60°C. (f) Area (A_n) of diamond-like micelles of (PPV-$Cl_{20\%}$)$_{10}$-b-P2VP$_{20}$ vs unimer to seed ratio (m_{unimer}/m_{seed}) formed at 60°C.

2.5 Conclusions

In summary, we utilized thermally induced nucleation self-assembly to control the conversion from 1D rod-like micelles to uniform 2D diamond-like micelles by preparing a PPV-*b*-P2VP copolymer that incorporated 20% of a chloride-substituted monomer in the PPV core. First, we prepared 1D rod-like micelles with precise control over their sizes by changing the concentrations of BCPs in solutions. Transformation from 1D rod-like micelles to 2D diamond-like micelles was achieved by the thermally induced nucleation process that lets the kinetically trapped 1D nanostructures to overcome the activation barrier to reach the thermodynamic state of the 2D nanostructure. The scales of the 2D diamond-like micelles could be precisely controlled by adjustment of the annealing temperature. The size of the 2D diamond-like micelles can be also effectively tuned by controlling the unimer-to-seed ratio. These 1D or 2D nanomaterials that have fluorescent and semiconducting properties could be potential candidates for applications in biosensors, catalysis, and optoelectronics.

2.6 References

[1] Zhong Y.; Wang Z.; Zhang R.; Bai F.; Wu H.; Haddad R.; Fan H., Interfacial Self-Assembly Driven Formation of Hierarchically Structured Nanocrystals with Photocatalytic Activity. ACS Nano 2014, 8 (1), 827-833.

[2] Wang L.; Gong C.; Yua, X.; Wei G., Controlling the Self-Assembly of Biomolecules into Functional Nanomaterials through Internal Interactions and External Stimulations: A Rev. Nanomater. 2019, 9 (2), 285.

[3] Brodin J. D.; Ambroggio X. I.; Tang C.; Parent K. N.; Baker T. S.; Tezcan F. A., Metal-directed, chemically tunable assembly of one-, two- and three-dimensional crystalline protein arrays. Nat. Chem. 2012**,** 4 (5), 375-382.

[4] Ferrari A. C.; Bonaccorso,F.; Fal'ko V.; Novoselov K. S.; Roche S.; Bøggild P.; Borini S.; Koppens F. H. L.; Palermo V.; Pugno N.; Garrido J. A.; Sordan R.; Bianco A.; Ballerini L.; Prato M.; Lidorikis E.; Kivioja J.; Marinelli C.; Ryhänen T.; Morpurgo A.; Coleman J. N.; Nicolosi V.; Colombo L.; Fert A.; Garcia-Hernandez M.; Bachtold A.; Schneider G. F.; Guinea F.; Dekker C.; Barbone M.; Sun Z.; Galiotis C.; Grigorenko A. N.; Konstantatos G.; Kis A.; Katsnelson M.; Vandersypen L.; Loiseau A.; Morandi V.; Neumaier D.; Treossi E.; Pellegrini V.; Polini M.; Tredicucci A.; Williams G. M.; Hee Hong, B.; Ahn J.H.; Min Kim, J.; Zirath H.; van Wees B. J.; van der Zant H.; Occhipinti L.; Di Matteo A.; Kinloch I. A.; Seyller T.; Quesnel E.; Feng X.; Teo K.; Rupesinghe N.; Hakonen P.; Neil S. R. T.; Tannock Q.; Löfwander, T.; Kinaret J., Science and technology roadmap for graphene, related two-dimensional crystals, and hybrid systems. Nanoscale 2015, 7 (11), 4598-4810.

[5] Matsui J.; Mitsuishi, M.; Aoki A.; Miyashita T., Molecular Optical Gating Devices Based on Polymer Nanosheets Assemblies. J. Am. Chem. Soc. 2004, 126 (12), 3708-3709.

[6] Gilroy J. B. Gädt T.; Whittell G. R.; Chabanne L.; Mitchels J. M.; Richardson R. M.; Winnik, M. A.; Manners, I., Monodisperse cylindrical micelles by crystallization-driven living self-assembly. Nat. Chem. 2010, 2 (7), 566-570.

[7] Han L.; Wang M.; Jia X.; Chen W.; Qian,H.; He F., Uniform two-dimensional square assemblies from conjugated block copolymers driven by π–π interactions with controllable sizes. Nat. Commun. 2018, 9 (1), 865.

[8] Qi R.; Zhu Y.; Ha L.; Wang, M.; He F., Rectangular Platelet Micelles with Controlled Aspect Ratio by Hierarchical Self-Assembly of Poly(3-hexylthiophene)-b-poly (ethylene glycol). Macromolecules 2020, 53 (15), 6555-6565.

[9] Feng C.; Jose Gonzalez-Alvarez, M.; Song Y.; Li, I.; Zhao G.; Molev G.; Guerin G.; Walker G.; Scholes G. D.; Manners I.; Winnik M. A., Synthesis, self-assembly and photophysical properties of oligo (2,5-dihexyloxy-1,4-phenylene vinylene)-block-poly (ethylene glycol). Soft Matter 2014, 10 (44), 8875-8887.

[10] Su M.; Huang H.; Ma, X.; Wang, Q.; Su, Z., Poly(2-vinylpyridine)-block -Poly(ϵ-caprolactone) Single Crystals in Micellar Solution. Macromol. Rapid. Commun. 2013, 34 (13), 1067-1071.

[11] Ganda S.; Dulle M.; Drechsler M.; Förster B.; Förster S.; Stenzel M. H., Two-Dimensional Self-Assembled Structures of Highly Ordered Bioactive Crystalline-Based Block Copolymers. Macromolecules 2017, 50 (21), 8544-8553.

[12] Rizis G.; van de Ven,T. G. M.; Eisenberg, A., "Raft" Formation by Two-Dimensional Self-Assembly of Block Copolymer Rod Micelles in Aqueous Solution. Angew. Chemie 2014, 126 (34), 9146–9149.

[13] Fan B.; Wang R.; Wang, X.; Xu, J.; Du, B.; Fan Z., Crystallization-Driven Co-Assembly of Micrometric Polymer Hybrid Single Crystals and Nanometric Crystalline Micelles. Macromolecules 2017, 50 (5), 2006–2015.

[14] Fukui T.; Garcia-Hernandez J. D.; MacFarlane L. R.; Lei S.; Whittell G. R.; Manners I., Seeded Self-Assembly of Charge-Terminated Poly(3-hexylthiophene) Amphiphiles Based on the Energy Landscape. J. Am. Chem. Soc. 2020, 142 (35), 15038-15048.

[15] Cao L.; Manners I.; Winnik M. A. Influence of the Interplay of Crystallization and Chain Stretching on Micellar Morphologies: Solution Self-Assembly of Coil−Crystalline Poly(isoprene-*block*-ferrocenylsilane). Macromolecules 2002, 35, 8258 - 8260.

[16] Pearce S.; He X.; Hsiao M. S.; Harniman R. L.; MacFarlane L. R.; Manners I., Uniform, High-Aspect-Ratio, and Patchy 2D Platelets by Living Crystallization-Driven Self-Assembly of Crystallizable Poly(ferrocenyldimethylsilane)-Based Homopolymers with Hydrophilic Charged Termini. Macromolecules 2019, 52 (16), 6068-6079.

[17] Nazemi A.; He X.; MacFarlane L. R.; Harniman R. L.; Hsiao M. S.; Winnik M. A.; Faul C. F. J.; Manners I., Uniform "Patchy" Platelets by Seeded Heteroepitaxial Growth of Crystallizable Polymer Blends in Two Dimensions. J. Am. Chem. Soc. 2017, 139 (12), 4409-4417.

[18] Qian J.; Lu Y.; Chia A.; Zhang M.; Rupar P. A.; Gunari N.; Walker G. C.; Cambridge G.; He F.; Guerin, G.; Manners, I.; Winnik, M. A., Self-Seeding in One Dimension: A Route to Uniform Fiber-like Nanostructures from Block Copolymers with a Crystallizable Core-Forming Block. ACS Nano 2013, 7 (5), 3754-3766.

[19] Qiu H.; Gao Y.; Boott C. E.; Gould O. E. C.; Harniman R. L.; Miles, M. J.; Webb, S. E. D.; Winnik, M. A.; Manners, I., Uniform patchy and hollow rectangular platelet micelles from crystallizable polymer blends. Science 2016, 352 (6286), 697-701.

[20] Günes S.; Neugebauer H.; Sariciftci N. S., Conjugated Polymer-Based Organic Solar Cells. Chem. Rev. 2007, 107 (4), 1324-1338.

[21] Elacqua E.; Croom A.; Manning K. B.; Pomarico S. K.; Lye D.; Young L.; Weck M., Supramolecular Diblock Copolymers Featuring Well-defined Telechelic Building Blocks. Angew. Chem., Int. Ed. 2016, 55 (51), 15873-15878.

[22] Han L.; Fan H.; Zhu Y.; Wang M.; Pan F.; Yu D.; Zhao Y.; He F., Precisely Controlled Two-Dimensional Rhombic Copolymer Micelles for Sensitive Flexible Tunneling Devices. CCS Chem. 2020, 2, 1399-1409

[23] Zhu Y.; Han L.; Fan H.; Wang M.; Qi, R.; Zhao, Y.; He, F., Three-Dimensional Spirals of Conjugated Block Copolymers Driven by Screw Dislocation. Macromolecules 2020, 53 (8), 3217-3223.

[24] Lai H.; He F., Crystal Engineering in Organic Photovoltaic Acceptors: A 3D Network Approach. Adv. Energy Mater. 2020, 10, 1–16.

[25] Qiu H.; Hudson Z. M.; Winnik M. A.; Manners I., Multidimensional hierarchical self-assembly of amphiphilic cylindrical block comicelles. Science 2015, 347 (6228), 1329-1332.

[26] Yang S.; Kang S. Y.; Choi T. L., Morphologically Tunable Square and Rectangular Nanosheets of a Simple Conjugated Homopolymer by Changing Solvents. J. Am. Chem. Soc. 2019, 141 (48), 19138-19143.

CHAPTER 3 MORPHOLOGICAL TRANSITION AND TRANSFORMATION OF 2D PLATELETS BY CONTROLLING BALANCE OF π−π STACKING INTERACTION AND CRYSTALLINE DRIVEN FORCE

Paper under review

Heng Li,[ab] Liang Han,[a] Yulin Zhu,[a] Nan Zheng,[d] Paco Fernández-Trillo[bc] and Feng He[af]

Materials Horizons, **2022**, major revision.

a. Shenzhen Grubbs Institute and Department of Chemistry, Southern University of Science and Technology, Shenzhen, 518055, China.
b. School of Chemistry, University of Birmingham, B15 2TT, UK.
c. Departamento de Química, Facultade de Ciencias and Centro de Investigacións Científicas Avanzadas (CICA), Universidade da Coruña A Coruña, 15071, Spain.
d. Institute of Polymer Optoelectronic Materials and Devices, State Key Laboratory of Luminescent Materials and Devices, South China University of Technology, Guangzhou 510640, China.
f. Guangdong Provincial Key Laboratory of Catalysis, Southern University of Science and Technology, Shenzhen, 518055, China

Author contribution statement

H.L conceived and designed the study, prepared the samples, performed the experiments (unless otherwise stated), analyzed and interpreted the data, prepared and edited the manuscript. L.H edited the manuscript and confirmed synthesis by ^{1}H-NMR spectroscopy. Y.L.Z assisted in AFM and synthesis. N.Z assisted in GIWAXS. P.F.T and F.H conceived the study, interpreted the data, edited the manuscript and supervised H.L.

3.1 Abstract

Nanoscale organic one-dimensional (1D) and two-dimensional (2D) materials of block copolymers (BCPs) have attracted interests on account of widely potential applications in a range of fields. Herein, we designed a new poly (p-phenylenevinylene) (PPV) based BCP that contains triisopropylsilyl (TIPS) side chain and poly (2-vinyl pyridine) (P2VP) corona, which could assemble into a series of 2D square and rectangular micelles in isopropanol. The aspect ratios and the scales of the 2D micelles could be tuned in two ways, including the ratios of P2VP and PPV-TIPS blocks and the concentrations. By precisely controlling the aspect ratios, the micro-scale rod-like micelles were also obtained. In depth studies of the morphology transition from rectangular micelles to rod-like or square micelles, it is found that the BCPs initially organized into fibers and then assembled into final micelles by the combination forces of π–π interactions and the crystalline force based on TIPS side chains.

3.2 Introduction

As widely applied in a range of applications owing to their ultrathin platelet morphology, nanoscale 1D and 2D structures based on amphiphilic BCPs have attracted a great deal of attention.[1] Recently, the 2D nanosheet has opened new and exciting opportunities in organic optoelectronic devices[2] and biological nanomaterials[3]. Over the past years, various 2D structures in micro- and nano-scale have been made from organic molecules[4], peptides[5], and block copolymers. Among all these methods, the bottom-up self-assembly of homopolymers and BCPs with the crystalline core in solution is a commonly used strategy. Self-assembly through crystalline core-forming block can achieve well-defined 2D platelet architectures with various shapes of square[6], rectangular[7,8], hexagon[9], diamond[10,11], and leaves[12], based on the symmetrical crystal unit cell of BCPs. These core crystalline blocks can be varied from nonconjugated polymers, such as polyferrocenylsilane[13, 14] polyethylene (PE),[15] and poly(lactic acid) (PLLA)[16] to conjugated BCPs including poly(3-hexylthiophene) (P3HT)[7].

Poly(p-phenylenevinylene), as a classic and well-known π-conjugated material, possesses attractive optical and electronic features. The conjugated backbone makes PPV achieve tight intermolecular packing with intense sheet-forming assembling tendency.[17,18] Recently, we have reported 2D micelles with morphologies of square, scarf, and diamond micelles based on PPV with different alkyl chains modified by SA methods.[6,11,19] For the formation of these 2D architectures, the driven force was led by π–π interactions between conjugated core blocks. If crystallization as another kind of driven force was introduced, exploring its effect on the SA process of these 2D micelles will be an interesting research project.

Herein, to investigate the influence of the crystallinity on BCP self-assembly, we designed a new PPV core containing a bulky triisopropylsilyl (TIPS) group, which possesses good crystallinity, at the side chain and combined it with P2VP to construct amphiphilic BCPs for SA.[20] The morphological transition from 2D square to rectangular or rod-like micelles with adjustable aspect ratios based on these copolymers was achieved through changing solution concentrations or the lengths of P2VP. The morphological transition was mainly attributed to the balance of the driven forces between the intermolecular π–π interactions among conjugated PPV blocks and the crystallization driven force based on TIPS groups during the SA process.

3.3 Materials and methods

3.3.1 Materials

Most of reagents and solutions were used as commercially received in synthesized procedures except dimethylformamide (DMF), potassium tert-butoxide (K*t*BuO), 1,1-diphenylethlene (DPE), 2-vinylpyridine (2VP), lithium chloride (LiCl), tetrahydrofuran (THF) and benzene. DMF was dried with molecular sieve before used. K*t*BuO and LiCl were heated at 120 °C under vacuum to remove water. DPE was titrated with n-BuLi until a red color sustained and then distilled under reduced pressure. 2VP was distilled with CaH_2 twice. THF and benzene was dried with Na and used as freshly distilled.

3.3.2 Methods

3.3.2.1 Characterization Equipment

^{1}H NMR spectra were measured on a Bruker AVANCE 400 MHz spectrometer with tetramethylsilane (TMS) as the internal standard. Molecular weights were determined by GPC measurements, which were carried out on a Waters ACQUITY APC System equipped with a UV detector (Waters ACQUITY TUV) and 3 series connected chromatographic columns (ACQUITY APC XT 450, 200, 45, 4.6 × 150 mm). Polystyrene standards (Aldrich) were used for calibration, and THF was used as the eluent with a flow rate of 0.5 ml min^{-1} at 40 °C.

3.3.2.2 Transmission electron microscopy

Transmission electron microscopy (TEM) photographs were taken by using a Hitachi HT7700 TEM instrument and operating at 100 kV. The samples were prepared by putting a drop of solution of assemblies on carbon-coated copper grids followed by solvent evaporated. For the

statistical analysis, the achieved photos were analyzed by using Digital Micrograph software package developed by the US Gatan company. The diagonal length was used to characterize the scale of the 2D rectangular micelles. The number-average length (L_n), the weight-average length (L_w), the number-average width (W_n), and the weight-average width (W_w) of the 1D or 2D micelles were calculated by the following equations: (where L_i and W_i are the sizes of individual 1D or 2D micelles, respectively, N_i are the number of L_i and W_i).

$$L_n = \frac{\sum_{i=1}^{N} N_i L_i}{\sum_{i=1}^{N} N_i} \qquad \text{(Equation 3.1)}$$

$$L_w = \frac{\sum_{i=1}^{N} N_i {L_i}^2}{\sum_{i=1}^{N} N_i L_i} \qquad \text{(Equation 3.2)}$$

$$W_n = \frac{\sum_{i=1}^{N} N_i W_i}{\sum_{i=1}^{N} N_i} \qquad \text{(Equation 3.3)}$$

$$W_w = \frac{\sum_{i=1}^{N} N_i {W_i}^2}{\sum_{i=1}^{N} N_i W_i} \qquad \text{(Equation 3.4)}$$

3.3.2.3 Atomic force microscopy

The detected AFM samples were prepared by drop-coating about 15 μL of the 2-D assemblies' solution onto a pre-cleaned and treated silicon wafer followed by evaporating the solvent isobutanol. The silicon wafers used as substrate were cleaned in piranha solution for 6 h, then ultrasound treated in ethanol, water, and ultrapure water in turn, and finally dried with blowing nitrogen. The images were gained using an Asylum Research AFM in AC mode under ambient conditions. The used sensor cantilevers were Silicon probe reflex coated with aluminum manufactured by Budget sensors Company. Images were analyzed with IGOR Pro software developed by WaveMetrics Inc.

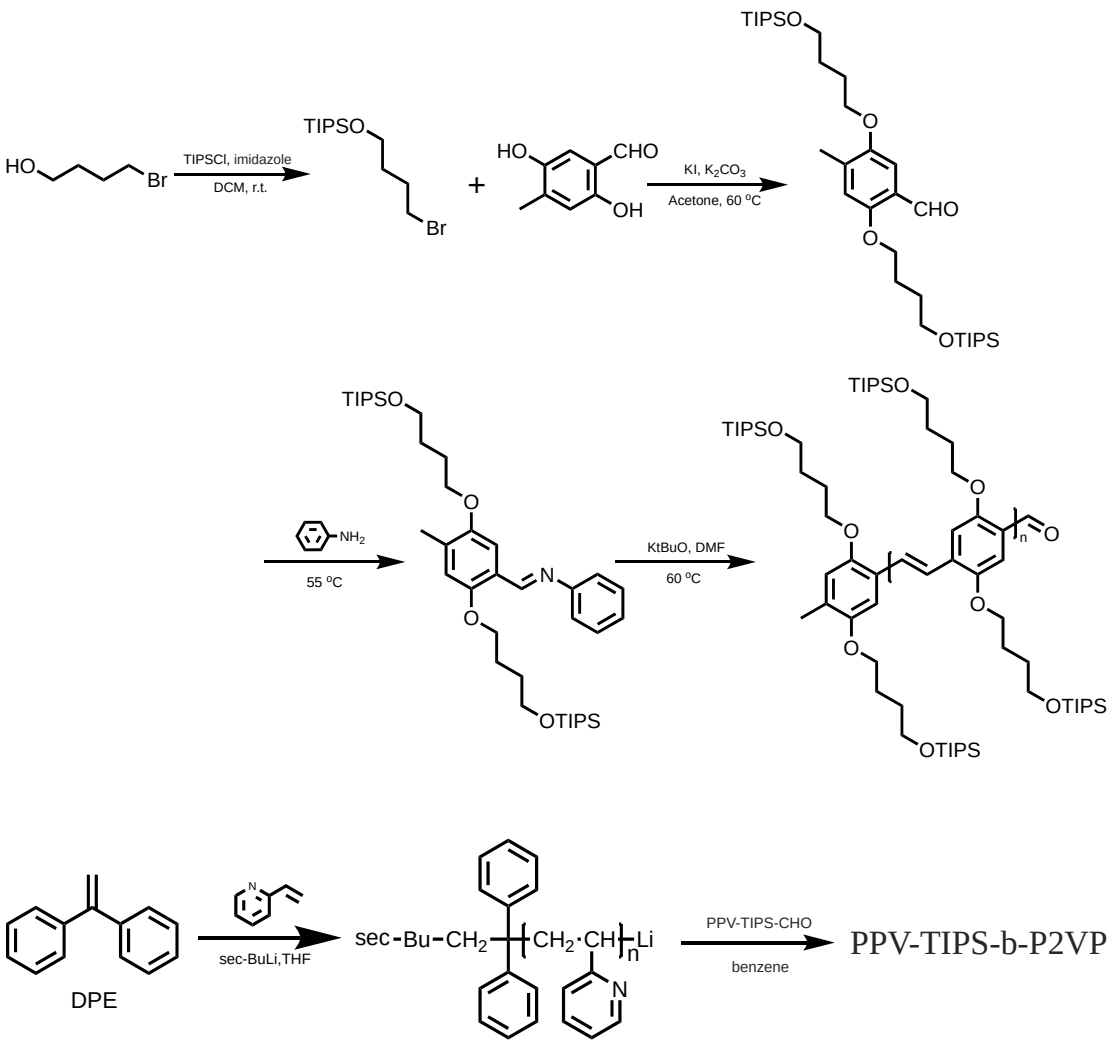

Scheme 3.1. Schematic synthesis route for PPV-TIPS-*b*-P2VP.

3.3.2.4 Synthesis of (4-bromobutoxy) triisopropylsilane (1)

A mixture of 4-bromo-1-butanol (14.2 g, 37 mmol), chlorotriisopropylsilane (4.82 g, 25 mmol) and imidazole (1g, 14.6 mmol) in DCM (50 mL) was refluxed at room temperature overnight under Ar atmosphere. The mixture was extracted with anhydrous EtOAc (3 × 40 ml), then the gathered organic phase was dried with $MgSO_4$, finally the solvent was removed by rotary evaporator. After

purification by chromatography (silica gel, petroleum ether), a yellow oil (**1**, 7.3 g, 0.023 mol, 94%) was obtained, which was determined by ^{1}H NMR (Appendix B, Figure B.1).

3.3.2.5 Synthesis of 4-methyl-2,5-bis(4-((triisopropylsilyl) oxy) butoxy) benzaldehyde (2)

(4-bromobutoxy) triisopropylsilane (5.5g, 17.8 mmol) was dissolved in acetone (60 ml), then added K_2CO_3 (4.14g, 30 mmol), KI (1.24g, 7.5 mmol), and 2,5-dihydroxy-4-methylbenzaldehyde (912 mg, 6 mmol). The reaction was refluxed overnight. After cooling to room temperature, 60 mL water was added into mixture. The mixture was extracted with anhydrous EtOAc (3 × 50 mL). After dried by $MgSO_4$ and rotary evaporating, the obtained crude oil was purified by chromatography (silica gel, petroleum ether/ EtOAc=50:1), a white oil (3, 1.3g, 2.13 mmol, 35.6%) was obtained, which was determined by ^{1}H NMR (Appendix B, Figure B.1).

3.3.2.6 Synthesis of Poly-4-(5-chloro-2-((2-ethylhexyl) oxy)-4-methylstyryl)-2,5-bis((2-ethylhexyl) oxy))-benzaldehyde (PPV-TIPS-CHO) (3)

A mixture of 4-methyl-2,5-bis(4-((triisopropylsilyl) oxy) butoxy) benzaldehyde (608 mg, 10 mmol) and aniline (6.16 g, 66.06 mmol) was stirred for 2h at 50 °C under reduced pressure, then the temperature of the mixture raised to 110 °C to remove excess aniline to yield red brown viscous oil. Next, the solution of oil in 15 ml anhydrous DMF was added into round flask containing potassium tert-butoxide (225 mg, 3 mmol) with 15 mL anhydrous DMF at 50 °C. After stirring for 2h at the same temperature, the mixture was poured into 100 mL 1M hydrochloric acid and stirred for 48 h. Then the reaction mixture was extracted with chloroform (3 × 10 ml), and the organic phase was successively washed by aqueous $NaHCO_3$ and water followed by dried with $MgSO_4$ and rotary evaporating. Product in low dispersity was successively collected and fractionated by methanol, acetone and hexane with Soxhlet extraction. The value of M_n = 2540 and the

polydispersity index was measured at 1.07 by GPC in THF. The number-average degree of polymerization n = 5 for PPV-TIPS-CHO was determined by GPC and ^{1}H NMR (Appendix B, Figure B.3 and 4).

3.3.2.7 Synthesis of Poly(2,5-di(2'-ethylhexyloxy)-1,4-phenylenevinylene)-block-poly (2-vinylpyridine) (4, PPV-TIPS-*b*-P2VP)

In a glovebox filled with N_2 at -78 °C, 86.9 μL of sec-BuLi (1.3 M in hexane) was quickly added to a stirring solution of dried LiCl (45.7 mg, 1.13 mmol) and 1,1-diphenylethylene (DPE, 20 μl, 0.113 mmol) in THF (2 ml). Then maintaining -78 °C, a certain amount of 2-vinylpyridine (2VP) in THF (2 mL) was added to the mixture. After the reaction went on running for 2h at -78 °C, a solution of PPV-TIPS-CHO (40 mg, 0.01mmol) in benzene (2 ml) was quickly added into the reaction mixture to quench the anion polymerization. Then the reaction temperature was increased to room temperature and stirred for additional 12 h. As the reaction stopped, the reaction mixture was poured into 25 ml chloroform and washed successively with aqueous HCl (pH = 3), water and aqueous $NaHCO_3$. After rotary evaporating, the crude residue was purified by chromatography (silica gel, eluent was changed from chloroform to chloroform/Et_3N 9:1), and finally red solid was obtained. The block ratio of produced PPV_5-TIPS-*b*-$P2VP_n$ was determined by NMR and GPC. (Appendix B, Figure B.5-8)

3.4 Results and discussion

3.4.1 Design and preparation of PPV-TIPS BCP micelles

Due to the introduction of silicon, the bulkier TIPS groups at side chains can change the intermolecular π–π packing, the solubility, and the crystallinity, compared with alkyl chains used in the previous report. [6, 20] Inspired by this principle, we designed a new PPV-based copolymer containing TIPS side chain with a corona block of P2VP as building blocks (Scheme 3.2). PPV-

TIPS aldehyde polymer was synthesized through Siegrist polycondensation and the monomer number of PPV block was 5 calculated by nuclear magnetic resonance (NMR) and gel permeation chromatography (GPC), with the polydispersity as 1.07 (Figure B.3 and 4). Finally, a series of BCPs were prepared by quenching the anionic polymerization of P2VP using PPV-TIPS aldehyde. The BCPs with different lengths of P2VP were synthesized, and the $R_{PPV/P2VP}$, short for the block ratio of PPV and P2VP, were nearly 1:2, 1:3, and 1:4 (Figure B.5-S8). To explore the effect of TIPS groups at the side chains on the self-assembly process and final morphology, the self-assembly experiments of PPV_5-TIPS-*b*-$P2VP_n$ in isopropanol solutions were carried out at a series of concentrations, which is a selective solvent for P2VP corona. These solutions were heated at 80 °C for 1 h and slowly cooled to room temperature (25 °C) followed by aging for 3 days. As expected, uniform regular 2D micelles were achieved, which were observed under transmission electron microscopy (TEM) and atomic force microscopy (AFM).

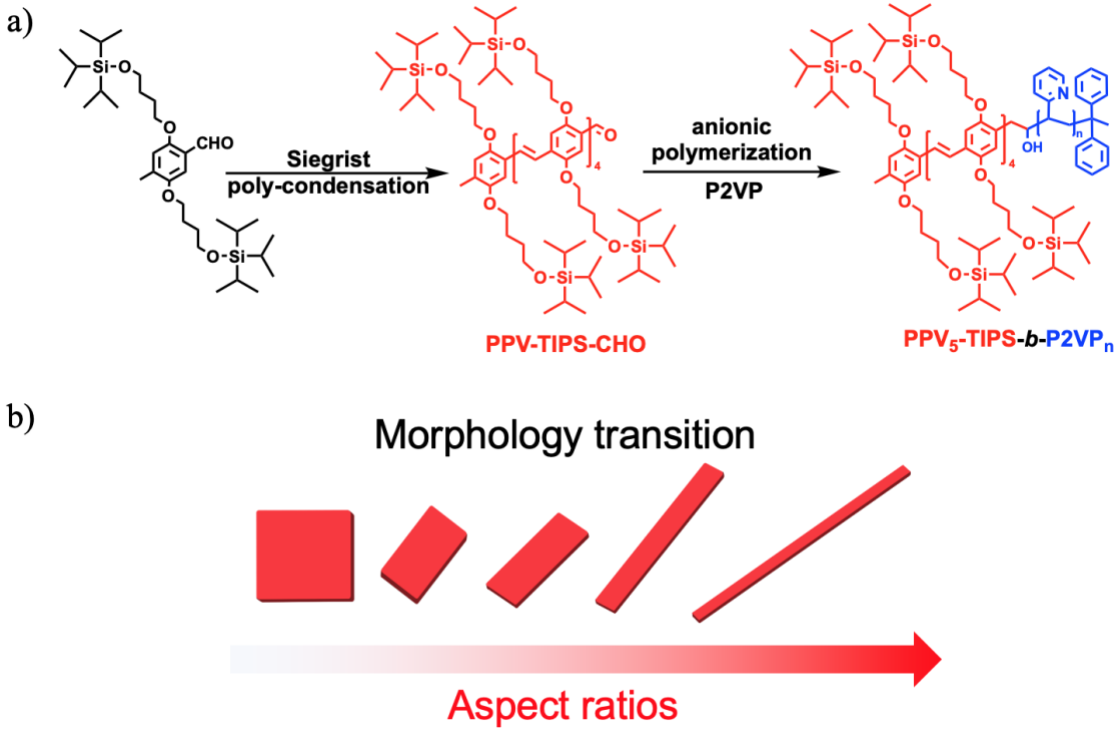

Scheme 3.2. (a) Synthesis route for PPV_5-TIPS-*b*-$P2VP_n$. (b) The morphology transition process from 2D platelet micelles into rod-like micelles by precisely controlling aspect ratios.

3.4.2 Effect of the P2VP chain length on the morphology transition

It was observed that the sizes and morphologies of the assembled 2D micelles were influenced by the length of $P2VP_n$ (n = 10, 15, 20). In the 0.005 mg·mL^{-1} solutions, all BCPs were assembled into regular 2D platelet micelles but the shapes of achieved micelles were quite different. In the case of PPV_5-TIPS-*b*-$P2VP_{10}$, it was observed that the assembled architectures were uniform square micelles. (Figure. 3.1a, b). The number-average length (L_n) of the square micelles at 0.005 mg mL^{-1} was calculated to be 661nm, and the weight-average length (L_w) was 707 nm. The morphology of these 2D micelles was strongly dependent on the length of the P2VP chain. As the degree of polymerization of P2VP increased, the morphology of micelles became rectangular platelet with higher aspect ratios.

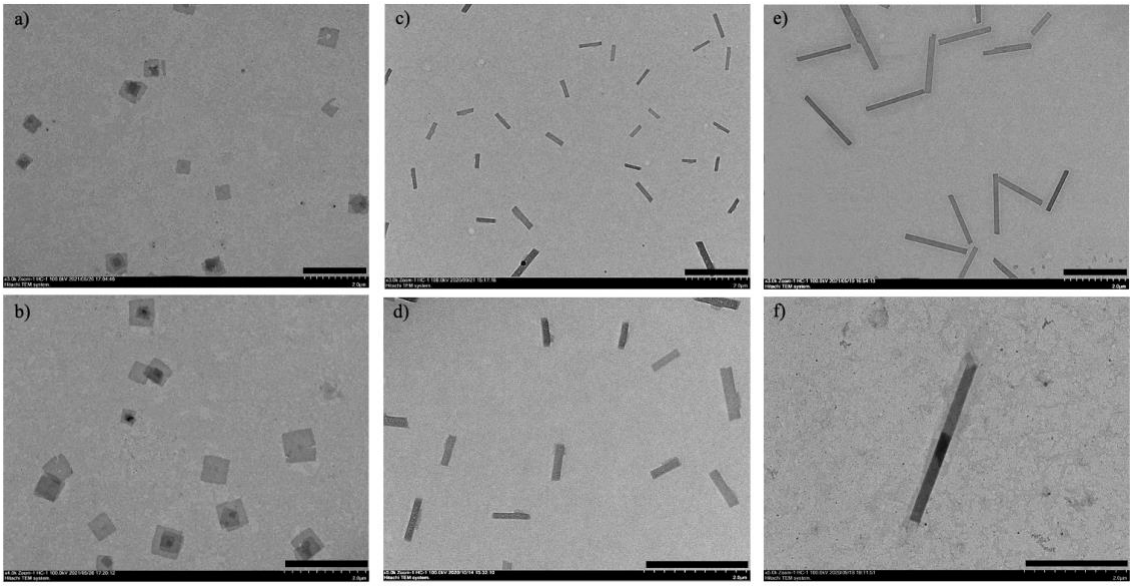

Figure 3.1 TEM images of 2D micelles prepared from (a, b) 0.005 mg ml^{-1} isopropanol solution of PPV_5-TIPS-*b*-$P2VP_{10}$; (c, d) 0.005 mg ml^{-1} isopropanol solution of PPV_5-TIPS-*b*-$P2VP_{15}$; (e,

f) 0.005 mg ml^{-1} isopropanol solution of PPV_5-TIPS-*b*-$P2VP_{20}$. Scale bars in TEM photos are 2 μm.

The L_n of the 2D rectangular platelet micelles was 656 nm, while the W_n was 165 nm, and the aspect ratio of that was 3.96 (Figure 3.1c, d). When the $R_{PPV/P2VP}$ was changed to 1: 4, the scales of the formed rectangular micelles were larger with a higher aspect ratio of 9.26 (Figure 3.1e, f). The W_n grew to 198 nm (W_w = 208 nm) and L_n tended to be 1834 nm (L_w = 1847 nm). (Figure B.9) It was obvious that the aspect ratios of these platelet micelles gradually increased as the length of P2VP increased, resulting in morphology transition from square to rectangular micelles (Table 3.1). The dispersity of the length (L_w/L_n) and the width (W_w/W_n) of these 2D micelles were less than 1.1, implying that all kinds of 2D micelles were uniform.

Table 3.1. Summary Data of the various Micelles

Polymers	Concentrations（mg ml^{-1}）	L_n (nm)	L_w/ L_n (nm)	W_n (nm)	W_w/ W_n (nm)	Aspect ratios
PPV_5-TIPS-*b*-$P2VP_{10}$	0.005	661	1.07	661	1.07	1
PPV_5-TIPS-*b*-$P2VP_{10}$	0.01	1738	1.02	191	1.02	9.10
PPV_5-TIPS-*b*-$P2VP_{15}$	0.005	656	1.03	165	1.02	3.96
PPV_5-TIPS-*b*-$P2VP_{15}$	0.01	2278	1.02	225	1.14	10.12
PPV_5-TIPS-*b*-$P2VP_{20}$	0.001	1230	1.03	258	1.01	4.77
PPV_5-TIPS-*b*-$P2VP_{20}$	0.005	1834	1.01	198	1.05	9.26
PPV_5-TIPS-*b*-$P2VP_{20}$	0.01	3421	1.06	158	1.09	21.65

3.4.3 Tuning the morphology of the 2D micelles by varying solution concentrations

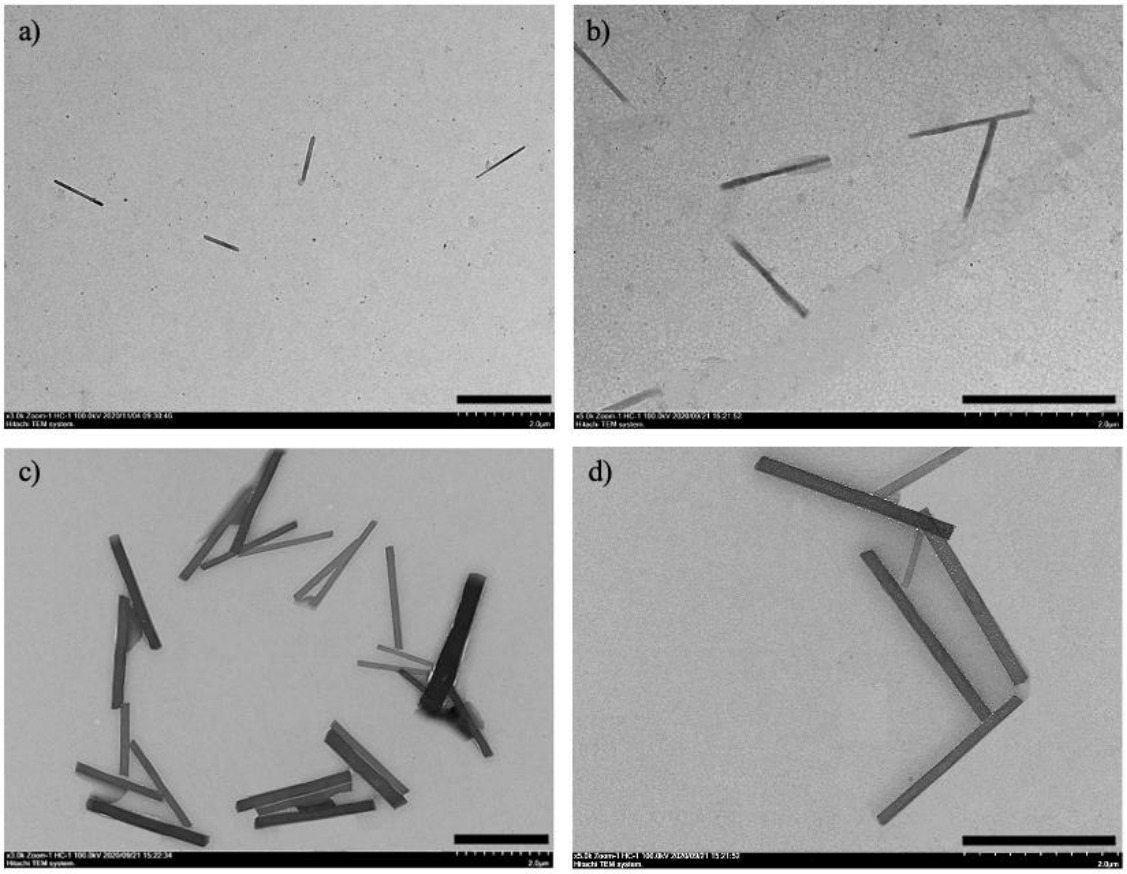

Figure 3.2 TEM images of 2D rectangular micelles prepared from (a, b) 0.01 mg ml^{-1} isopropanol solution of PPV_5-TIPS-*b*-$P2VP_{10}$; (c, d) 0.01 mg ml^{-1} isopropanol solution of PPV_5-TIPS-*b*-$P2VP_{15}$. Scale bars in TEM photos are 2 μm.

To further adjust the aspect ratios of the obtained micelles, we investigated the concentration effect on the self-assembly of PPV_5-TIPS-*b*-$P2VP_n$. The self-assembly behavior of PPV_5-TIPS-*b*-$P2VP_{10}$ in isopropanol at 0.01 mg·mL^{-1} was forming rectangular micelles (Figure 3.2a, b), which is different from the original square morphology at 0.005 mg·mL^{-1} (Figure 3.1a). The L_n of the

rectangular micelles as 1738 nm was remarkably higher than square micelles, while the W_n and the aspect ratios were 246 nm and 7.06, respectively.

When the concentration of the PPV_5-TIPS-b-$P2VP_{15}$ solution was increased to 0.01 mg ml^{-1}, the L_n of the rectangular micelles grew up to 2278 nm (L_w = 2327 nm). The W_n of the 2D micelles increased to 225 nm (W_w = 257 nm), the aspect ratios continued to increase to 10.12 as the concentrations increased. The influence of the concentrations (0.001 mg·ml^{-1}, 0.005 mg·ml^{-1}, and 0.01 mg·ml^{-1}) on the sizes of 2D rectangular micelles was also confirmed by assembled architectures of PPV_5-TIPS-b-$P2VP_{20}$ (Figure 3.1e, f and 3.3). The tendency of decreased aspect ratio as decreased concentration was consistent with that of all BCPs. The L_n of the 2D rectangular micelles in a 0.001 mg·ml^{-1} solution decreased to 1230 nm with higher W_n as 258 nm (aspect ratio = 4.77). Notably, continuing to increase the concentrations to adjust the aspect ratios of original rectangular micelles at 0.005 mg·mL^{-1} (Figure 3.1e, f), rod-like micelles with quite high aspect ratios were achieved at the 0.01 mg·mL^{-1} (Figure 3.3c, d). The L_n of these rod-like micelles was 3421nm (L_w = 3633 nm) with good dispersity (L_w/L_n =1.06).

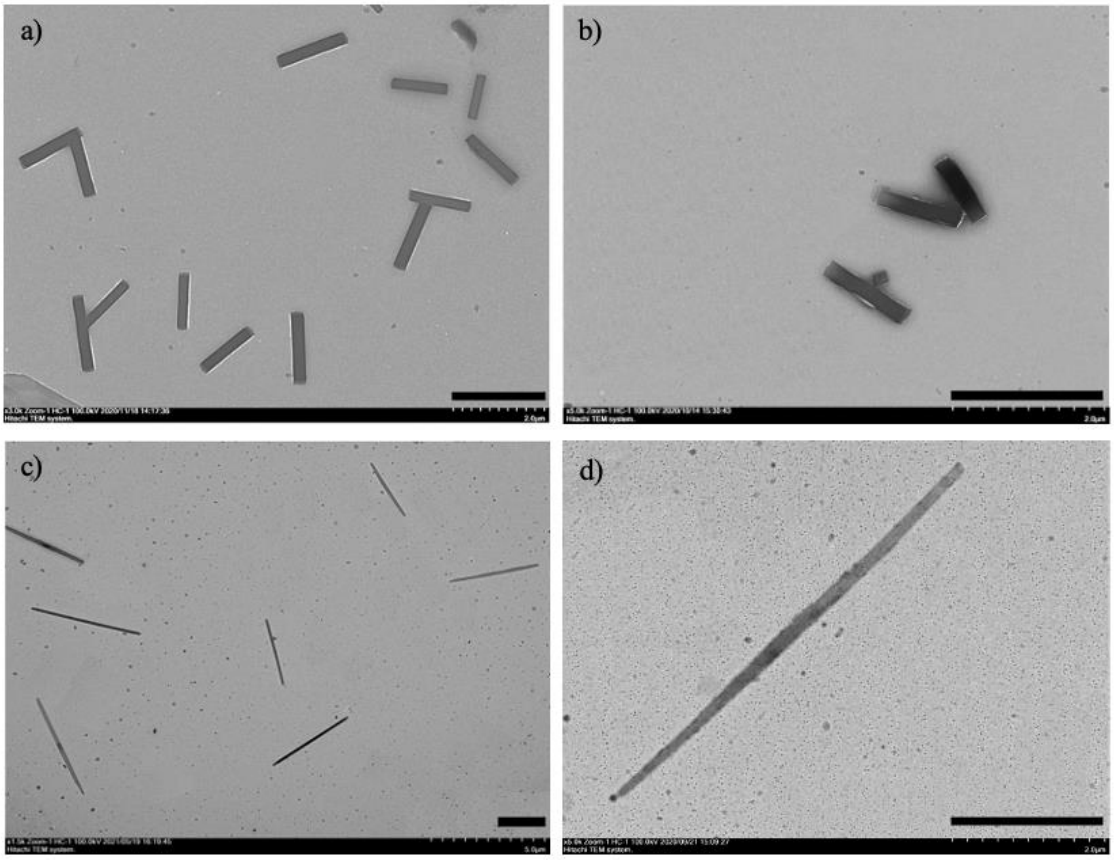

Figure 3.3 TEM images of 2D rectangular and rod-like micelles prepared from PPV_5-TIPS-*b*-$P2VP_{20}$ at different concentrations in isopropanol of (a, b) 0.001 mg ml^{-1} and (c, d) 0.01 mg ml^{-1}. Scale bars in TEM photos are 2 μm.

Atomic force microscopy (AFM) characterization showed similar results with the TEM observation concerning the scales of the micelles formed from different block ratios of BCPs. (Figure 3.4). In addition, it was clear that the thickness of these micelles in different shapes formed from PPV-TIPS based BCPs changed very little. Their height of 43-47 nm indicated that the BCPs should adopt multilayer packing in the molecular arrangement, compared with the previously reported EH-PPV monolayer square structures, [6] with the introduction of the crystallization of the TIPS groups in the SA process.

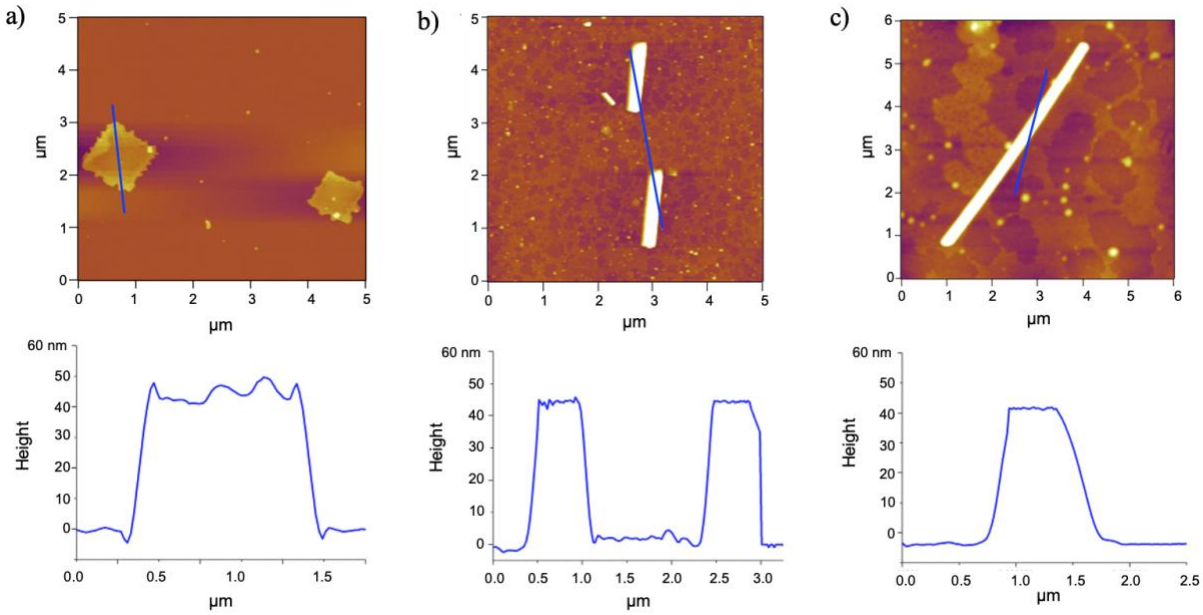

Figure 3.4 AFM height images of 2D square and rectangular micelles formed from PPV-TIPS-*b*-P2VP with different block ratios in isobutanol. (a) PPV_5-TIPS-b-$P2VP_{10}$ at 0.005 mg ml^{-1}; (b) PPV_5-TIPS-b-$P2VP_{15}$ at 0.005 mg ml^{-1}; and (c) PPV_5-TIPS-b-$P2VP_{20}$ at 0.005 mg ml^{-1}.

3.4.4 Growth process and mechanism of the formation of the 2D platelet micelles

To explore the assembly process of the BCPs in isopropanol, we traced the growth process of 2D rectangular micelles formed from PPV_5-TIPS-*b*-$P2VP_{10}$ in a 0.01 mg·ml^{-1} solution as times change. After the heating-cooling process followed aging for 24h, some 1D fiber-like structures were observed and then these micelles showed side-by-side attachment to each other in Figure B.10a, b. [11] As these fiber micelles continued to parallelly stack when aging at 48h, the clear outline of 2D morphology gradually appeared (Figure B.10c, d). Finally, these aggregates grew to the uniform 2D rectangular architectures at 72h (Figure 4.2b). To understand more growth details in SA process, we measured the variable-temperature UV−vis absorption spectra with different ratios of BCPs (Figure B.11). In the growth process of 2D rectangular micelles formed in

isopropanol solution at a concentration of 0.005 mg mL^{-1}, the UV−vis spectrum of PPV_5-TIPS-*b*-$P2VP_{15}$ at 80 °C has a peak at 447 nm, where the BCP was completely dissolved without aggregation. As the temperatures decreased, there was a redshift of 12 nm of the absorption maximum from 80 °C to room temperature, consistent with the formation of 1D fiber-like intermediate micelles (Figure B.10). After the cooling process, there was little change displayed on the absorption maximum during the aging time from 24 to 72 h with only 5 nm of blueshift, which was in accordance with the parallel stacking and attachment of the 1D fiber micelles shown in Figure S10. Similar variation tendency of the absorption peaks was observed in the SA processes of all the BCPs in the isopropanol. In addition, differential scanning calorimetry (DSC) measurement was performed to characterize the change of the molecular states (Figure B.12). PPV-TIPS-CHO showed T_g (glass transition temperature) at 41 ℃ and T_c (crystalline transition temperature) at 63 ℃, respectively. T_g and T_c are lower than the temperature of initial self-assembly (90 °C), which represents that the polymer undergoes two phase transition processes by the crystallization of the silicon groups and the change of the aggregation states of the polymer chains. It indicated that the π−π stacking interactions of PPV core and the crystallization force between Si-Si on the TIPS side chain led to the molecular packing and the movement of polymer chains during the SA process. The balance of these driven forces caused the difference of growth rates in different orientations, which resulted in the morphology transition from square to rectangular micelles.

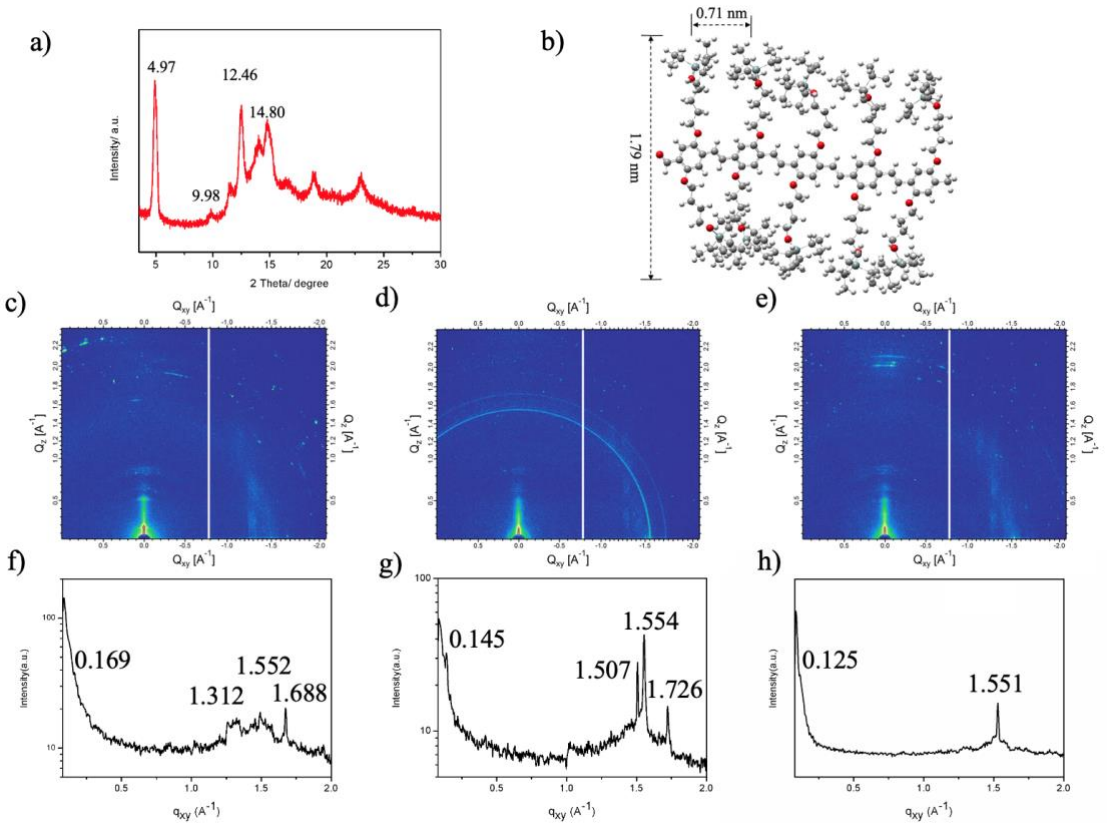

Figure 3.5 (a) XRD patterns of PPV_5-TIPS-CHO; (b) The optimized structures and calculated scales of PPV_5-TIPS-CHO by DFT calculations. The DFT calculation was performed with the Gaussian09 suite of programs. (c-e) 2D GIWAXS patterns and GIWAXS profiles along the (f-h) in-plane direction of platelet 2-D square or rectangular micelles obtained from PPV_5-TIPS-*b*-$P2VP_{10}$, PPV_5-TIPS-*b*-$P2VP_{15}$, and PPV_5-TIPS-*b*-$P2VP_{20}$.

To test the effect of the introduction of the TIPS group at side chains on the crystallinity of polymers, we carried out powder XRD measurements of PPV-TIPS-CHO and PPV-EH-CHO[6]. In the case of PPV-EH-CHO (Figure 4a), most peaks were broad peaks and only the (100) and (200) discernible diffraction peaks at 2θ values of 9.29° and 18.64° could be significantly observed. This result indicated that the PPV-EH-CHO molecules should adopt lamellar arrangement with packing distance d_{001} = 0.96 nm. Compared with the XRD data of EH-PPV-CHO, PPV-TIPS

homopolymers presented sharper diffraction peaks and narrower half peak width, which means that the crystallinity of the BCPs was obviously improved with the lamellar arrangement characteristic by the introduction of TIPS groups. The XRD data showed obvious Bragg reflections (001), (002), (003) peaks at (4.97°, 9.98°, and 14.80°) along the packing direction, respectively. The packing distance calculated as d_{001}= 1.79 nm was bigger than the EH-PPV-CHO, showing the effect of the spatial hindrance of TIPS groups on PPV accumulation. In addition, the (010), (020) reflection peak at 12.46° and 22.99° suggest that the PPV-TIPS also stack in order along another direction with packing distance d_{010}= 0.71 nm.

Furthermore, the structure of the conjugated PPV_5-TIPS-CHO block was optimized by density functional theory (DFT) calculations with the Gaussian09 suite (Figure 3.5b). [21-23] The PPV block exhibited a rigid skeleton and its unit length was calculated as 1.79 nm, which could be attributed to the (001) reflection. The width between the silicon of monomers was estimated to be 0.71 nm, which could be attributed to the (010) direction. These results are consistent with the XDR diffraction peaks. To investigate the molecular packing in these micelles with different shapes, grazing incidence wide-angle X-ray scattering (GIWAXS) was performed (Figure 3.5c–h). These micelles formed by PPV_5-TIPS-*b*-$P2VP_{10}$, PPV_5-TIPS-*b*-$P2VP_{15}$, and PPV_5-TIPS-*b*-$P2VP_{20}$ exhibited similar diffraction patterns. There was only one periodic reflection peak along q_z direction observed (Figure B.14), the packing distance was calculated as 3.81 nm, which was equal to two layers of polymer molecules. This suggested that all BCP molecules favor an edge-on configuration in the achieved micelles. Along q_{xy} direction, these BCPs revealed two similar reflection peaks along q_{xy}. One of the d-spacing as 4.04 Å, was calculated from the (100) peak (q = 1.55 $Å^{-1}$), which should be the π–π stacking distance of the primary molecular arrangement based on PPV-TIPS backbones (Figure 3.6a). The other d-spacing as 37.1, 43.3, and 49.9 Å were

calculated from the (010) peaks (q= 0.169, 0.145, and 0.125 $Å^{-1}$, respectively), which should be assigned as the distance between adjacent polymer center of PPV backbones along (010) direction, and the difference of d-spacing should be caused by the length of P2VP.

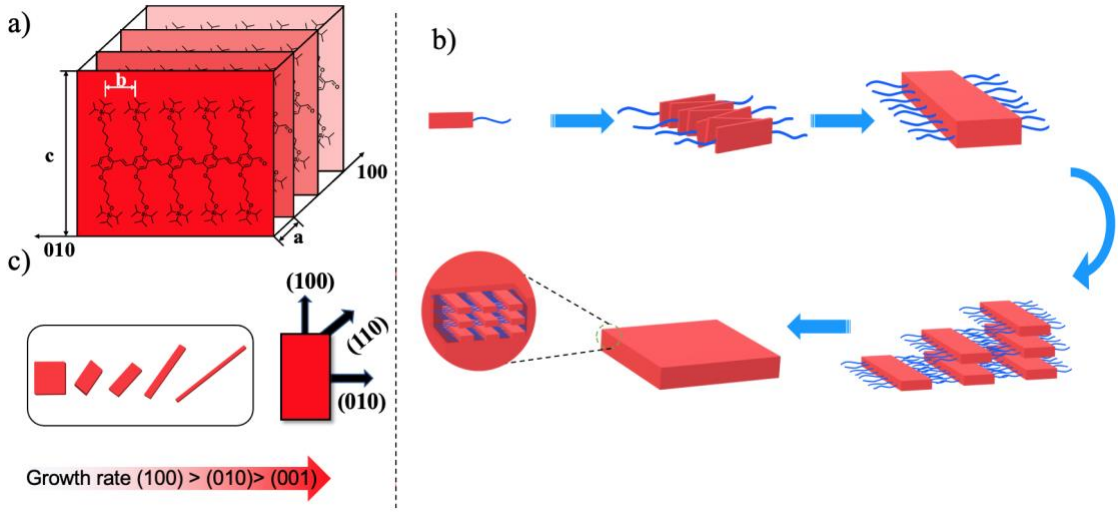

Figure 3.6 (a) Probable structure of the one-dimensional fiber-like PPV monolayer packing model; (b) Proposed growth process of 2D micelles by self-assembly process involving PPV-TIPS-*b*-P2VP; (c) Morphological transition by different growth rates.

From the above results from measurements of TEM, AFM, DFT, GIWAXS, DSC, XRD, and UV-Vis absorption spectra, the schematic representation of the whole SA process was depicted in Figure 3.6b. As temperature decreased, the BCPs in the completely dissolved state started to rapidly aggregate on account of the decrease in the solubility of PPV-TIPS block. Firstly, the BCP molecules arranged in order via crystallization between TIPS groups under 60 °C. And after the temperature was below 40 °C, PPV-TIPS-*b*-P2VP formed regular one-dimensional fiber-like micelles with monolayer PPV backbones closely packing as (100) orientation driven by not only crystallization but also the intermolecular π–π interactions. The distances between the neighbor

PPV blocks are equal to 4.04 Å, confirmed by GIWAXS. Then, during the aging process, these fibers started to attach to each other in the side-by-side way, defined as (010) orientation, gradually grew, and finally organized into uniform 2D rectangular micelles. When the P2VP block was short, the poor solubility made the whole BCP molecule aggregate quite fast, and the π–π stacking force of PPV core based on solvophobic interaction became the leading driven force to form the initial 2D square micelles based on PPV_5-TIPS-*b*-$P2VP_{10}$, which is consistent with previous reports.[6] As the block ratios of P2VP in polymers increased, the solubility of BCPs increased and the crystalline force between Si-Si of TIPS side chains gradually became the leading driven force during the SA process. Conjugated molecule structures made the dominant growth orientation of assemblies consistent with the direction of intermolecular π-π interaction. Due to the increasing lengths of P2VP in BCPs, growth rate in (010) direction was restrained. Based on the above result, the growth rate of each plane is (100) > (010) > (001). Thus, one side (100) of the 2D nanosheet would grow faster than the other side (010), leading to the morphological transition from a square to an anisotropic rectangular nanosheet with a higher aspect ratio. When the length of P2VP is longer, we could even achieve the formation of rod-like micelles with the highest aspect ratios because of the leading crystalline force based on silicon. In summary, the self-assembly of PPV_5-TIPS-*b*-$P2VP_n$ could be considered as a process in which the two driven forces competed. Compared with each other, the crystallization of the TIPS groups should be stronger and more thermodynamically stable, while the π–π interactions between the PPV block should be weaker and more relevant to dynamics. The balance of the driven forces resulted in the morphological transition between different shapes.

3.4.5 Heterogenous co-assembly based on crystallization and π–π interactions

To further explore the effect of the collaboration between crystallization and π–π stacking interactions on the assembly process, we tried to co-assembly by using PPV_{12}-*b*-$P2VP_{12}$ [6] and PPV_5-TIPS-*b*-$P2VP_{10}$ (1:1) at a 0.005 mg·mL^{-1} solution, whose lengths of P2VP were similar. As reported,[6] the main driven force of BCPs based on PPV-EH was π–π stacking interaction and growth rate in all directions was uniform. Based on above results, we established the heterogenous co-assembly method by the introduction of the PPV_5-TIPS-*b*-$P2VP_{10}$ with crystalline into PPV_{12}-*b*-$P2VP_{12}$ by controlling the balance between crystallization and π–π interactions. These two BCPs were separately assembled into uniform 2D square micelles under the same condition (Figure 3.1a, B.15c and d). For the co-assembly system, the mixed solution was heated at 80 °C for 1 h and slowly cooled to room temperature (25 °C) followed by aging for 1 day. Surprisingly, the original morphology as square micelles disappeared and the new circular disk-like micelles were achieved (Figure 3.7). The edges of these circular structures were smooth rather than the original right-angle structure as square micelles and these micelles were easily packed. Analysis of these circular micelles, determined by measuring more than 50 samples in several images, showed that the number-average diameter (D_n) of circular structures 982 nm with low dispersity（D_w/D_n = 1.09) was uniform. The D_n and D_w are the number and weight average micelle diameters, respectively. The main driven force of PPV-EH BCPs was π–π stacking interaction, as reported, and that of BCPs based on PPV-TIPS were the combined forces between Si-Si crystallization and π–π stacking interaction. The introduction of PPV-TIPS BCPs with crystalline into co-assembly system leaded to difference of growth rate in partial directions, resulting in the morphological transformation from square to circular micelles. Therefore, the achievement of heterogenous co-assembly could be explained by the collaboration between π–π stacking interaction and crystalline driven force in good balance.

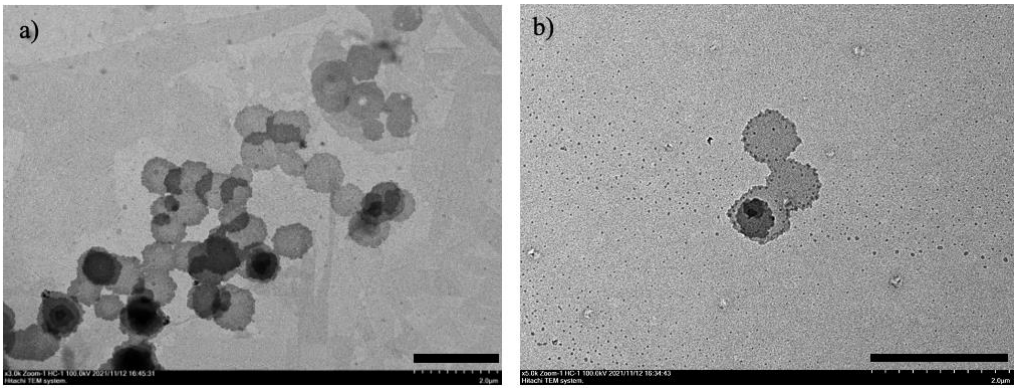

Figure 3.7 TEM images of 2D circular disk-like micelles based on co-assembly with PPV_{12}-*b*-$P2VP_{12}$ and PPV_5-TIPS-*b*-$P2VP_{10}$ at a 0.005 mg·mL^{-1} solution. Scale bars in TEM photos are 2 μm.

Next, we tried to perform an analogous experiment by using different lengths of BCPs (PPV_{12}-*b*-$P2VP_{12}$ and PPV_5-TIPS-*b*-$P2VP_{20}$). TEM results revealed that the obtained architectures were irregular platelet structures and the edges of the micelles were not smooth (Figure B.15a, b). The reason why these micelles were not uniform in this case could be that large differences in aggregation rates based on different lengths of P2VP broke the original good balance between π−π stacking interaction and crystallization. In all, the ability to perform 2D heterogenous co-assembly based on the balance of different driven forces would represent a significant advance in tailoring platelets as it would allow the creation of novel architectures by using BCPs with different cores.

3.5 Conclusions

In summary, we demonstrated the self-assembly of a series of conjugated BCPs into various 2D square and rectangular nanosheets by the introduction of TIPS group. We tuned the scales and shapes of 2D platelet micelles by regulating the ratios of PPV and P2VP. Besides, by adjusting the concentrations of micelles, the morphology transition from 2D rectangular to rod-like micelles could also be achieved based on the balance of the strong π–π interaction and crystalline force between Si-Si. Based on the result, the heterogenous co-assembly method was established by the introduction of PPV-TIPS BCPs with crystalline into co-assembly system, resulting in new circular disk-like micelles. These nanosheets with controllable shapes and scales could be potential materials for biological and optoelectronics applications.

3.6 References

[1] Zhuang X.; Mai Y.; Wu D.; Zhang F.; Feng X., Two-Dimensional Soft Nanomaterials: A Fascinating World of Materials. Adv. Mater. 2015**,** 27 (3), 403-427.

[2] Wakahara T.; D'Angelo P.; Miyazawa K. i.; Nemoto Y.; Ito O.; Tanigaki N.; Bradley D. D. C.; Anthopoulos T. D., Fullerene/Cobalt Porphyrin Hybrid Nanosheets with Ambipolar Charge Transporting Characteristics. J. Am. Chem. Soc. 2012**,** 134 (17), 7204-7206.

[3] Chao Z. C.; Lu H. W.; Xiao F.; Shao C.; Wei Z. X.; Yu J. T.; Zhang X. D.; Lin L.; Tian L. L., Robust and Tumor-Environment-Activated DNA Cross-Linker Driving Nanoparticle Accumulation for Enhanced Therapeutics. CCS Chemistry 2020, 2 (5), 349-361.

[4] Bai W.; Jiang Z.; Ribbe A. E.; Thayumanavan S., Smart Organic Two-Dimensional Materials Based on a Rational Combination of Non-covalent Interactions. Angew. Chem. Int. Ed. 2016**,** 55 (36), 10707-10711.

[5] Insua I.; Montenegro J., 1D to 2D Self Assembly of Cyclic Peptides. J. Am. Chem. Soc. 2020,

142 (1), 300-307.

[6] Han L.; Wang M.; Jia X.; Chen W.; Qian H.; He F., Uniform two-dimensional square assemblies from conjugated block copolymers driven by π–π interactions with controllable sizes. Nat. Commun. 2018**,** 9 (1), 865.

[7] Qi R.; Zhu Y.; Han L.; Wang M.; He F., Rectangular Platelet Micelles with Controlled Aspect Ratio by Hierarchical Self-Assembly of Poly(3-hexylthiophene)-b-poly(ethylene glycol). Macromolecules 2020, 53 (15), 6555-6565.

[8] Feng C.; Jose Gonzalez-Alvarez M.; Song Y.; Li I.; Zhao G.; Molev G.; Guerin G.; Walker G.; Scholes G. D.; Manners I.; Winnik M. A., Synthesis, self-assembly and photophysical properties of oligo(2,5-dihexyloxy-1,4-phenylene vinylene)-block-poly(ethylene glycol). Soft Matter 2014, 10 (44), 8875-8887.

[9] Ganda S.; Dulle M.; Drechsler M.; Förster B.; Förster S.; Stenzel M. H., Two-Dimensional Self-Assembled Structures of Highly Ordered Bioactive Crystalline-Based Block Copolymers. Macromolecules 2017, 50 (21), 8544-8553.

[10] He X.; He Y.; Hsiao M. S.; Harniman R. L.; Pearce S.; Winnik M. A.; Manners I., Complex and Hierarchical 2D Assemblies via Crystallization-Driven Self-Assembly of Poly(l-lactide) Homopolymers with Charged Termini. J. Am. Chem. Soc. 2017, 139 (27), 9221-9228.

[11] Li H.; Han L.; Zhu Y.; Fernández-Trillo P.; He F., Transformation from Rod-Like to Diamond-Like Micelles by Thermally Induced Nucleation Self-Assembly. Macromolecules 2021, 54, 11, 5278–5285

[12] Lee I. H.; Amaladass P.; Yoon K. Y.; Shin S.; Kim, Y. J.; Kim I.; Lee E.; Choi, T. L., Nanostar and Nanonetwork Crystals Fabricated by in Situ Nanoparticlization of Fully Conjugated Polythiophene Diblock Copolymers. J. Am. Chem. Soc. 2013, 135 (47), 17695-17698.

[13] Pearce S.; He X.; Hsiao M. S.; Harniman R. L.; MacFarlane L. R.; Manners I., Uniform, High-Aspect-Ratio, and Patchy 2D Platelets by Living Crystallization-Driven Self-Assembly of Crystallizable Poly(ferrocenyldimethylsilane)-Based Homopolymers with Hydrophilic Charged Termini. Macromolecules 2019, 52 (16), 6068-6079.

[14] Nazemi A.; He X.; MacFarlane L. R.; Harniman R. L.; Hsiao, M. S.; Winnik M. A.; Faul C. F. J.; Manners I., Uniform "Patchy" Platelets by Seeded Heteroepitaxial Growth of Crystallizable Polymer Blends in Two Dimensions. J. Am. Chem. Soc. 2017, 139 (12), 4409-4417.

[15] Osichow A.; Rabe C.; Vogtt K.; Narayanan T.; Harnau L.; Drechsler M.; Ballauff M.; Mecking S., Ideal Polyethylene Nanocrystals. J. Am. Chem. Soc. 2013, 135 (31), 11645-11650.

[16] Inam M.; Jones J. R.; Pérez-Madrigal M. M.; Arno M. C.; Dove A. P.; O'Reilly R. K., Controlling the Size of Two-Dimensional Polymer Platelets for Water-in-Water Emulsifiers. ACS Cent. Sci. 2018, 4 (1), 63-70.

[17] Günes S.; Neugebauer H.; Sariciftci N. S., Conjugated Polymer-Based Organic Solar Cells. Chem. Rev. 2007, 107 (4), 1324-1338.

[18] Elacqua E.; Croom A.; Manning K. B.; Pomarico S. K.; Lye D.; Young L.; Weck M., Supramolecular Diblock Copolymers Featuring Well-defined Telechelic Building Blocks. Angew. Chem. Int. Ed. 2016, 55 (51), 15873-15878.

[19] Han L.; Fan H.; Zhu Y. L.; Wang M. J.; Pan F.; Yu D. P.; Zhao Y.; He F., Precisely Controlled Two-Dimensional Rhombic Copolymer Micelles for Sensitive Flexible Tunneling Devices. CCS Chem. 2020**,** 3 (5), 1399-1409.

[20] Yang S.; Kang S. Y.; Choi, T. L., Morphologically Tunable Square and Rectangular Nanosheets of a Simple Conjugated Homopolymer by Changing Solvents. J. Am. Chem. Soc. 2019, 141 (48), 19138-19143.

[21] Frisch M. J. et al. Gaussian 09, Revision D.01 (Gaussian, Inc., Wallingford, CT, 2009).

[22] Becke A. D., Density-functional thermochemistry. III. The role of exact exchange. J. Chem. Phys. 1993, 98, 5648–5652.

[23] Lee C.; Yang W.; Parr R. G., Development of the Colle-Salvetti correlation- energy formula into a functional of the electron density. Phys. Rev. B 1988, 37, 785–789.

CHAPTER 4 HIERARCHICAL CHIRAL SUPRAMOLECULAR NANOARCHITECTONICS WITH MOLECULAR DETECTION: HELICAL STRUCTURE CONTROLS UPON SELF-ASSEMBLY AND CO-ASSEMBLY

Published Article

Heng Li,[ab] Liang Han,[a] Qing Li,[e] Hanjian Lai,[a] Paco Fernández-Trillo,[bc] Leilei Tian[e] and Feng He[ad]

Macromolecular Rapid Communication, **2021**, 2100690.

DOI: doi.org/10.1002/marc.202100690

a. Shenzhen Grubbs Institute and Department of Chemistry, Southern University of Science and Technology, Shenzhen, 518055 (China).
b. School of Chemistry, University of Birmingham, B15 2TT, UK.
c. Departamento de Química, Facultade de Ciencias and Centro de Investigacións Científicas Avanzadas (CICA), Universidade da Coruña A Coruña, 15071 (Spain).
d. Guangdong Provincial Key Laboratory of Catalysis, Southern University of Science and Technology, Shenzhen, 518055 (China)
e. Department of Materials Science and Engineering, Southern University of Science and Technology, Shenzhen, 518055 (China).

Author contribution statement

H.L conceived and designed the study, prepared the samples, performed the experiments (unless otherwise stated), analyzed and interpreted the data, prepared and edited the manuscript. L.H edited the manuscript and confirmed synthesis by ^{1}H-NMR spectroscopy. Q.L and L.L.T assisted in SEM experiments. H.J.L assisted in single crystal experiments. P.F.T and F.H conceived the study, interpreted the data, edited the manuscript and supervised H.L.

4.1 Abstract

Supramolecular assemblies with built-in chirality attract great interest among researchers on account of their relationship to the biological or physical properties of materials. However, controlling supramolecular chirality and utilizing helicity in explorations of their potential applications is very challenging. Herein, the morphological transformation from microspheres to helical nanofibers with controllable handedness was achieved by the introduction of molecular chirality based on phenylalanine derivatives (TDAP), and the chirality of the self-assembled architectures that were achieved was nullified through the co-assembly of the equivalent TDAP enantiomers. The driving forces in the assembly process have been further investigated by scanning electron microscopy, variable temperature circular dichroism, and single-crystal X-ray diffraction. The molecular detection of achiral melamine based on *R*-TDAP-COOH supramolecular system was achieved by appearance of helicity and inversion in the co-assembly process. This work provides insight into the control of the helicity of chiral supramolecular structures in hierarchical self-assembly systems and explores the potential application of chiral materials in the biologic field.

4.2 Introduction

Chiral compounds play a vital role in organisms and their chirality is strongly related to their biomolecular functions. This has continuously attracted interest in biology, physics, chemistry, and material sciences.[1] Typical examples found in biological systems are sugars and amino acids which have L- and D-enantiomers. Recently, artificially chiral molecules have been designed and have displayed potential applications in chemistry,[2,3] materials science,[4] and biological systems.[5] For well-defined chiral architectures, a general strategy has been established to design building blocks based on biologically relevant molecules (such as amino acids or DNA).[6,7] Among these, supramolecular self-assembly, [8] which is an important method in nature to construct chiral ordered structures, opens an efficient way by noncovalent interactions, such as hydrogen-bonding, hydrophobic interactions, and π–π stacking to design functional materials with tailored properties.[9] Notably, chirality is also extended to the supramolecular level, and the stereochemical communication or chiral–chiral interaction between various chiral molecules becomes extremely important.[10] Molecular chirality has been well explored but the importance of supramolecular chirality and its biofunction has not yet been fully recognized.[11]

The self-assembly of chiral molecules into various architectures can be expressed across a broad range of structures, such as helices, Möbius strips, and gyroids. [12-15] Among these, chiral helicity exhibits great sensitivity to external stimuli. Manipulation of the chirality of nano-architectures is a promising way to develop the biological functions of artificial materials. Hence, focusing on in-depth studies of supramolecular chirality is currently vigorously pursued.[16] However, it is still challenging to fabricate desirable nano-

structures that can mimic helical biomolecules through self-assembly from artificial molecules and utilize the sensitivity of helicity to explore the potential biological application of such helical biomolecules. [16-17]

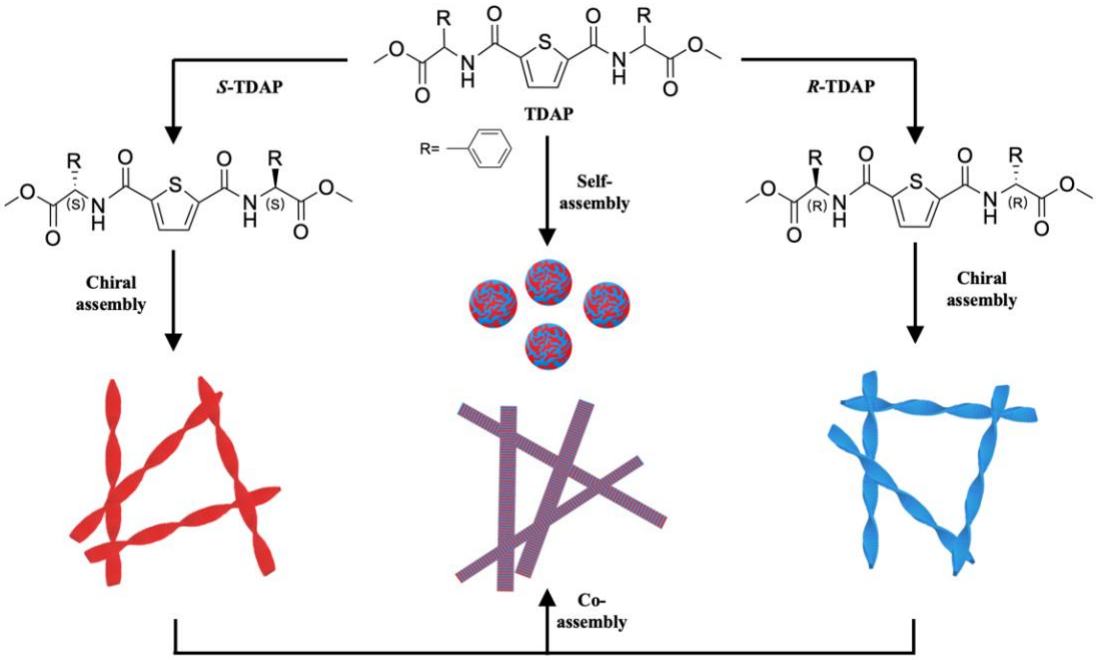

Scheme 4.1. Structure transition from microspheres (TDAP) to twisted fibers with different chirality (*S*-TDAP, P-helicity, and *R*-TDAP, M-helicity) and micro sheets without chirality (*R*+*S*-TDAP).

Herein, we report the synthesis of a thiophene-2,5-dicarboxamide with enantiomeric and racemic phenylalanine methyl ester branches (TDAP) (Scheme 4.1). Enantiopure *R*-TDAP, *S*-TDAP, and racemate TDAP were characterized by nuclear magnetic resonance (NMR) and liquid chromatography-mass (LC-MS) spectroscopy. Uniform microspheres were self-assembled from TDAP, while right-handed (P-helicity) and left-handed (M-helicity) nanofibers were constructed by the introduction of chiral enantiomers into the supramolecular system (Scheme 4.1). In comparison, by co-assembly with *R*-TDAP and *S*-TDAP, only racemic micro sheets lacking chiral characteristics were produced. To explore

the biological applications, the *R*-TDAP was modified as *R*-TDAP-COOH to take advantage of the helicity. Melamine (MA) can be detected by explicit morphology transformation including the appearance and inversion of helicity.

4.3 Materials and Methods

4.3.1 Materials

All reagents and solutions were purchased from Bide Pharm and Aladdin Chemistry (Shanghai, China).

4.3.2 Experimental Methods

4.3.2.1 Characterization Equipment

^{1}H NMR spectra were measured on a Bruker AVANCE 400 MHz spectrometer with tetramethylsilane (TMS) as the internal standard. SEM images were obtained from scanning electron microscope operated at 5 KV (Hitachi SU8230, Japan). Before SEM measurements, samples were prepared by depositing assembled solutions on silicon wafers, followed by drying and coating them with a thin layer of Au to increase the contrast. CD spectra of assembled architectures were measured on a Chirascan CD (Chirascan, UK). These samples were prepared by dissolving compounds in mixture of isopropanol/water (1:1) at 0.5 mg ml^{-1} and the prepared isobutanol solutions were heated at 90 °C for 1h, cooled to room temperature (25 °C), and aged for 24 h. Single-crystal X-ray Diffraction. The compound (approximately 10 mg) was dispersed in 2.0 mL of the mixture of isopropanol/water (1:1), then the suspension solution was heated to be transparent. The solutions were slowly cooled down to room temperature for crystallization. X-ray quality single crystals were isolated from mother liquor and quickly immersed in cryogenic oil and then mounted. Crystallographic data for the structures have been deposited to the Cambridge Crystallographic Data Centre as supplementary publication (CCDC no: 2090969−2090970).

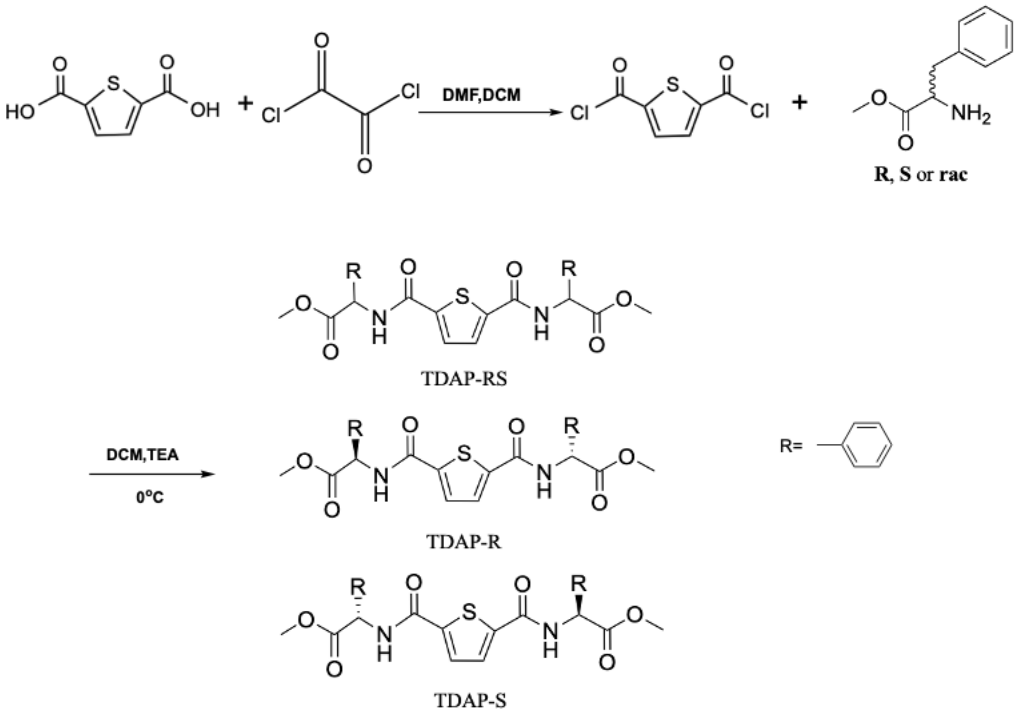

Scheme 4.2**.** Synthesis route of *R*-TDAP, *S*-, and racemate.

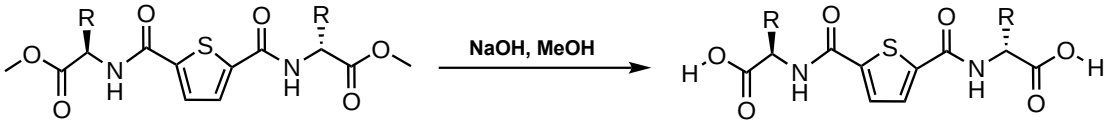

Scheme 4.3. Synthesis route of *R*-TDAP-COOH.

4.3.2.2 Synthesis of *R*-, *S*-, and racemate TDAP

Oxalyl chloride (2.2mL, 5.9 g, 46.8 mmol) was added under a N_2 atmosphere to a suspension of thiophene-2,5-dicarboxylic acid (1 g, 5.8 mmol) in 20 mL of dry DCM, and the reaction mixture was stirred at rt overnight. A clear solution was observed, and the solvents were removed to yield the thiophene-2,5-dicarbonyl dichloride as a brown solid. Dry DCM (20 mL) was charged to the acid chloride (311 mg, 1.5 mmol), and methyl *R*-, *S*-, or racemic phenylalanine hydrochloride (1.3 g, 7.5 mmol) was subsequently added to a mixture under a N_2 atmosphere. 2.6 ml (1.9 g, 18.7

mmol) of triethylamine was added dropwise to the mixture and stirred overnight at 0 °C. The solution was washed with 3.0% $NaHCO_3$, 1M HCl, and brine. The organic layer was dried over Na_2SO_4 and evaporated to yield *R*-, *S*-, or racemic TDAP as a white solid. Yield 2.8 g, 90.3%. ^1H NMR (400 MHz, CD_2Cl_2): δ [ppm] 7.49 (2H, s), 7.47-7.15 (10H, m), 6.50 (2H, *J* = 5.7 Hz, d), 5.11 (2H, *J* = 7.7, 5.7 Hz, dt), 3.77 (6H, s), 3.26 (4H, m). MS: cald for $C_{26}H_{26}N_2O_6S$ $[M]^+$ 494.56.; found, 495.1577, 495.1577 and 495.1576. (Appendix C, Figure C.1-4)

4.3.2.3 Synthesis of *R*-TDAP-COOH

Aqueous sodium hydroxide solution (2.0 M, 5 ml) was added under a N_2 atmosphere to a suspension of *R*-TDAP (1.1g, 2.2 mmol) in 5 mL of methanol, and the reaction mixture was stirred at rt overnight. Acidification of mixture was carried out with 3.0 M hydrogen chloride until pH reaches to 3.0 and gel-like precipitate appeared. The precipitate was filtered off, washed with distilled water 3–4 times, and lastly dried up in the vacuum oven to give *R*-TDAP-COOH (0.8g, 1.80 mmol, 81%), which was determined by ^1H NMR in DMSO: δ [ppm] 8.81 (2H, J = 8.2 Hz, d), 7.76 (2H, J = 2.2 Hz, d), 7.42-7.10 (10H, m), 4.53 (2H, J = 10.1, 7.7, 4.2 Hz, ddd), 3.26-2.98 (4H, m). (Figure C.5).

4.3.2.4 Self-assembly of TDAP and MA/R-TDAP-COOH

Self-assembly experiments were performed at concentrations of 0.5 mg ml^{-1}. *R*-TDAP, *S*-TDAP, and TDAP were dispersed into the solvent at room temperature (RT), then the suspension solutions were heated to transparency. After the solutions were cooled down to RT and aged for 24 h, the assembled structures were formed and were systematically investigated by scanning electron microscopy (SEM). Molecular detection experiments were performed with *R*-TDAP-COOH at 0.5 mg ml^{-1}. Then MA with different ratios was added in the solutions and followed by same self-assembly procedure.

4.4 Results and Discussion

4.4.1 Hierarchical self-assembly of TDAP

We investigated the self-assembled nanostructures of TDAP in different solvent systems including pure water and mixtures of methanol/H_2O (1:1), ethanol/H_2O (1:1), and isopropanol/H_2O (1:1) (Figures 4.1a, C6-8). Among the aggregations that were to obtained, the microspheres formed in a mixture of isopropanol and water (1:1), attracted our attention because of their uniformity and assembled potential (Figure 4.1a). For structural growth of *R*-TDAP and *S*-TDAP, the isopropanol/H_2O (1:1) is also the best solvent system like achiral TDAP, as a result of the suitable aggregating rates (Figure C.9 and 10). The self-assembly of enantiopure *R*-TDAP was carried out and twisted nanofibers with left-handedness (M-type) were obtained (Figure 4.1b). As expected, *S*-TDAP were organized into nanofiber with P-type helicity (Figure 4.1c). For the helical fiber architecture of *S*-TDAP, the helical pitch was in the range of 200−400 nm, while the left-handed helices formed from *R*-TDAP had helical pitch in the 300-500 nm range. Next, we mixed an equimolar ratio of *R*-TDAP and *S*-TDAP in the mixture of isopropanol and H_2O (1:1) at a concentration of 0.5 mg mL^{-1} and followed by the same assembly approach. Interestingly, in contrast to the initial supramolecular structures, the co- assembled morphology, in this case, was the rectangular platelet without helicity, and the width was in the range of 500-800 nm. In all, the statistics of structural features based on every different morphology including helical pitch, diameter, length and width were calculated in Table C.1. This indicated that the co-assembly of R- and S-compounds resulted in the nullification of chiral characteristics. These architectures obtained from co-assembly are also totally different from initial microspheres formed by racemic TDAP. As shown in Figure C.11, racemic sphere objects are composed of

molecules with three molecular configurations, while 2D platelet micelles are co-assembled with only two *R*-TDAP and *S*-TDAP components. In addition, we checked the morphological changes of *R*-, *R*+*S*-, and racemic-TDAP in the cooling assembly process at 80, 60, and 40 ℃ (Figure C.12). The formation process of nanofibers, sheets, and spheres showed a significant morphological transformation from crystallization aggregation to fibred growth, quite different from those of sheets, and spheres. Therefore, this reveals that molecular structures whose symmetric chiral centers have the same chiral configuration play a key role in the process of the formation of supramolecular architectures as chiral nanofibers or platelet micelles rather than microspheres.

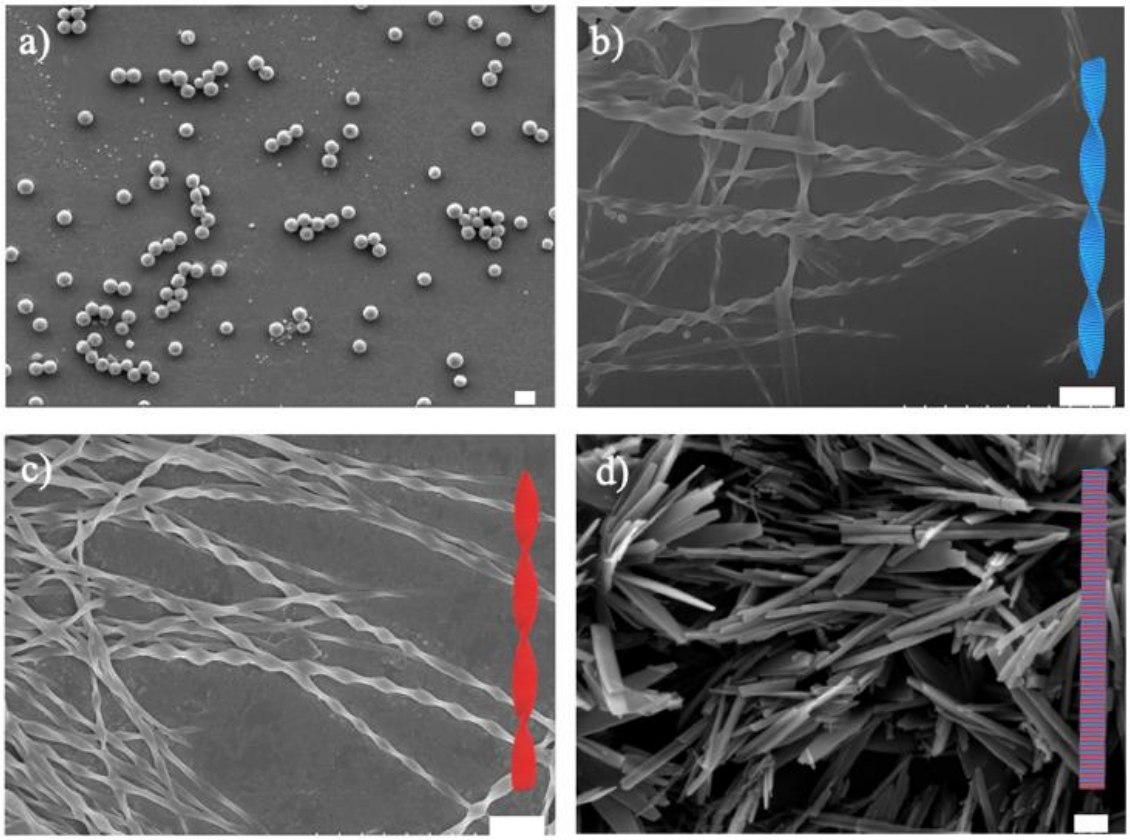

Figure 4.1 SEM images of (a) racemic, (b) *R*-, (c) *S*-, and (d) *R*+*S*-TDAP assembled architectures prepared in isopropanol/H_2O (1:1) mixtures. The schematic diagram of observed assemblies

showed the structure characteristic, consisting of aggregation of many single molecular chains. Scale bars in the SEM images are 1 μm.

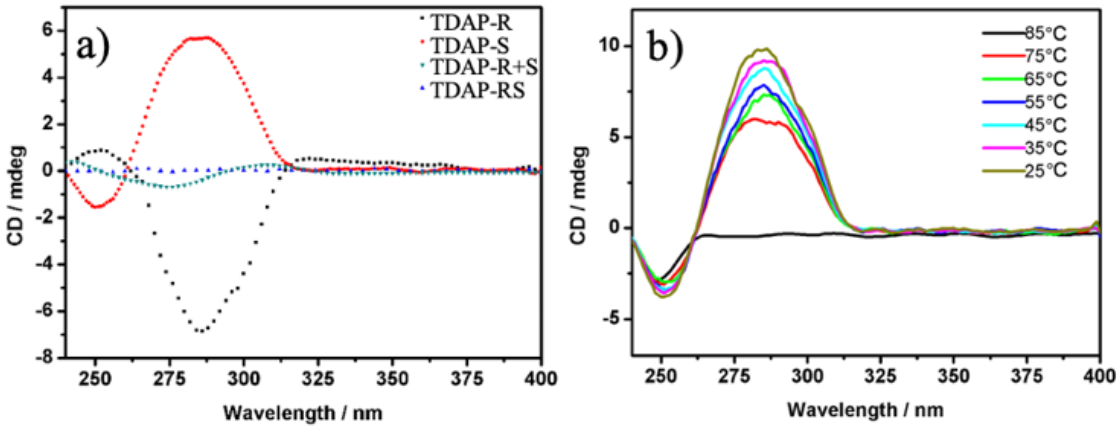

Figure 4.2 (a) CD spectra for *S*-, *R*-, racemic, and *R*+*S*-TDAP in the assembly state measured at 25.0 °C. (b) CD spectral changes of *S*-TDAP self-assemblies under different temperatures in the range of 25-85 °C with 10 °C intervals. These experiments were performed in the mixture of isopropanol/water (1:1) at 0.5 mg ml^{-1}.

4.4.2 Spectroscopic characterization of the chiral helices

CD spectroscopy was employed to examine the chiroptical properties. The CD spectrum of *S*-TDAP showed a significant Cotton effect with a strong positive (286 nm) and a weak negative CD signal (250 nm). The negative signal could be attributed to the intrinsic molecular chirality and the strong positive counterpart could be assigned to the chiral scattering of light caused by the interaction with the chiral supramolecular structure.[5] These results indicated that aromatic rings in the helical fibers are in a highly asymmetric environment. *R*-TDAP showed a mirror image of the signal of *S*-TDAP (Figure 4.2). The racemate TDAP displayed a linear CD signal, confirmed the cancelation of the optical rotation in the microspheres. The CD spectrum of the co-assembly system of *S*-TDAP and *R*-TDAP failed to reveal any peak at 286 nm, thus showing that there was no chirality in

the 2D platelet micelles because of the presence of opposing stereogenic centers. These results are further confirmation that molecular chirality and symmetric chiral configuration play key roles in the formation of supramolecular assembled architecture, which is consistent with SEM results. To further confirm the existence of chirality in the supramolecular, variable-temperature CD (VT-CD) spectra were applied with the *S*-TDAP (Figure 4.2b). It is clear that the interactions in the assembled structures were broken due to the increase in the extent of molecular motion at high temperatures. When initially heating to 75 °C, the positive peak at 286 nm gradually decreased because of heating-induced disassociation of the twisted nanofibers. Upon further heating to 85 °C, the spectrum showed CD silence at around 286 nm, suggesting the *S*-TDAP molecules were completely in the freely moving state. However, *S*-TDAP still revealed negative CD absorption at around 250 nm originating from molecular instinct chirality. All in all, the supramolecular chirality was mainly evident below 70 °C, while the signal of molecular chirality was dominant over 60 °C.

4.4.3 Exploring the Mechanism and Stoichiometry of Chiral assembly

In addition, single crystals of the enantiomers *S*-TDAP and *R*-TDAP were carried out (Figure 4.3 and Table C.2). It was obvious that the molecular structures of the two TDAP isomers were symmetric as mirror images. In the case of the TDAP enantiomers, these molecules were arranged in a molecular chain and connected with each other by H-bonding interactions, which were formed between the carbonyl (C=O) and the secondary amine (N-H) groups with an interaction distance of 2.31 Å. It can be seen that the transfer directions of the H-bonding in the molecular chains are different as mirror images of each other. The different transfer directions of the H-bonding induce the different molecular arrangements

and the packing of the molecular chains in different conformations. Aggregation of multiple molecular chains leads to the final helical morphologies with the different supramolecular chirality (Figure 4.3e and 4.3f). For the *R*+*S*-TDAP co-assembly system, it could be inferred that the H-bonding interactions would be disordered and the dominant orientation of the molecular arrangement would disappear, and this kind of multiple molecular chain aggregations might lead to the 2D tape-like architectures lacking helicity (Figure 4.3g).

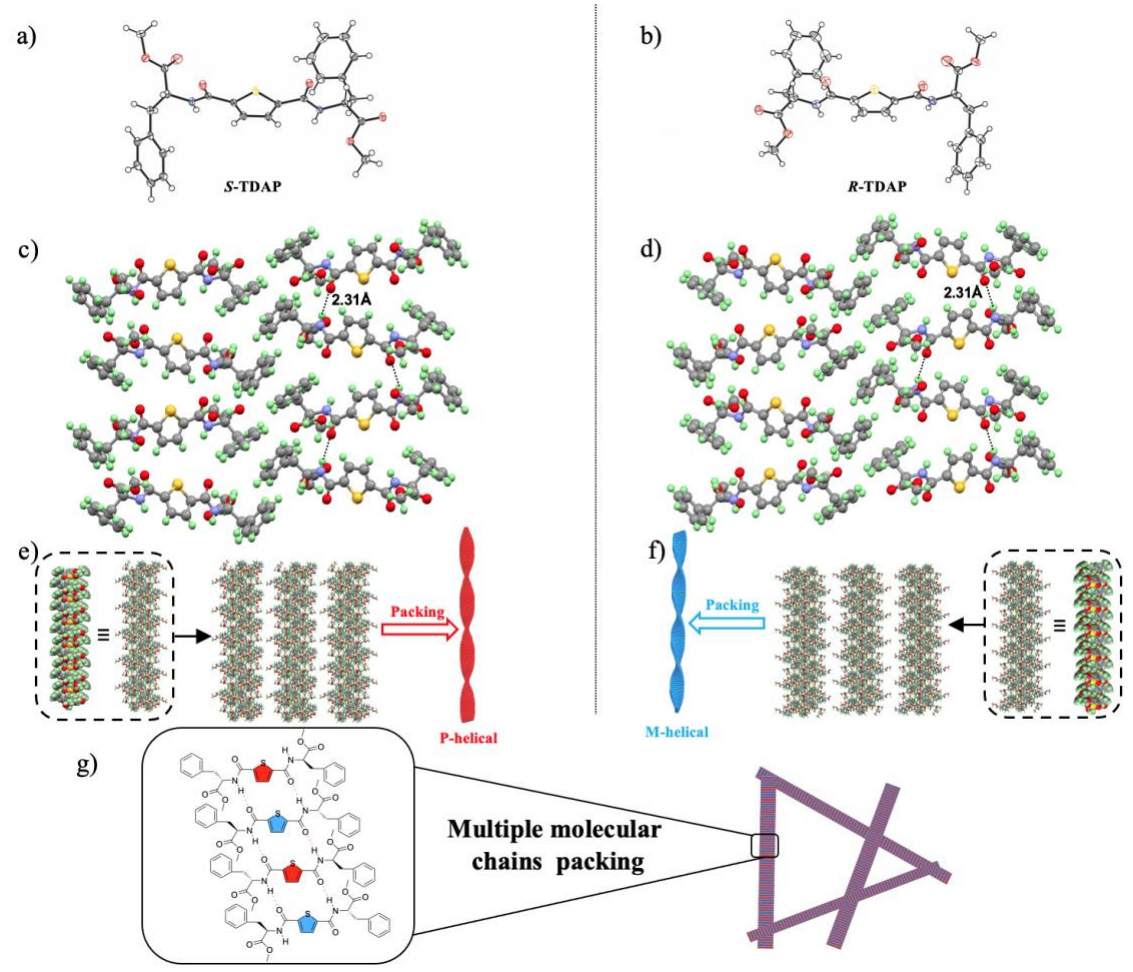

Figure 4.3 Single-crystal structures of *S*-TDAP and *R*-TDAP: (a-b) Molecular structures of thermal ellipsoids; (c-d) Intermolecular H-bond interactions; (e-f) Three-dimensional packing structures. Different molecular arrangements result in different handedness. In these figures, the

molecular chains were observed as spacefilling models and the stacking modes were observed as ball and stick models. (g) The possible co-assembly mechanism of *R*+*S*-TDAP architecture (*R*-TDAP and *S*-TDAP are shown in blue and red, respectively.).

4.4.4 Molecular detection of melamine

Among the supramolecular interactions in the assembly systems, the stacking of the hydrophobic phenyl core of the phenylalanine-based supramolecular system and the hydrogen bonding based on carboxylic acid moieties may provide an approach for efficient co-assembly with achiral structural analogues.[7] So we synthesized the *R*-TDAP-COOH to explore biological applications (Scheme 4.3, and Figure C.5). Then we tested its self-assembly in the H_2O, which stimulates the biological assembled situation without organic solvents. The achieved morphology was a nanofiber with no twist or chirality (Figure 4.4b). Due to the appearance of carboxylic acid moieties after functionalization, the new H-bonding was formed between carboxylic acid (O-H) and the original amide group. This interaction hindered the initial intermolecular H-bonding resulting in the disappearance of helicity and destruction of the consistency of chirality. We tried to co-assemble *R*-TDAP-COOH with MA (1:1) by the heating-cooling process in H_2O. The achieved morphology was long twisted fiber with mainly P helicity (Figure 4a). In addition, we also tried to utilize *R*-TDAP-COOH to recognize MA structural analogue, Cyanuric acid (CA). There was no helicity in the co-assembly system (Figure 4.4c), which proved the specificity of TDAP recognition system for MA. SEM images were also recorded by varying the ratios of MA/ *R*-TDAP-COOH. SEM images showed helical fibers with a gradual increase in pitch and

diameter as the proportion of melamine analogues increases (Figure 4.5 and Figure C.13, 14).

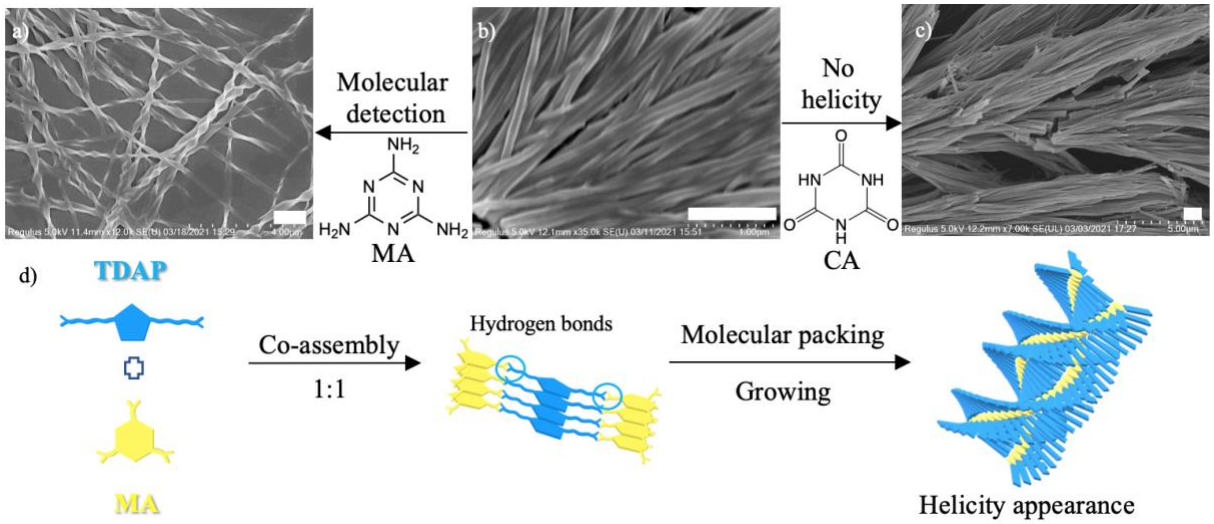

Figure 4.4 SEM images of (a) MA/*R*-TDAP-COOH (b) *R*-TDAP-COOH and (c) CA/ *R*-TDAP-COOH assembled architectures. Scale bars in the SEM images are 1 μm. (d) Schematic representation for the molecular detecting process in MA/TDAP co-assembly system.

We tried to test limit of recognition of MA (0.5 mg ml^{-1}, 0.25 mg ml^{-1}, 0.1 mg ml^{-1}, 0.05 mg ml^{-1} and 0.01 mg ml^{-1}) (Figure C.15). These results showed that molecular recognition by helicity appearance can be realized even at 0.05 mg mL^{-1}. It indicated that molecular recognition by the TDAP system can be realized even at very low concentrations. Then variable-temperature ^{1}H NMR spectra were also measured (Figure C.16). The results showed that the proton signals of the amine in MA at around 5.9 ppm shifted upfield, broadened and decreased in the intensity [18] as the temperatures increased, suggesting the formation of carboxylic acid-amine hydrogen bonds within assemblies. As the temperature increased, the upfield shift of the protons of the amide group in TDAP-COOH at around 8.7 ppm implied the presence of similar H-bonding with *R*-TDAP nanofibers. These

characteristics can be interpreted as an indication of restricted freedom of motion of the proton due to the H-bonding between the amide of MA and the carboxylic acid groups of TDAP molecules at RT. In the detection system, the H-bonding based on carboxylic acid moieties could be restrained by the addition of MA leading to the reconstruction of helicity. Meanwhile, the new H-bonding between the amine of MA and the carboxylic acid groups of TDAP was formed, which contributed to the construction of new helicity. (Figure 4.4d) Thus multiple H-bonding sites of melamine and self-aggregation of TDAP, play dominant roles in regulating the molecular arrangement, so MA is considered to be a stimulus in detecting process. In all, these SEM, TEM, and NMR results suggest that molecular detection of MA by TDAP system can be achieved by the supramolecular assembly.

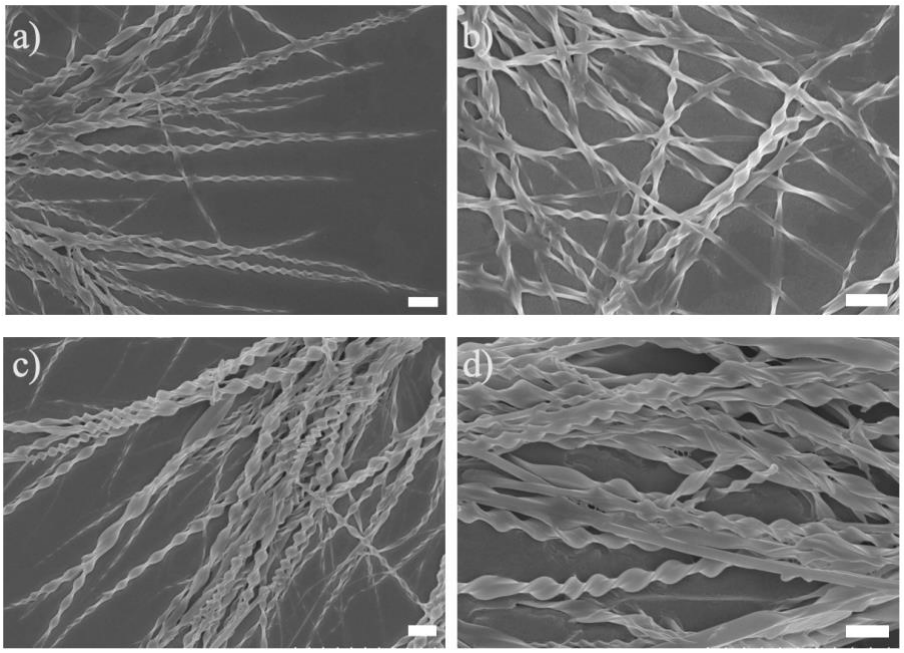

Figure 4.5 SEM images of TDAP/MA at molar ratios of (a)1: 0.5, (b) 1:1, (c) 1:2, and (d) 1:3 co-assembled architectures. The concentration of *R*-TDAP-COOH in all samples was 0.5 mg mL^{-1}. Scale bars in the SEM images are 1 μm.

4.5 Conclusions

In summary, various supramolecular architectures and morphology transformations were achieved by hierarchical self-assembly based on thiophene derivatives with enantiomeric or racemic phenylalanine ester arms. The morphology transformation from microspheres to nanofibers was achieved through the introduction of molecular chirality. The handedness of twisted fibers can be adjusted precisely by the regulation of molecular chirality. The molecular chirality is transmitted into the supramolecular level through the hydrogen bond which has been confirmed as a driving force. In addition, we synthesized *R*-TDAP-COOH and used it to explore its biological application by utilizing co-assembly through supramolecular interactions. Helicity appearance and inversion were observed for the TDAP-MA system, which was used to provide a detection method for melamine. In conclusion, the present work provides valuable insight into the control of supramolecular chirality and also explores the potential applications in functional biomaterials.

4.6 References

[1] Ghosh D.; Farahani A. D.; Martin A. D.; Thordarson P.; Damodaran K. K., Unraveling the Self-Assembly Modes in Multicomponent Supramolecular Gels Using Single-Crystal X-ray Diffraction. Chem. Mater. 2020, 32 (8), 3517-3527.

[2] Jiang J.; Meng Y.; Zhang L.; Liu M., Self-Assembled Single-Walled Metal-Helical Nanotube (M-HN): Creation of Efficient Supramolecular Catalysts for Asymmetric Reaction. J. Am. Chem. Soc. 2016, 138 (48), 15629-15635.

[3] Ariga K.; Mori T.; Kitao T.; Uemura T., Supramolecular Chiral Nanoarchitectonics. Adv. Mater. 2020, 32 (41), 1905657.

[4] Wu H.; Zhou Y.; Yin L.; Hang C.; Li X.; Ågren H.; Yi T.; Zhang Q.; Zhu L., Helical Self-

Assembly-Induced Singlet–Triplet Emissive Switching in a Mechanically Sensitive System. J. Am. Chem. Soc. 2017, 139 (2), 785-791.

[5] Liu J.; Yuan F.; Ma X.; Auphedeous D. I. Y.; Zhao C.; Liu C.; Shen C.; Feng C., The Cooperative Effect of Both Molecular and Supramolecular Chirality on Cell Adhesion. Angew.Chem.Int. Ed. 2018, 57 (22), 6475-6479.

[6] Fan Y.; Xing Q.; Zhang J.; Wang Y.; Liang Y.; Qi W.; Su R.; He Z., Self-Assembly of Peptide Chiral Nanostructures with Sequence-Encoded Enantioseparation Capability. Langmuir 2020, 36 (35), 10361-10370.

[7] Chao Z. C.; Lu H. W.; Xiao F.; Shao C.; Wei Z. X.; Yu J. T.; Zhang X. D.; Lin L.; Tian L. L., Robust and Tumor-Environment-Activated DNA Cross-Linker Driving Nanoparticle Accumulation for Enhanced Therapeutics. CCS Chem. 2020, 2 (5), 349-361.

[8] Han L.; Fan H.; Zhu Y. L.;Wang M.J.;Pan F.; Yu D. P.;Zhao Y.; He F., Precisely Controlled Two-Dimensional Rhombic Copolymer Micelles for Sensitive Flexible Tunneling Devices. CCS Chem. 2020, 3 (5), 1399-1409.

[9] Wang F.; Feng C. L., Metal-Ion-Mediated Supramolecular Chirality of l-Phenylalanine Based Hydrogels. Angew.Chem.Int. Ed. 2018, 57 (20), 5655-5659.

[10] Minakawa M. ; Nakagawa M.; Wang K. H.; Imura Y.; Kawai T., Controlling Helical Pitch of Chiral Supramolecular Nanofibers Composed of Two Amphiphiles. Bull. Chem. Soc. Jpn. 2020, 93 (10), 1150-1154.

[11] Yeom J.; Guimaraes P. P. G.; Ahn H. M.; Jung B. K.; Hu Q.; McHugh K.; Mitchell M. J.; Yun C. O.; Langer R.; Jaklenec A., Chiral Supraparticles for Controllable Nanomedicine. Adv. Mater. 2020, 32 (1), 1903878.

[12] Thornalley K. A.; Laurini E.; Pricl S.; Smith D. K., Enantiomeric and Diastereomeric Self-

Assembled Multivalent Nanostructures: Understanding the Effects of Chirality on Binding to Polyanionic Heparin and DNA. Angew.Chem.Int. Ed. 2018, 57 (28), 8530-8534.

[13] Liu G.; Sheng J.; Teo W. L.; Yang G.; Wu H.; Li Y.; Zhao Y., Control on Dimensions and Supramolecular Chirality of Self-Assemblies through Light and Metal Ions. J. Am. Chem. Soc. 2018, 140 (47), 16275-16283.

[14] Ouyang G.; Ji L.; Jiang Y.; Würthner F.; Liu M., Self-assembled Möbius strips with controlled helicity. Nat. Commun. 2020, 11 (1), 5910.

[15] Uemura N.; Kobayashi T.; Yoshida S.; Li, Y.; Goossens K.; Zeng X.; Watanabe G.; Ichikawa T., Double-Gyroid Nanostructure Formation by Aggregation-Induced Atropisomerization and Co-Assembly of Ionic Liquid-Crystalline Amphiphiles. Angew.Chem.Int. Ed. 2020, 59 (22), 8445-8450.

[16] Sun Y.; Li S.; Zhou Z.; Saha M. L.; Datta S.; Zhang M.; Yan X.; Tian D.; Wang H.; Wang L.; Li X.; Liu M.; Li H.; Stang P. J., Alanine-Based Chiral Metallogels via Supramolecular Coordination Complex Platforms: Metallogelation Induced Chirality Transfer. J. Am. Chem. Soc. 2018, 140 (9), 3257-3263.

[17] Ogasawara M.; Lin X.; Kurata H.; Ouchi H.; Yamauchi M.; Ohba T.; Kajitani T.; Fukushima T.; Numata M.; Nogami R.; Adhikari B.; Yagai S., Water-induced self-assembly of an amphiphilic perylene bisimide dyad into vesicles, fibers, coils, and rings. Mater. Chem. Front. 2018, 2 (1), 171-179.

[18] Wang F.; Qiu H. B.; Feng C. L., Wrapping Chiral Nanoribbons into Coiled and Condensed Microstructures in Supramolecular Hydrogels. Adv. Funct. Mater. 2020, 30 , 200293

CHAPTER 5 MORPHOLOGIACALLY TUNABLE RECTANGULAR MICROSHEETS AND MICROSAWS CONSTRUCTED BY HIERARCHICAL SELF-ASSEMBLY BASED ON HYDROGEN BONDS

Published paper

Heng Li,[ab] Liang Han,[a] Qing Li,[e] Hengtao Wang,[a] Paco Fernández-Trillo,[bc] and Feng He[ad]

Macromolecular Rapid Communication, **2022**, accepted.

a. Shenzhen Grubbs Institute and Department of Chemistry, Southern University of Science and Technology, Shenzhen, 518055 (China).
b. School of Chemistry, University of Birmingham, B15 2TT, UK.
c. Departamento de Química, Facultade de Ciencias and Centro de Investigacións Científicas Avanzadas (CICA), Universidade da Coruña A Coruña, 15071 (Spain).
d. Guangdong Provincial Key Laboratory of Catalysis, Southern University of Science and Technology, Shenzhen, 518055 (China)
e. Department of Materials Science and Engineering, Southern University of Science and Technology, Shenzhen, 518055 (China).

Author contribution statement

H.L conceived and designed the study, prepared the samples, performed the experiments (unless otherwise stated), analyzed and interpreted the data, prepared and edited the manuscript. L.H edited the manuscript and confirmed synthesis by ^{1}H-NMR spectroscopy. Q.L assisted in SEM experiments. H.T.W assisted in single crystal experiments. P.F.T and F.H conceived the study, interpreted the data, edited the manuscript and supervised H.L.

5.1 Abstract

Amino acid derivatives TDAV as new building blocks for two-dimensional (2D) structure assembly have been developed and employed to fabricate various square and rectangular microsheets with tunable aspect ratios by controlling the polarity of solvent. By the introduction of chirality, the novel microsaw and were also achieved. It provides a new approach to prepare various kinds of unique supramolecular 2D materials with controllable shapes and sizes for the future biological device.

5.2 Introduction

Two-dimensional (2D) nanomaterials have attracted a great deal of attention and have been the subject of intensive research in the last decades, as a result of their unique physical, biological, electronic optical, and chemical properties.[1, 2] Recently, various 2D micro- and nano-structures have been constructed from inorganic, organic molecules[3], metal salts[4], peptides[5], and block copolymers[6], including square,[7] rectanglar,[8] hexagon,[9] and diamond[6]. These 2D nanomaterials have opened novel opportunities in the fields of catalysis,[10] biological nanomaterial,[9] and optoelectronic devices. [11] Therefore, it is still an important issue to develop new building blocks for the construction of unique 2D structures with desired characteristics.

Strategies that lead to well-controlled construction of 2D organic layers with long-range structural ordering and high uniformity over large areas have thus been widely pursued. Among these, by supramolecular self-assembly (SA), which widely exists in nature, natural biomolecules (protein, polypeptide, DNA, etc.) were included in various fundamental processes in life fold into complex structures. Recently, many efforts have been made in the construction of diversified supramolecular materials with controllable dimensions, sizes and manners by self-assembly, which also displayed superiority and functionality. In particular, molecular self-assembly opens an efficient way by covalent (e.g., click chemistry)[12] and noncovalent strategies such as hydrophobic interactions, and π−π stacking. Of particular interest are the biological derivative block (e.g., protein, DNA, amino acids, and peptide) that can be designed in a well-defined manner to favor self-assembly to 2D architectures. Although amino acid derivatives and peptides represent an important class of supramolecular units with tendency toward aggregating into 1D nanomaterials (e.g., nanotubes and nanofiber),[13, 14] the design of 2D platelet structures is

infrequently reported. This is because the H-bonding arising from amide groups dominates 1D peptide self-assembly preferentially along the direction parallel to H-bonding. It is different and insufficient to fabricate 2D supramolecular assemblies containing hydrogen bonding interactions with controllable sizes and scales.[15] From the unique excellent properties and structural characteristics perspective, it is a challenging and elusive task to design and fabricate 2D architectures by precisely self-assembly behavior of building blocks utilizing amino acid derivatives.

Recently, we have demonstrated the formation of 1D helices with controllable chirality by using amino acid derivate (TDAP) containing phenylalanine methyl ester, which simulated the self-assembly behavior of peptides.[16] Interestingly, by co-assembly of enantiomers, platelet micelles with low uniformity were also achieved but we were unable to control their precise shapes or sizes presumably because of the steric hindrance around H-bonding site. In order to form well-defined 2D assemblies with higher uniformity, we focused on changing the arrangement of H-bonding by engineering the side chains around H-bonding site. (Scheme 5.1) Herein, we report a new design of the amino acid derivate (TDAV) containing valine methyl ester arms forming 2D uniform square microsheets in cosolvent of alcohols and H_2O. Changing the polarity of the mixture solvent or tuning water content leaded to a precisely morphological transition from square to rectangular platelets. In addition, by using opposite chirality of TDAV to assembly, new microsaw was also achieved, which was scarcely reported before.

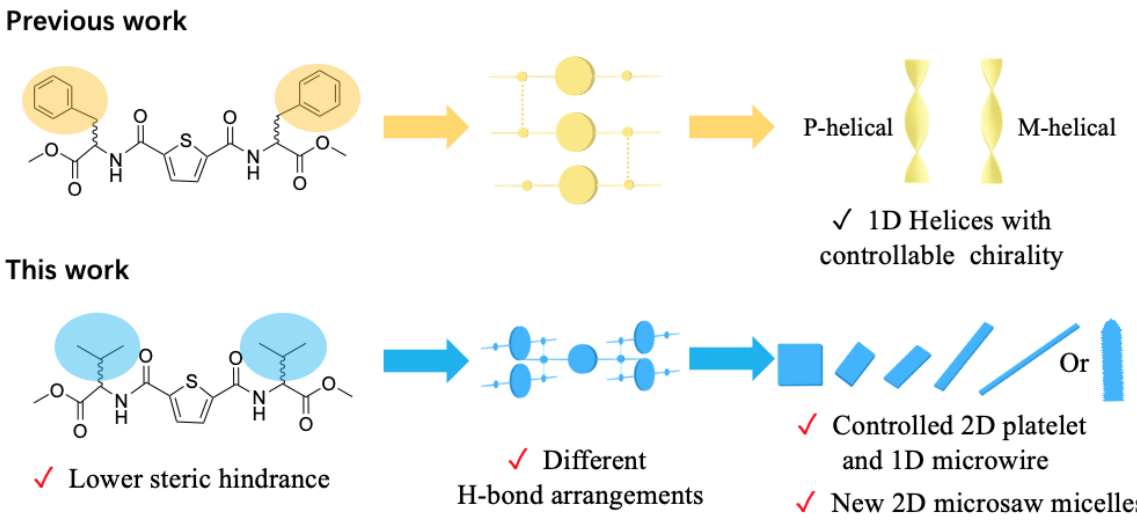

Scheme 5.1. New strategy to obtain well-defined 2D microsheets of square and rectangular using new amino acid derivate TDAV

5.3 Materials and Methods

5.3.1 Materials

All reagents and solutions were purchased from Bide Pharm and Aladdin Chemistry (Shanghai, China).

5.3.2 Methods

5.3.2.1 Characterization Equipment

^{1}H NMR spectra were measured on a Bruker AVANCE 400 MHz spectrometer with tetramethylsilane (TMS) as the internal standard. SEM images were obtained from scanning electron microscope operated at 5 KV (Hitachi SU8230, Japan). Before SEM measurements, samples were prepared by depositing assembled solutions on silicon wafers, followed by drying and coating them with a thin layer of Au to increase the contrast. The average statistics of structural features of every different morphology were calculated after tracing 50 different morphological structures by hand.

Single-crystal X-ray Diffraction. The compound (approximately 1 mg) was dispersed in 1.0 mL of the mixture of dichloromethane, then the petroleum (5 ml) was slowly added in the solution, and leave it for one week. X-ray quality single crystals were isolated from mother liquor and quickly immersed in cryogenic oil and then mounted. Crystallographic data for the structures have been deposited to the Cambridge Crystallographic Data Centre as supplementary publication (CCDC no: 2132627).

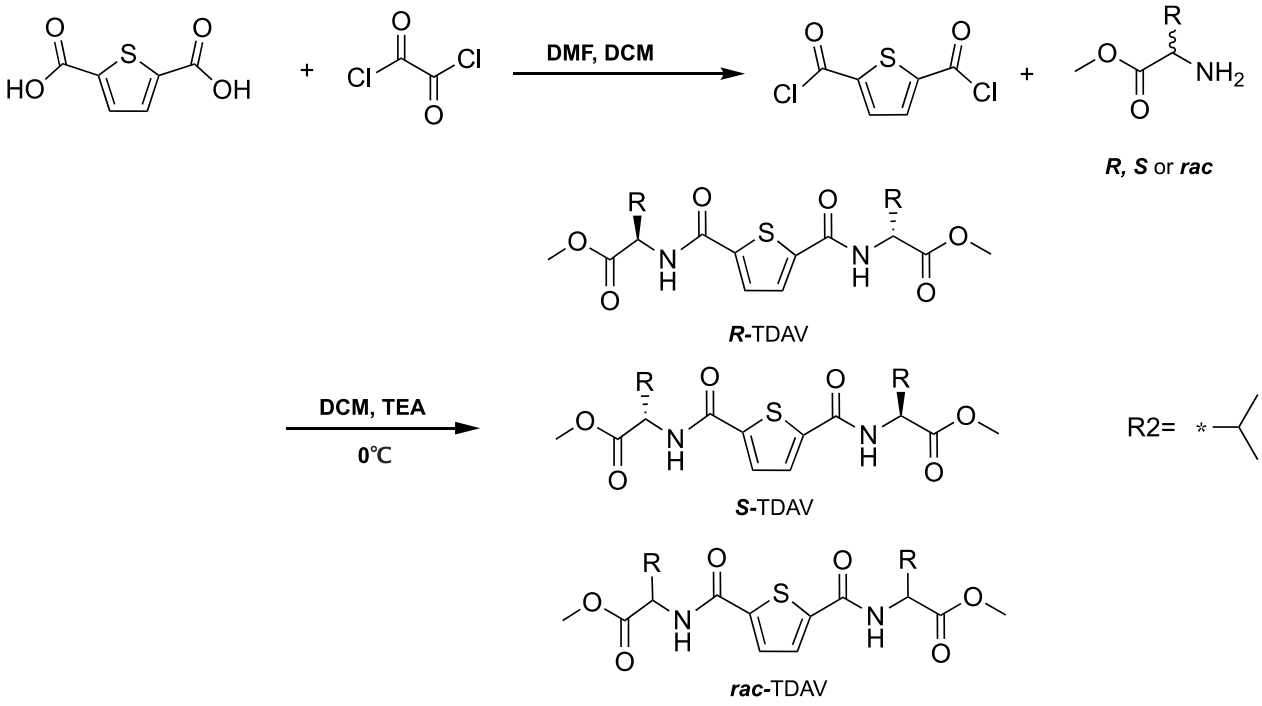

Scheme 5.2. Synthesis route of *R*-, *S*-, and racemate TDAV.

5.3.2.2 Synthesis of *R*-, *S*-, and racemate TDAV

Oxalyl chloride (2.2mL, 5.9 g, 46.8 mmol) was added under a N_2 atmosphere to a suspension of thiophene-2,5-dicarboxylic acid (1 g, 5.8 mmol) in 20 mL of dry DCM, and the reaction mixture was stirred at rt overnight. A clear solution was observed, and the solvents were removed to yield the thiophene-2,5-dicarbonyl dichloride as a brown solid. Dry DCM (20 mL) was charged to the

acid chloride (311 mg, 1.5 mmol), and methyl R-, S-, or racemic valine hydrochloride (1.3 g, 7.5 mmol) was subsequently added to a mixture under a N2 atmosphere. 2.6 mL (1.9 g, 18.7 mmol) of triethylamine was added dropwise to the mixture and stirred overnight at 0 °C. The solution was washed with 3.0% $NaHCO_3$, 1M HCl, and brine. The organic layer was dried over Na_2SO_4 and evaporated to yield *R*-, *S*-, or racemic TDAP as a white solid. Yield 531 mg, 89.1%. ^1H NMR (400 MHz, CD_2Cl_2): δ [ppm] 7.55 (s, 2H), 6.54 (d, J = 8.6 Hz, 2H), 4.70 (dd, J = 8.6, 5.1 Hz, 2H), 3.80 (s, 6H), 2.29 (td, J = 6.9, 5.2 Hz, 2H), 1.02 (t, J = 6.8 Hz, 12H). MS : cald for $C_{18}H_{26}N_2O_6S$ $[M]^+$ 398.15; found, 399.15, 399.15, and 399.16. (Appendix D, Figure D1-D4).

5.3.2.3 Self-assembly of TDAV

Self-assembly experiments were performed at concentrations of 0.5 mg mL^{-1}. *R*-TDAV, *S*-TDAV, and TDAV were dispersed into the solvent at room temperature (RT), then the suspension solutions were heated to transparency. After the solutions were cooled down to RT and aged for 24 h, the assembled structures were formed and were systematically investigated by scanning electron microscopy (SEM).

5.4 Results and Discussion

5.4.1 Synthesis and self-assembly of TDAV

In order to form new 2D well-defined micelles, we developed a rational 2D supramolecular construction methodology through H-bond based on amino acid derivatives. The thiophene-2,5-dicarboxamide with enantiomeric or racemic valine methyl ester branches (TDAV) was synthesized as building block because of high crystallinity, and ease of modification, which were characterized by nuclear magnetic resonance (NMR) and liquid chromatography-mass (LC-MS). Self-assembly experiments were performed at concentrations of 0.5 mg ml^{-1}. TDAV were dispersed into the solvent at room temperature, then the suspension solutions were heated to be transparent. After the solutions were cooled down to room temperature following by aging for 24 h, the assembled structures were formed. We systematically investigated the assemblies of *S*-TDAV in different solvent systems including the mixture of methanol/water (1:1), ethanol/water (1:1), and isopropanol/water (1:1) by scanning electron microscopy (SEM). In the mixture of methanol/water (1:1), well-defined 2D rectangular architectures were obtained (Figure 5.1a-c). The number-average lengths (L_n) of rectangular micelles were 66.02 μm and the widths were roughly 10 μm. When the ethanol was employed to replace methanol in assembly system, the aspect ratios of new rectangular micelles were much lower than that of initial 2D micelles. The L_n of rectangular micelles were 56.41 μm and the widths were roughly 30 μm. Then we continued to decrease the polarity of assembly solvent by using isopropanol/ H_2O (1:1), and the morphological transitions were observed. The aspect ratios of obtained micelles continued to decrease and 2D square architectures were achieved (Figure 5.1g-i) with the L_n as roughly 23.44 μm. Noting that the length of the rectangular structures formed in mixture of methanol and H_2O was several times larger than that in isopropanol mixture solution. Meanwhile, the uniformity of square micelles was

obviously better compared with the rectangular micelles obtained in the methanol/H_2O system. Due to the differences of solubility and polarity of cosolvents, the aggregation rate of assemblies in the isopropanol cosolvent should be slowest among three assembly systems, leading to best uniformity of achieved morphology. These observed morphological transition also indicated that the solvent properties profoundly influenced the molecular packing, and thus induced differences in the resulting micro-structures. It revealed that the aspect ratios of obtained 2D micelles increased as the growth rate increased.

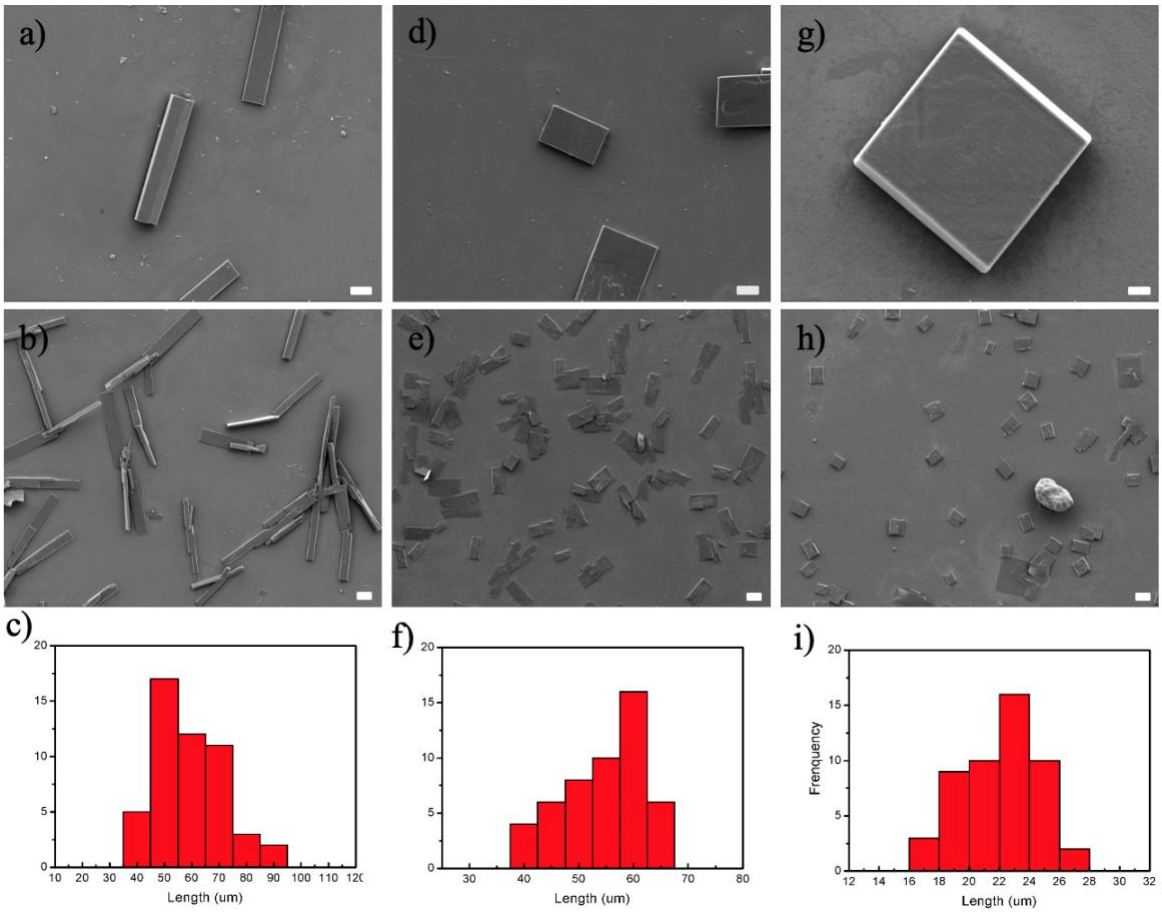

Figure 5.1 SEM images and contour length distributions of 2D square and rectangular micelles prepared from TDAV in 0.1 mg ml^{-1} cosolvents solution of (a-c) methanol and water (1:1); (d-f) ethanol and water (1:1); (g-i) isopropanol and water (1:1). Scale bars in TEM photos are 10 μm.

5.4.2 Tuning the morphology of 2D micelles by controlling water content

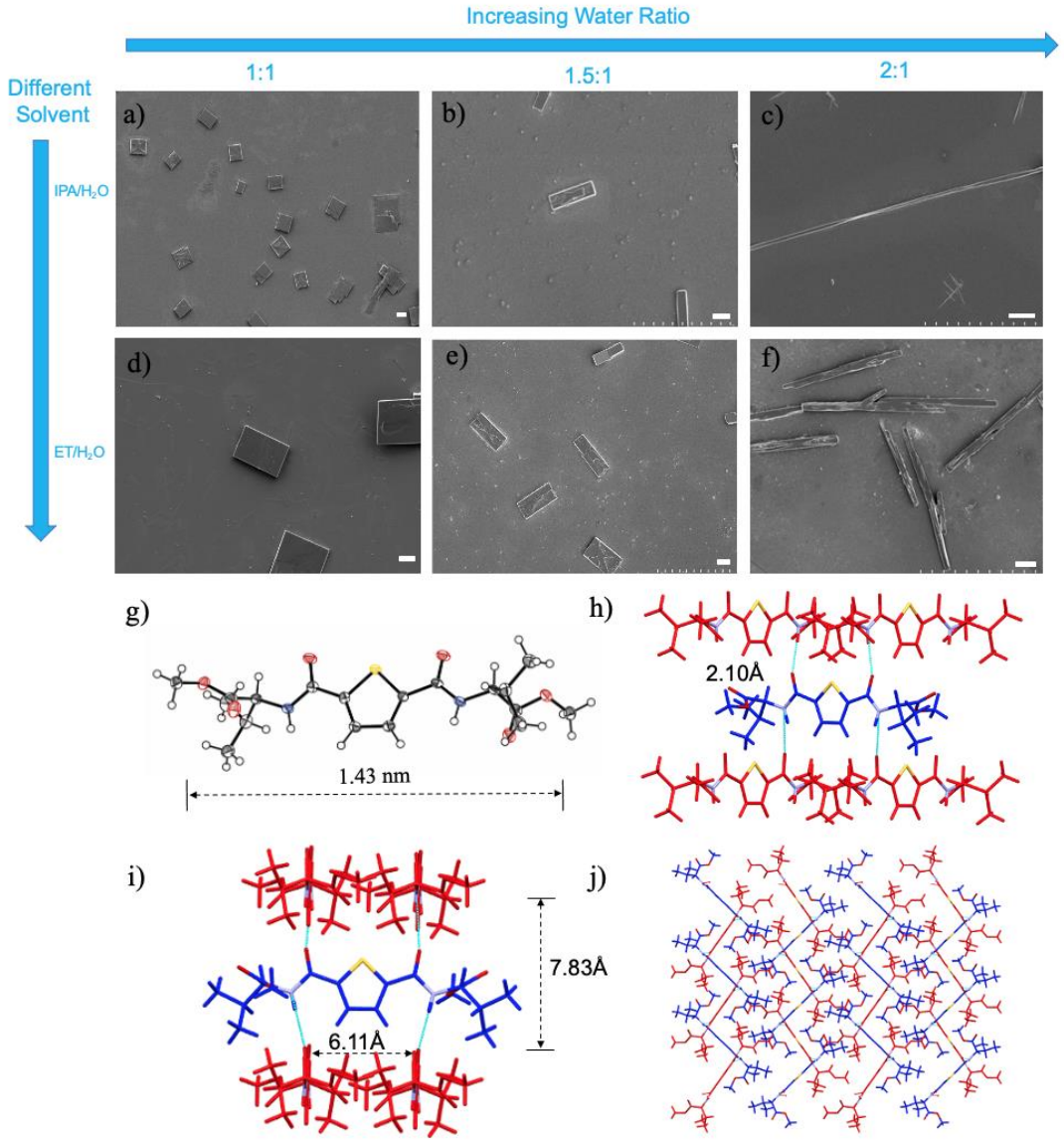

Figure 5.2 SEM images 2D and 1D micelles prepared from *S*-TDAV in 0.5 mg ml^{-1} cosolvents solution of (a-c) H_2O/isopropanol (1:1, 1.5:1, and 2:1) and (d-f) H_2O/ethanol (1:1, 1.5:1, and 2:1). Single-crystal structures of *S*-TDAV: (g) Molecular structures of thermal ellipsoids; (h, i) Intermolecular H-bond interactions; (i) Molecular packing structures. In these figures, the stacking modes were observed as ball and stick models.

To further investigated the effects of cosolvent properties for 2D assembled platelets, the different water/alcohol ratios of the cosolvents for the assembly systems were employed as 2:1, 1.5:1, 1:1. The water is the poor solvent with low solubility and high polarity for the TDAV. In the case of isopropanol/water, as the water ratio was increased, the original square micelles was transformed to rectangular micelles with higher aspect ratio (Figure 5.2a, b). When the water content continued to be increased, the aspect ratio of obtained micelles also increased resulting in 1D ultra-long microwire rather than 2D micelles, whose length is more than 50 μm (Figure 5.2c). In the case of the cosolvent of ethanol, as the water/isopropanol ratio was increased to 1.5:1, the aspect ratio of new rectangular micelles became larger, whose tendency of morphological transformation is consistent with the cased in the isopropanol mixture. When the water ratio was increased to 2:1, the rectangular micelles with super high aspect ratio and large length were achieved in Figure 5.2 f. In general, with the content of poor solvent as water improved, the growth rate of 2D micelles became faster resulting in larger aspect ratio of 2D micelles and even the 1D ultra-long microwire, which is consistent with the above results.

To figure out molecular packing and assembly characteristics of *S*-TDAV, the single crystal of TDAV was employed to investigated. Analysis of the crystal data revealed that the carbonyl (C=O) and the secondary amine (N-H) of the TDAV formed the hydrogen bonding with interaction distances as 2.10 Å (Figures 5.2h). In the crystal structure, one TDAV molecule was connected with four other molecules by H-bonds to form layer-like structures. In general, for the case of peptides or amino acid derivates, the H-bonding arising from amide groups dominates self-assembly preferentially along the direction parallel to H-bonding resulting in tendency towards the 1D nanostructures.[13] However, even with the existence of molecular chirality, these layers based on derivate *S*-TDAV were oriented perpendicular to each other layer without one specific stacking

direction resulting in the formation of plane multilayer structures (Figures 5.2h). From the supramolecular point of view, this kind of molecular multilayer arrangement in the crystal explained the final assembly architectures as 2D platelet micelles without any twist or chiral characteristic. In the other hand, the different polarity and solubility of cosolvents caused different aggregation rate of assemblies, so these 2D platelets were obtained with different shapes and scales, which resulted in morphological transition from rectangular micelles to square micelles.

5.4.3 Effect of chirality on the morphology 2D platelet

Then we investigated the effect of molecular chirality on supramolecular assemblies, *R*-TDAV and *RS*-TDAV were used as building block to fabricate new architectures. Self-assembly experiments were performed in the mixed solvent methanol/H_2O (1:1) at concentrations of 0.5 mg mL^{-1}, in which rectangular micelles was obtained by using *S*-TDAV (Figure 5.1a, b). In the case of *R*-TDAV, new 2D micelles as saw-like structures were achieved rather than square or rectangular platelets. (Figure 5.3b, c) The scales of microsaw micelles were larger than the scales of rectangular micelles, while the uniformity was worse. The "sawtooth" was formed from small rectangular platelets arranging in a ladder way. The length of the sawtooth was more than 10 μm, and width was roughly 8 μm. However, for the racemic TDAV, layer-like plane structures without specific advantage growth orientation were obtained (Figure D5a, b), which still kept 2D growth tendency.

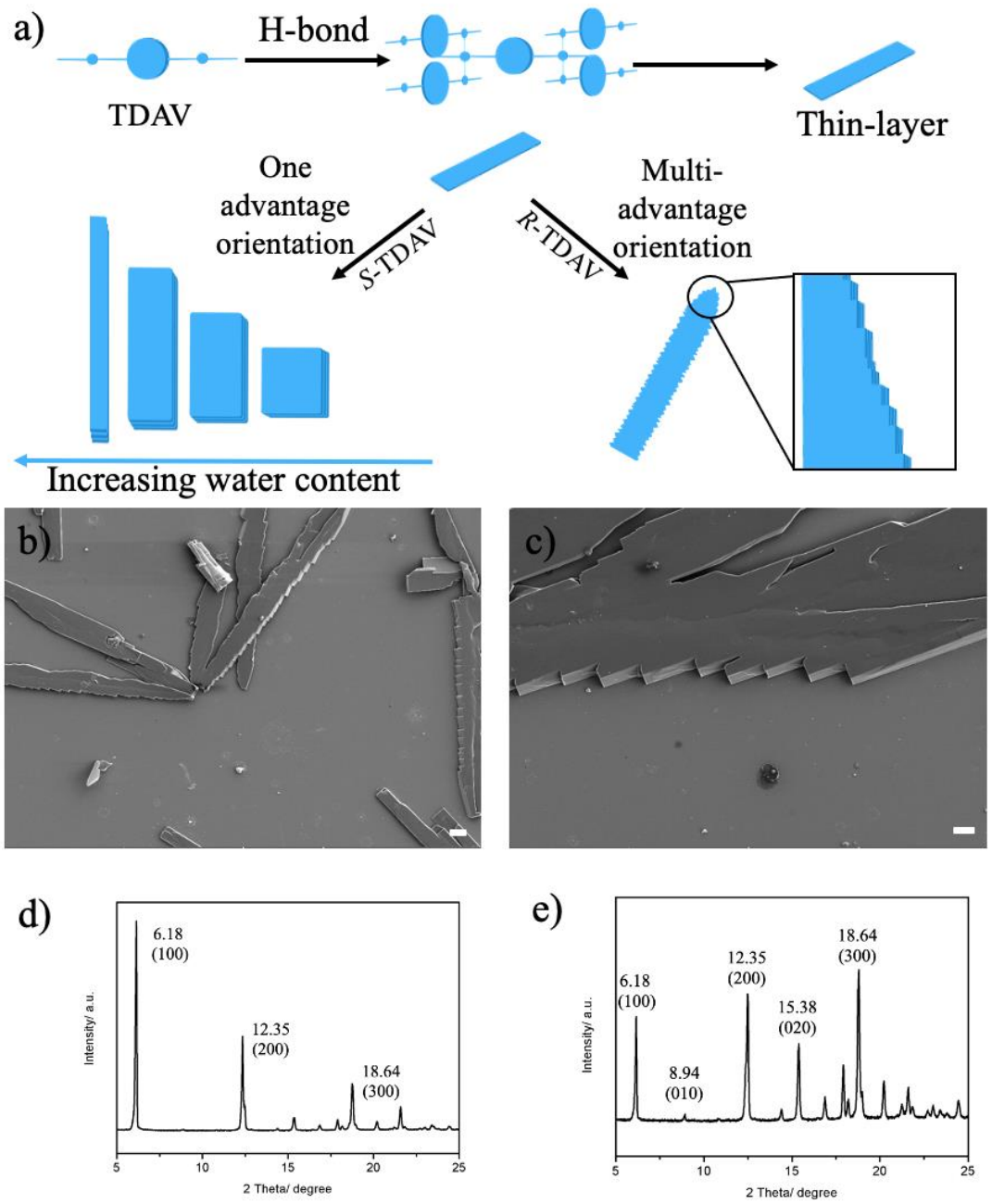

Figure 5.3 (a) Schematic illustration of the formation of microsheets and microsaws. (b, c) SEM images of different micelles prepared from *R*-TDAV at 0.5 mg ml^{-1} cosolvent of methanol/H_2O (1:1). Scale bars in SEM photos are 10 μm. (d, e) XRD patterns of *S*-TDAV and *R*-TDAV.

In order to elucidate the formation of these different microstructures based on the difference of chirality, powder X-ray diffraction (XRD) was carried out for TDAV enantiomers as shown in

Figure 5.3d and e. The diffraction of *S*-TDAV showed highly crystalline with distinct sharp peaks and high intensity. The diffraction peaks were observed at 2θ values of 6.18°, 12.35° and 18.64°. The following d-spacing values were calculated with Bragg's equation: d= 14.3 Å. These corresponding d-spacing ratio is about 1: 2: 3, which essentially indicated a lamellar packing mode.[17] These period peaks show one advantage growth orientation leading to uniform 2D microsheets. However, in the case of *R*-TDAV, the diffraction patterns became complicated. These diffraction peaks can be divided into two types of period peaks (Figure 5.3e). 2θ values of one group peaks were observed at 6.18°, 12.35° and 18.64° with same d-spacing as enantiomer *R*-TDAV resulting in the growth tendency of 2D platelet, which was attributed to the lamellar packing mode. The other type of diffraction peaks was observed at 8.94° and 15.38°, whose corresponding distances were calculated as 9.89 Å. Compared with the enantiomer, *R*-TDAV had two kinds of advantage growth orientations. In the assembly progress, building block could be assembled in these two advantage growth orientations and the cooperation of these different assembled tendency resulted in the molecular aggregation in a ladder way. In addition, the inconsistent growth rates in the two orientations could cause the worse uniformity than the rectangular micelles. Thus the new morphology was obtained as microsaw with low uniformity, which was in accordance with the SEM observation. Based on the above results, the schematic diagram was proposed for the formation of a series of 2D microsheets (Figure 5.3a). During the process of assembly, adjacent molecules aggregated and become a thin layer-like structure by the H-bonds. Because of the different chirality leading to the different crystalline, these thin layer-like structures as foundation units possess one or multi- advantaged growth orientation resulting in 2D rectangular microsheets or microsaw. When using *S*-TDAV to assembly in different cosolvent or water ratio of solution, the aspect ratios of the basic thin-layer is changing, so these layers further

stacked into final microsheets with different morphology even in the same advantaged growth orientation. For the case of racemic TDAV, due to the mixture of different chirality, the growth rates in multiple directions compete with each other, so the 2D layer-like micelles is not well-defined and the shape is disordered.

5.5 Conclusions

In conclusion, amino acid derivatives TDAV consisting of central thiophene-2,5-dicarboxamide cores with enantiomeric valine methyl ester have been synthesized and employed as building blocks to fabricate various microstructures. The *S*-TDAV formed the well-defined 2D microsheets with tunable aspect ratios from rectangular to square micelles through changing the polarity of cosolvents and 1D microwire even was obtained by controlling water content. By using the enantiomer and racemic TDAV to self-assembly, the new microsaw and lay-like micelles were achieved, respectively. The molecular packing through the hydrogen bond and assembly characteristics have been confirmed by SCXRD and powder-XRD. This work expands the construction of 2D controllable supramolecular microstructures through amino acid derivatives and provided further understanding of the effect of chirality on the supramolecular architectures.

5.6 References

[1] Cai S. L.; Zhang, W. G.; Zuckermann R. N.; Li Z. T.; Zhao X.; Liu Y., The Organic Flatland—Recent Advances in Synthetic 2D Organic Layers. Adv. Mater. 2015, 27 (38), 5762-5770.

[2] Boott C. E.; Nazemi A.; Manners I., Synthetic Covalent and Non-Covalent 2D Materials. Angew. Chem. Int. Ed. 2015, 54 (47), 13876-13894.

[3] Zhang J.; Qi, S.; Zhang C.; Wang W.; Ding Q.; Zhang H.; Dong, Z., Supramolecular 2D monolayered nanosheets constructed by using synergy of non-covalent interactions. Chem. Commun. 2021, 57 (51), 6272-6275.

[4] Ishiba K.; Noguchi T.; Iguchi H.; Morikawa, M..; Kaneko K.; Kimizuka N., Photoresponsive Nanosheets of Polyoxometalates Formed by Controlled Self-Assembly Pathways. Angew. Chem. Int. Ed. 2017, 56 (11), 2974-2978.

[5] Sakai F.; Yang G.; Weiss M. S.; Liu Y.; Chen G.; Jiang M., Protein crystalline frameworks with controllable interpenetration directed by dual supramolecular interactions. Nat. Commun. 2014, 5 (1), 4634.

[6] Li H.; Han L.; Zhu,Y.; Fernández-Trillo P.; He F., Transformation from rod-like to diamond-like micelles by thermally induced nucleation self-assembly. Macromolecules 2021, 54 (11), 5278-5285.

[7] Han L.; Wang M.; Jia X.; Chen W.; Qian H.; He F., Uniform two-dimensional square assemblies from conjugated block copolymers driven by π–π interactions with controllable sizes. Nat. Commun. 2018, 9 (1), 865.

[8] Qi R.; Zhu Y.; Han L.; Wang M.; He F., Rectangular platelet micelles with controlled aspect ratio by hierarchical self-assembly of poly(3-hexylthiophene)-b-poly(ethylene glycol). Macromolecules 2020, 53 (15), 6555-6565.

[9] Ganda S.; Dulle M.; Drechsler M.; Förster B.; Förster S.; Stenzel M. H., Two-dimensional self-assembled structures of highly ordered bioactive crystalline-based block copolymers. Macromolecules 2017, 50 (21), 8544-8553.

[10] Zhong Y.; Wang Z.; Zhang R.; Bai F.; Wu H.; Haddad R.; Fan H., Interfacial self-assembly driven formation of hierarchically structured nanocrystals with photocatalytic activity. ACS Nano 2014, 8 (1), 827-833.

[11] Han L.; Fan H.; Zhu Y.; Wang M.; Pan F.; Yu D.; Zhao Y.; He F., Precisely controlled two-dimensional rhombic copolymer micelles for sensitive flexible tunneling devices. CCS Chem.

2021, 3 (5), 1399-1409.

[12] Baek K.; Yun G.; Kim Y.; Kim D.; Hota R.; Hwang I.; Xu D.; Ko Y. H.; Gu G. H.; Suh J. H.; Park C. G.; Sung B. J.; Kim, K., Free-standing, single-monomer-thick two-dimensional polymers through covalent self-assembly in solution. J. Am. Chem. Soc. 2013, 135 (17), 6523-6528.

[13] Wei G.; Su Z.; Reynolds N. P.; Arosio P.; Hamley I. W.; Gazit,E.; Mezzenga R., Self-assembling peptide and protein amyloids: from structure to tailored function in nanotechnology. Chem. Soc. Rev. 2017, 46 (15), 4661-4708.

[14] Qin M.; Li Y.; Zhang Y.; Xing C.; Zhao C.; Dou X.; Zhang Z.; Feng C., Solvent-Controlled Topological Evolution from Nanospheres to Superhelices. Small 2020, 16 (47), 2004756.

[15] Nicks J.; Boer S. A.; White N. G.; Foster J. A., Monolayer nanosheets formed by liquid exfoliation of charge-assisted hydrogen-bonded frameworks. Chem. Sci. 2021, 12 (9), 3322-3327.

[16] Li H.; Han L.; Li Q.; Lai H.; Fernández-Trillo P.; Tian L.; He F., Hierarchical chiral supramolecular nanoarchitectonics with molecular detection: helical structure controls upon self-assembly and coassembly. Macromol. Rapid Commun. 2100690.

[17] Sang Y.; Duan P.; Liu M., Nanotrumpets and circularly polarized luminescent nanotwists hierarchically self-assembled from an achiral C_3-symmetric ester. Chem. Commun. 2018, 54 (32), 4025-4028.

CHAPTER 6 SUMMARY AND CONCLUSIONS

In this thesis, we investigated the versatility of the hierarchical self-assembly using block copolymers and amino acid derivates in order to construct various 2D platelet micelles with controllable morphology and chiral supramolecular architectures. Based on PPV-*b*-P2VP BCPs with conjugated backbones and bottom-up assembly, by the introduction of chlorine or TIPS group, we achieved the 2D morphological transformation and transition and deeply studied the growth process and energetics. In addition, we also obtained the chiral supramolecules with tunable handedness for biologic applications.

In the second chapter, based on the Siegrist poly-condensation, the $(PPV\text{-}Cl_{20\%})_{10}$-*b*-$P2VP_{20}$ was designed and synthesized for novel nanostructures. By self-assembly, 1D rod-like micelles with precise control on their scales were obtained by changing the concentrations. Then we created the thermally induced nucleation assembly approach of sonication and heating treatment, achieving morphological transformation from rod-like micelles to 2D diamond-like micelles. The scales of the 2D diamond-like micelles could be precisely controlled by adjustment of the annealing temperature. In addition, the sizes of the diamond micelles could be also effectively tuned by controlling the unimer-to-seed ratio.

Having achieved morphological transformation between different dimensions by increasing intermolecular interactions, we continued to explore the effect of introduced crystalline of the building block as PPV-*b*-P2VP on the assembled process and the

obtained micelles. In Chapter 3, we designed and synthesized a new PPV-based copolymer containing bulkier TIPS side chain with a corona block of P2VP as the building unit. A series of 2D rectangular nanosheets were established, whose scales and shapes were controlled by regulating the concentrations and the ratios of PPV and P2VP. Based on the result, the heterogenous co-assembly by using PPV-TIPS and PPV-EH based BCPs was achieved through the balance of π−π interactions and crystalline force between Si-Si, resulting in new circular disk-like micelles.

The fourth and fifth chapter presents the design and synthesis of building blocks based on amino acid derivatives for different supramolecular assembly systems with potential applications. First, we synthesized the thiophene-2,5-dicarboxamide with phenylalanine methyl ester (TDAP) and valine methyl ester branches (TDAV). In the fourth chapter, the morphology transformation from spherical micelles to twisted fibers with controllable handedness was achieved by TDAP, and racemic microsheets were produced by co-assembly with enantiomeric TDAP. In addition, the *R*-TDAP was engineered as *R*-TDAP-COOH and we explored the biological application of *R*-TDAP-COOH by utilizing co-assembly with MA through supramolecular interactions. Melamine (MA) can be detected by explicit morphology transformation including the appearance and inversion of helicity. In the fifth chapter, we employed *R*-TDAV to form the well-defined 2D supramolecular microsheets with tunable aspect ratios from rectangular to square micelles through changing the polarity of cosolvents or controlling water content. By

using the enantiomer and racemic TDAV for self-assembly, the new microsaw and lay-like micelles were also achieved.

In summary, these above results and conclusions provided approaches to fabricating 2D hierarchical supramolecular platelet micelles with controllable morphology and chiral architectures based on BCPs or amino acid derivates, which could be potential materials for biological and optoelectronics applications.

APPENDIX A Supplementary information for chapter 2

A.1 Supplementary data

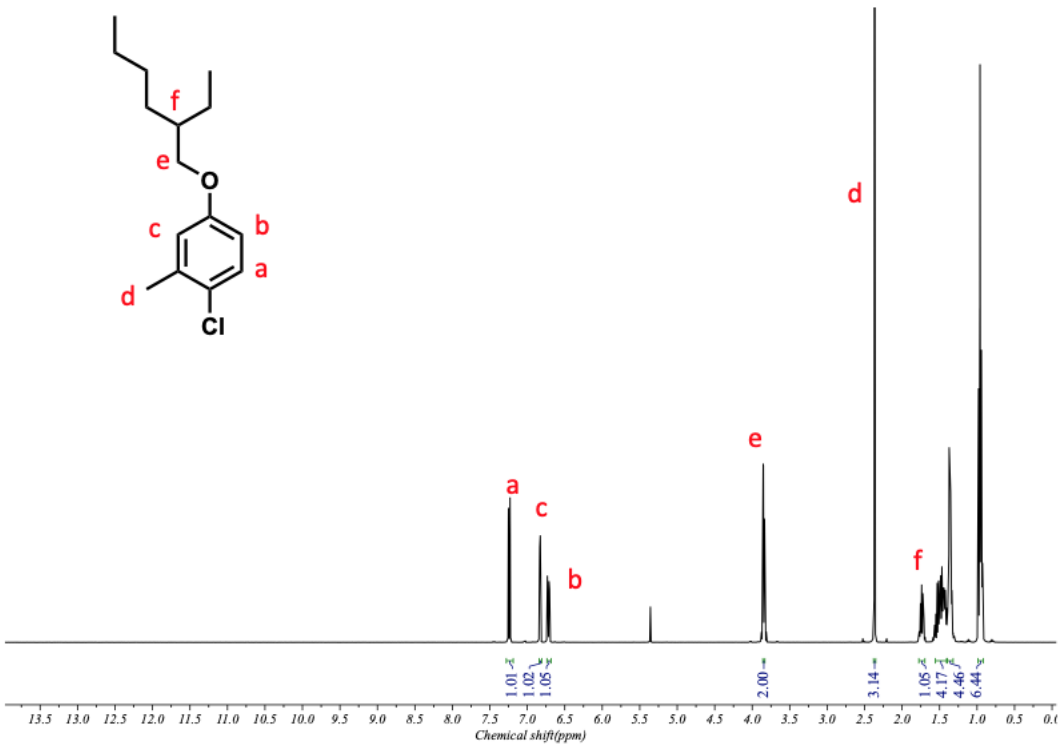

Figure A.1. ^{1}H NMR spectrum of 1-chloro-4-((2-ethylhexyl) oxy)-2-methylbenzene in CD_2Cl_2.

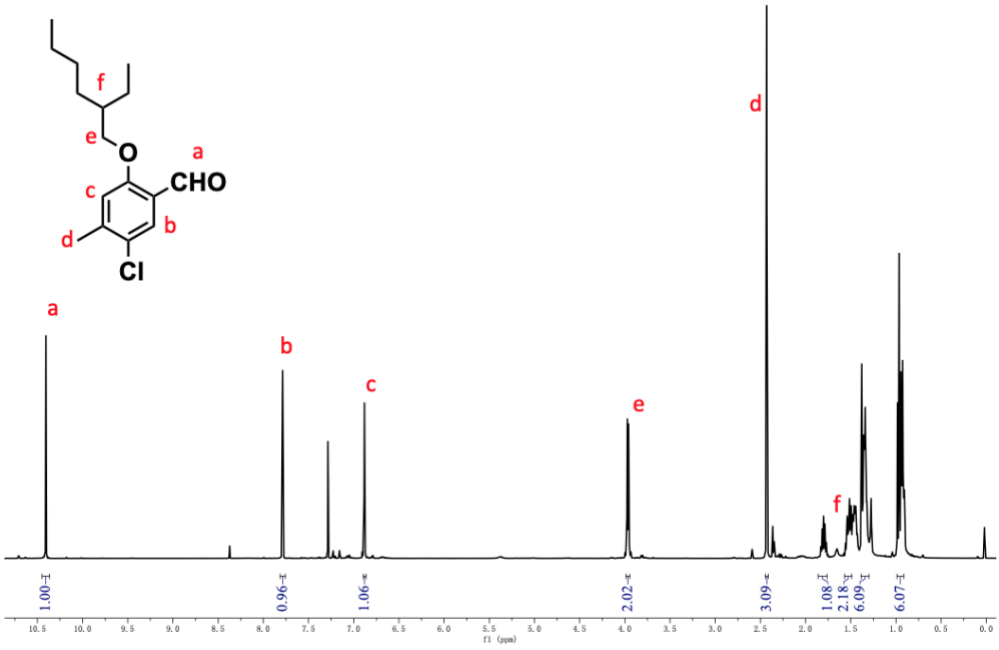

Figure A.2. ^{1}H NMR spectrum of 5-chloro-2-((2-ethylhexyl) oxy)-4-methylbenzaldehyde in $CDCl_3$.

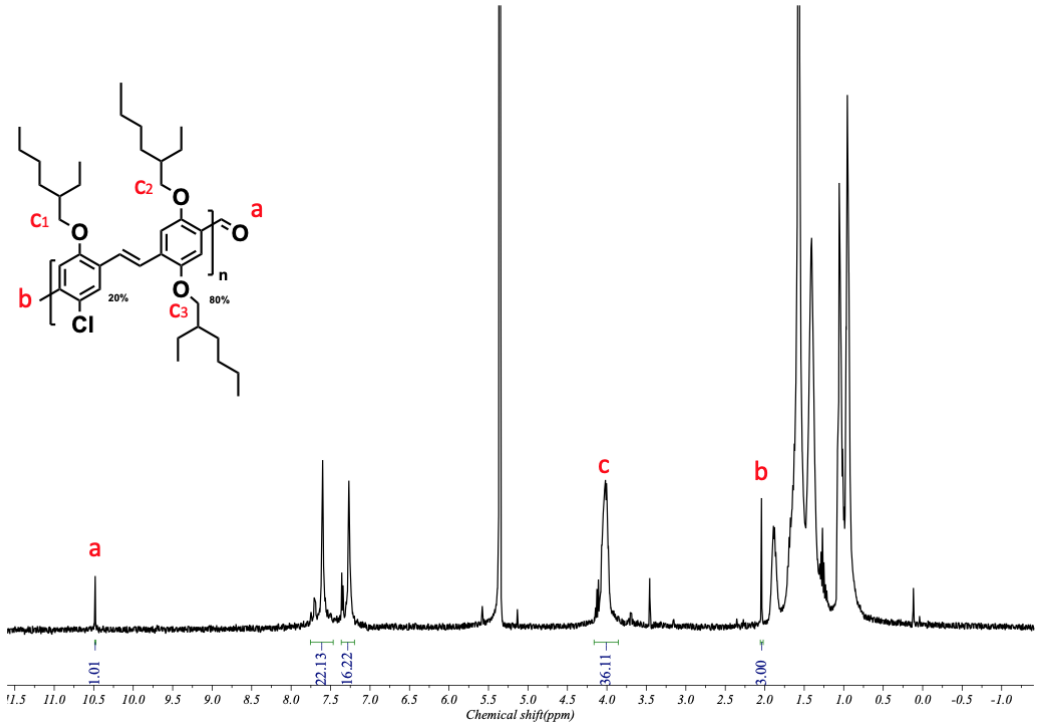

Figure A.3 ^{1}H NMR spectrum of (PPV-Cl$_{20\%}$)$_{10}$-CHO in CD_2Cl_2.

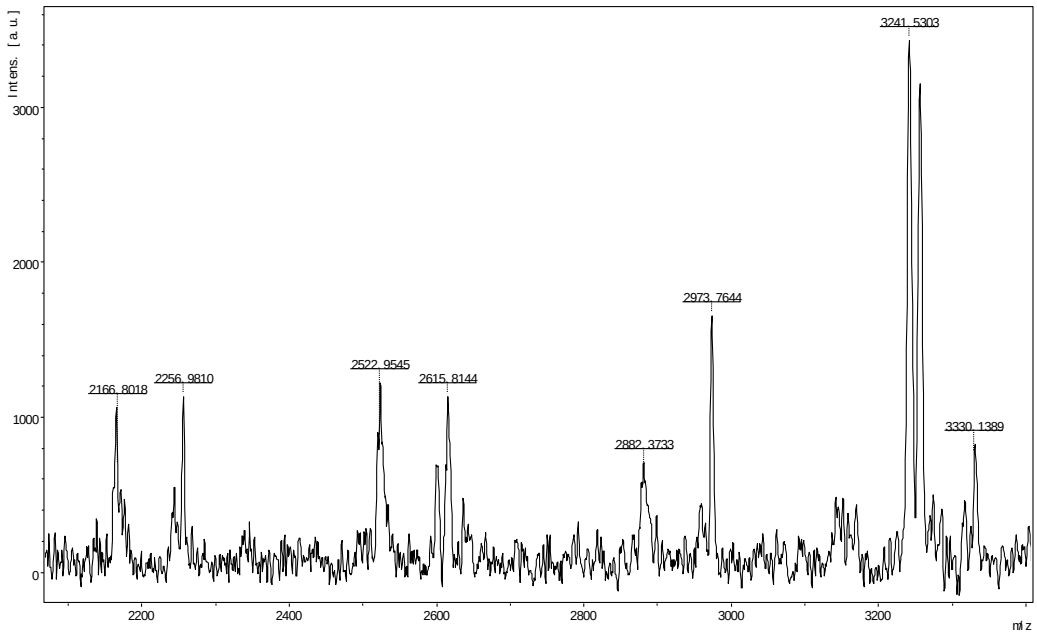

Figure A.4 MALDI-TOF mass spectrum of (PPV-Cl$_{20\%}$)$_{10}$-CHO. The EH-PPV repeat unit is 358.2 m/z and molecular weight difference of EH-PPV unit and PPV-Cl unit is 94 m/z.

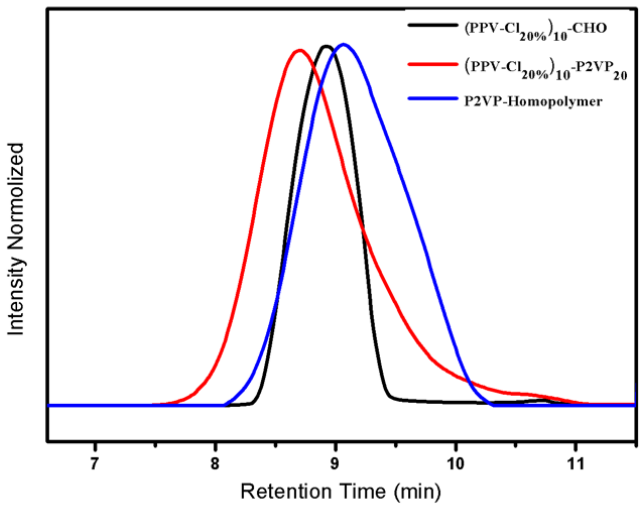

Figure A.5. GPC traces (UV-Vis) of (PPV-Cl$_{20\%}$)$_{10}$-CHO, P2VP homopolymer and (PPV-Cl$_{20\%}$)$_{10}$-*b*-P2VP$_{20}$.

Table. A.2. GPC data of the (PPV-$Cl_{20\%}$)$_{10}$-CHO, P2VP and (PPV-$Cl_{20\%}$)$_{10}$-*b*-P2VP$_{20}$.

BCP	M_n	M_w	DPI
(PPV-$Cl_{20\%}$)$_{10}$-CHO	3400	3740	1.10
P2VP	2100	2373	1.13
(PPV-$Cl_{20\%}$)$_{10}$-*b*-P2VP$_{20}$	5577	6358	1.14

Table A.3. Summary of the data of the length of the 1D rod-like micelles.

Concentration (mg ml^{-1})	L_n[a] (nm)	L_w (nm)	$Đ$ (L_n / L_w)
0.01	6971	7528	1.08
0.005	3715	4161	1.12
0.001	1833	1929	1.05

[a]100 1D rod-like micelles from TEM images were traced by hand.

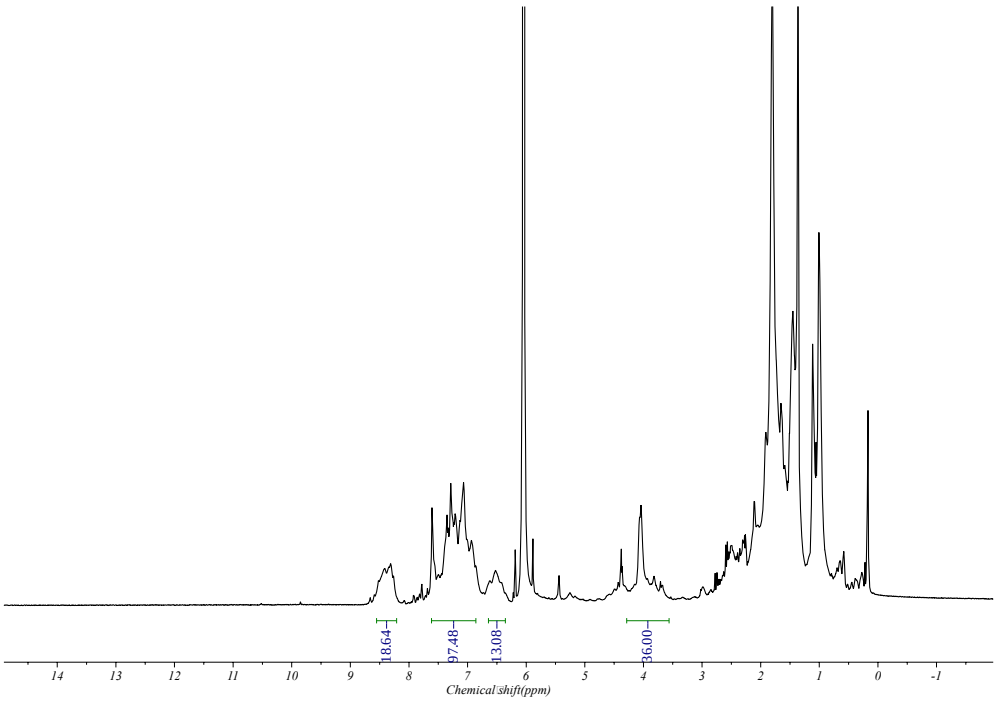

Figure A.6. ^{1}H NMR spectrum of (PPV-$Cl_{20\%}$)$_{10}$-*b*-P2VP$_{20}$ in $C_2D_2Cl_4$.

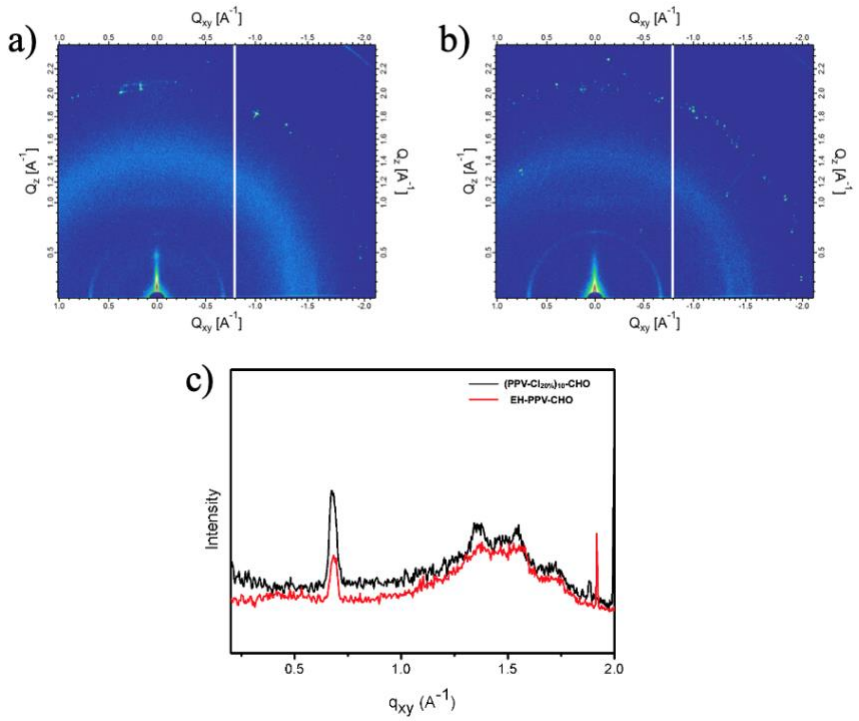

Figure. A.7. 2D GIWAXS patterns of **a.** $(PPV\text{-}Cl_{20\%})_{10}$-CHO and **b.** EH-PPV-CHO. **c.** GIWAXS profiles along the in-plane direction of $(PPV\text{-}Cl_{20\%})_{10}$-CHO and EH-PPV-CHO.

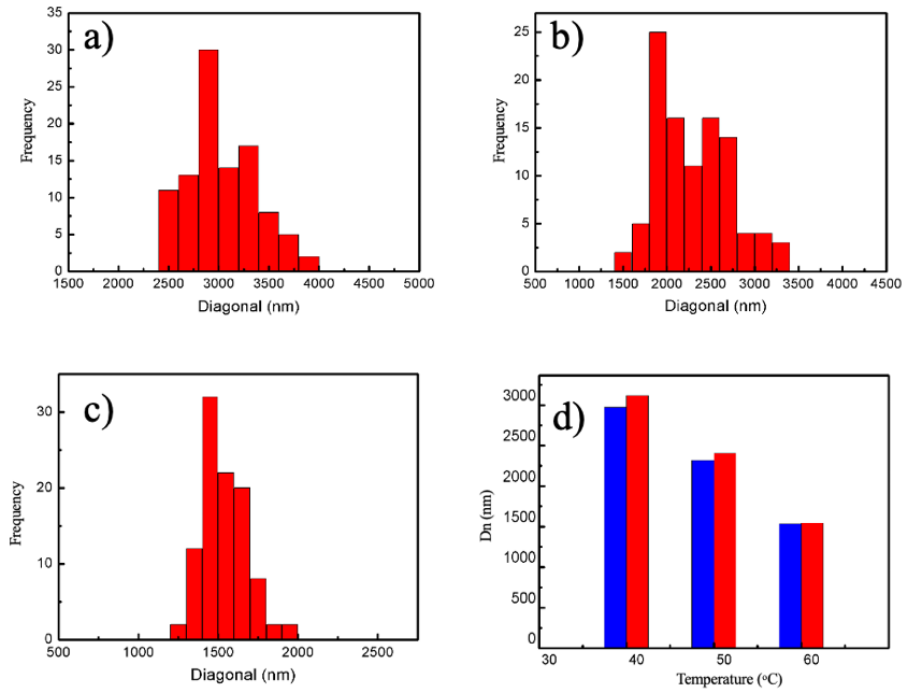

Figure A.8 a. b. c. contour length distributions of the diagonal length of correspondent 2-D diamond micelles formed at 40 °C, 50 °C and 60 °C; **d.** D_{ln} and D_{lw} of diamond micelles formed at 40 °C, 50 °C and 60 °C (Blue represent D_{ln} and red represent D_{lw}).

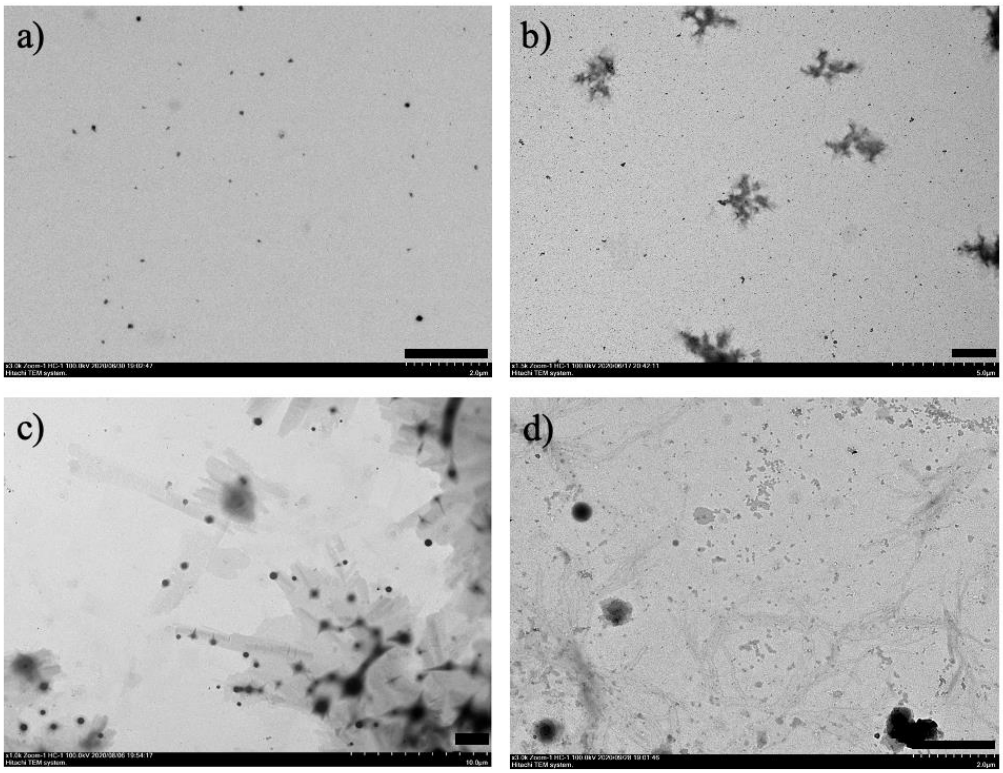

Figure A.9. TEM images of the seed micelles and the comparison experiment results. **a.** TEM images of seed micelles consist of (PPV-$Cl_{20\%}$)$_{10}$-*b*-P2VP$_{20}$ in iso-butanol after the sonication; **b.** TEM images of contrast experiment using the (PPV-$Cl_{20\%}$)$_{10}$-*b*-P2VP$_{20}$ following the same approach without adding unimers for 7 days; **c.** TEM images of aggregates of polydisperse 2D platelets with poorly defined edges formed by the addition of 10 μL of blending unimers to isobutanol at 50℃ in the absence of seed micelles; **d.** TEM images of contrast experiment using the (PPV-$Cl_{20\%}$)$_{10}$-*b*-P2VP$_{20}$ following the same SA approach without annealing for 7 days. Scale bars in the TEM images are 2 μm.

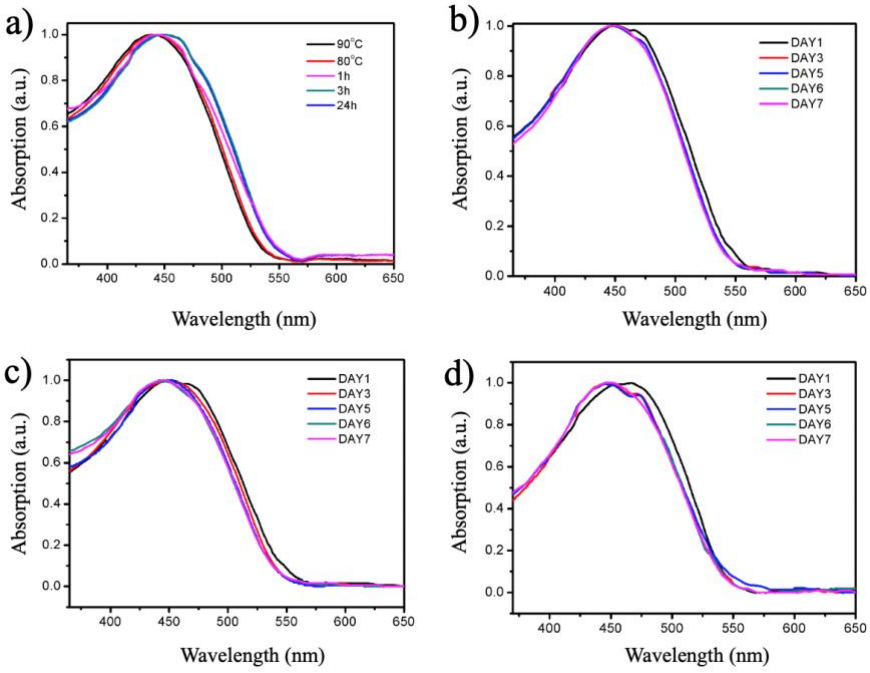

Figure A.10. UV-Vis absorption changes of **a.** 1D rod-like micelles formed from (PPV-$Cl_{20\%}$)$_{10}$-*b*-P2VP$_{20}$ in 0.01 mg ml^{-1} isobutanol solution; **b.** 2D diamond micelles formed from (PPV-$Cl_{20\%}$)$_{10}$-*b*-P2VP$_{20}$ at 40 ºC; **c.** 2D diamond micelles formed from (PPV-$Cl_{20\%}$)$_{10}$-*b*-P2VP$_{20}$ at 50 ºC; **d.** 2D diamond micelles formed from (PPV-$Cl_{20\%}$)$_{10}$-*b*-P2VP$_{20}$ at 60 ºC.

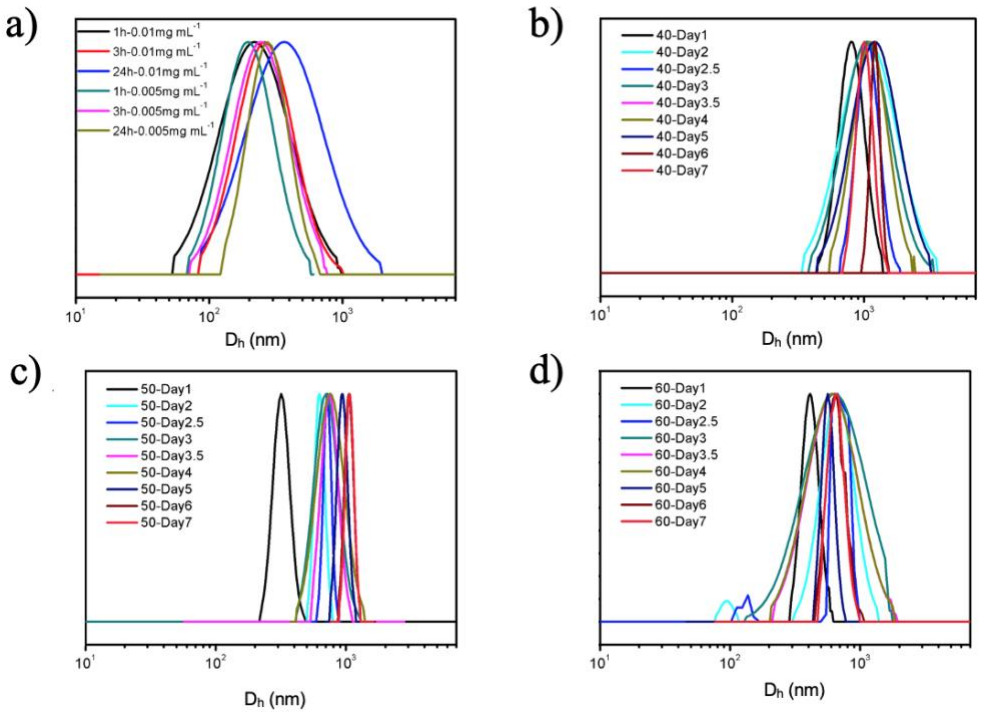

Figure. A.11. Changes of hydrodynamic diameter (D_h) of PPV-Cl in isobutanol solutions during the aging times. **a.** 1D rod-like micelles formed from $(PPV\text{-}Cl_{20\%})_{10}$-*b*-$P2VP_{20}$ in 0.01 mg ml^{-1} isobutanol solution; **b.** 2D diamond micelles formed from $(PPV\text{-}Cl_{20\%})_{10}$-*b*-$P2VP_{20}$ annealing at 40 °C; **c.** 2D diamond micelles formed from $(PPV\text{-}Cl_{20\%})_{10}$-*b*-$P2VP_{20}$ annealing at 50 °C; **d.** 2D diamond micelles formed from $(PPV\text{-}Cl_{20\%})_{10}$-*b*-$P2VP_{20}$ annealing at 60 °C.

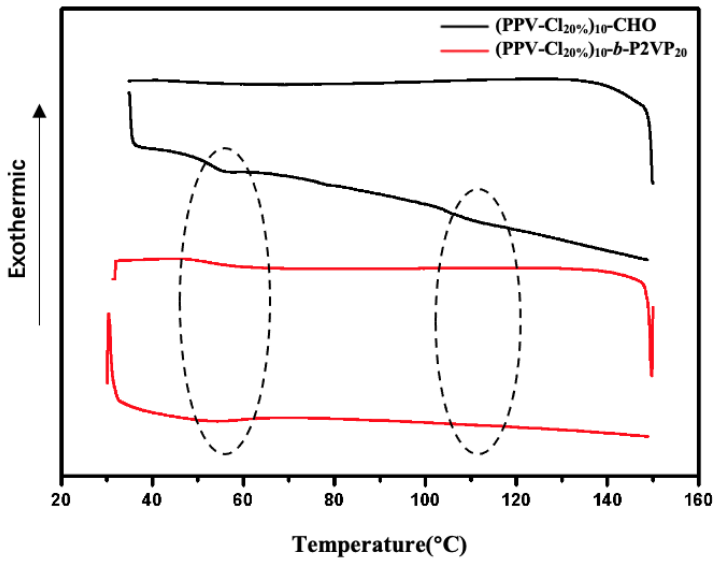

Figure. A.12 DSC curves of $(PPV\text{-}Cl_{20\%})_{10}$-CHO and $(PPV\text{-}Cl_{20\%})_{10}$-*b*-$P2VP_{20}$. The measurements were carried under N_2 at a heating rate of 10 °C min^{-1} for twice scan, and the represented curves are recorded for the second heating scan.

Table A.4 Summary of the data of the scales of the 2D diamond micelles formed at annealing 40 °C, 50 °C and 60 °C.

Temperature (°C)	D_{ln}[a] (nm)	D_{lw} (nm)	$Đ$ (D_{ln} / D_{lw})
40	2973	3118	1.05
50	2316	2406	1.04
60	1535	1548	1.01

[a]100 2D diamond-like micelles from TEM images were traced by hand.

Table. A.5 Summary of the data of the scales of the 2D diamond micelles formed from different m_{unimer}/m_{seed}.

m_{unimer}/m_{seed}	D_{ln}[a] (nm)	D_{lw} (nm)	$Đ$ (D_{ln} / D_{lw})
10	453	462	1.02
25	1535	1548	1.01
35	2306	2398	1.04
40	2805	2858	1.02

[a]100 2D diamond-like micelles from TEM images were traced by hand.

APPENDIX B Supplementary information for chapter 3

B.1 Supplementary methods

B.1.1 UV-Vis Absorption Spectra (UV-Vis)

The PL spectra were recorded by a Shimadzu RF6000 spectrofluorometer. The samples were prepared by dissolving PPV-TIPS-*b*-P2VP in isobutanol under a concentration of 0.005 mg ml^{-1} and the prepared isobutanol solutions were heated at 90 °C for 1h, cooled to room temperature (25 °C), and aged for 24 h.

B.1.2 Grazing Incidence Wide-angle X-ray Scattering (GIWAXS)

The samples were prepared by drop-coating 60 μl of the solution onto the pre-cleaned and treated silicon wafer followed by evaporating the solvent for seven times. The silicon wafers were cleaned in piranha solution for 30 min, then ultrasound successively in ethanol, ultrapure water, and finally dried with blowing nitrogen dispersed.

B.1.3 Differential scanning calorimetry

Different scanning calorimetry (DSC) measurements were performed on a Discovery series thermal analyser at a scanning rate of 10 °C min^{-1} in N_2 atmosphere. The samples were heated from 30 to 150 °C, and then cooled back to 30 °C. The thermal cycles carried on twice, and the data of second cycle were used to analyse.

B.1.4 Laser scanning confocal microscopy (LSCM).

LSCM images were performed using a ZEISS LSM 900 inverted epifluorescence microscope with a × 63 (numerical aperture1.4) oil-immersion objective lens. A drop

of sample solution of micelles was put on a cleaned slide followed sealing with a cover slip, which was prepared for observing. The samples of formed micelles in solution were excited using an argon laser operating at 405 and 488 nm and the confocal images were obtained using digital detectors with observation windows of 530–630 nm.

B.2 Supplementary data

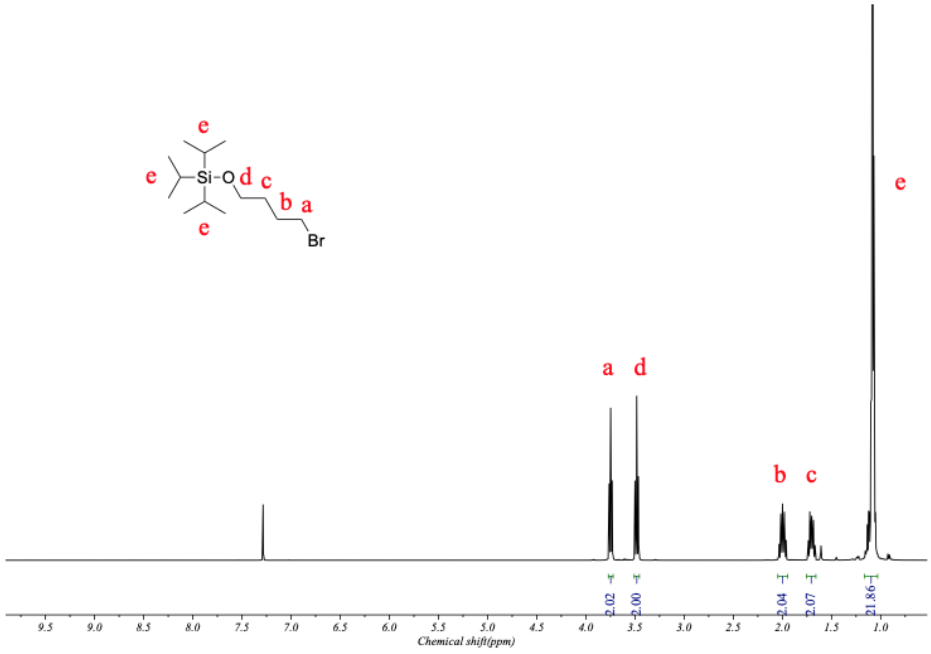

Figure B.1. ^{1}H NMR spectra of (4-bromobutoxy) triisopropylsilane in $CDCl_3$.

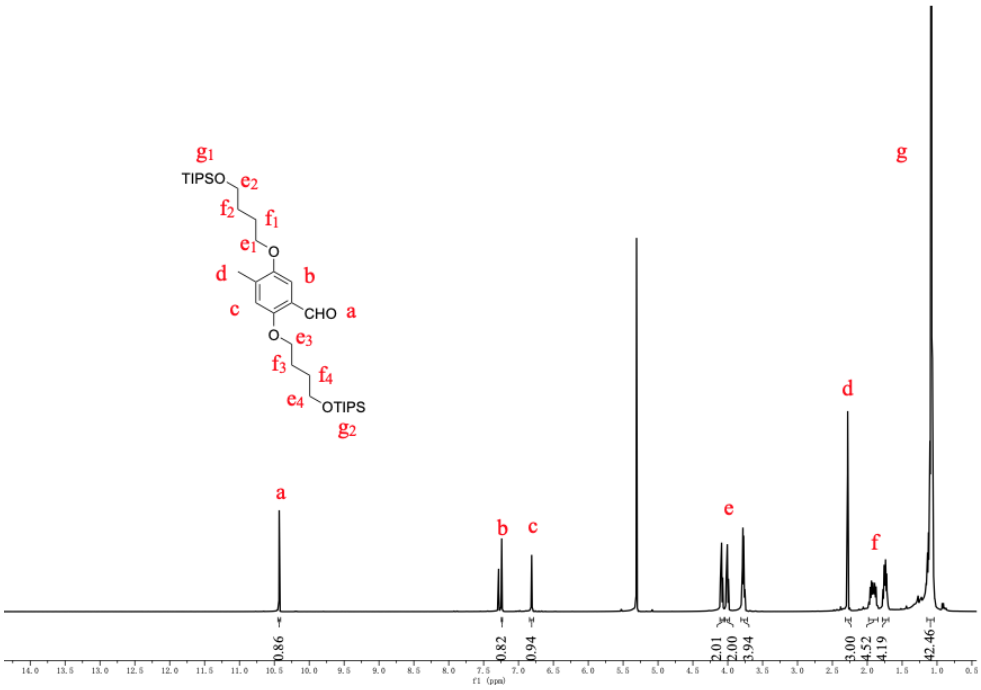

Figure B.2. ^{1}H NMR spectra of 4-methyl-2,5-bis(4-((triisopropylsilyl) oxy) butoxy) benzaldehyde in CD_2Cl_2.

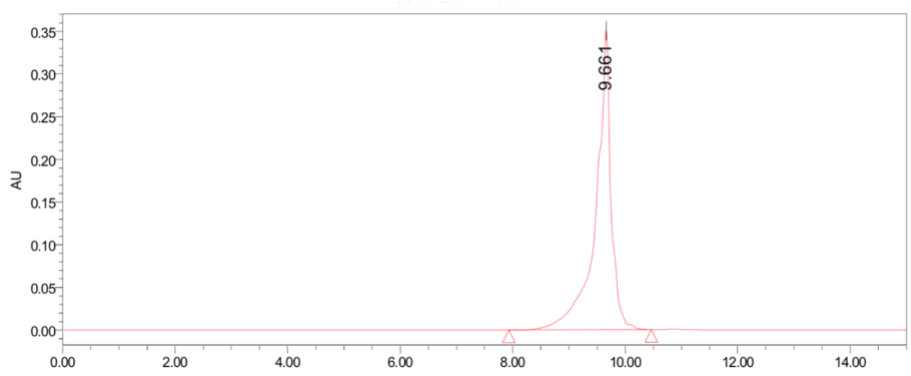

Polymers	M_n	M_w	PDI	Retention time (min)
PPV_5-TIPS-CHO	2540	2722	1.07	9.661

Figure B.3. GPC traces of PPV-TIPS-CHO.

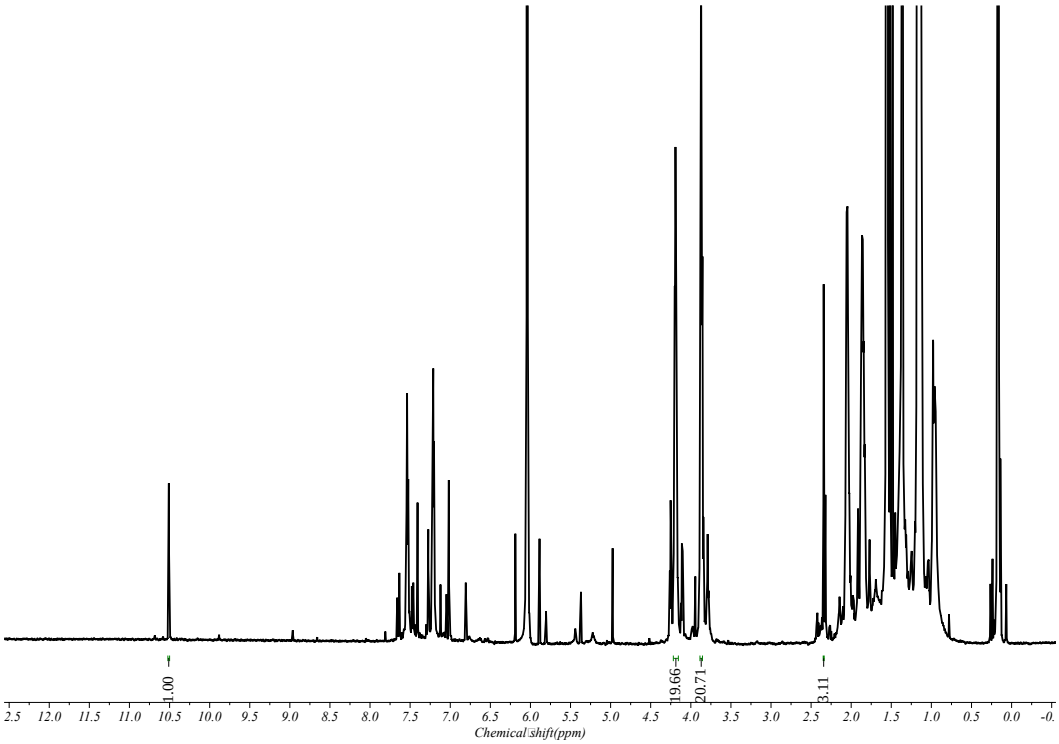

Figure B.4. ^{1}H NMR spectra of PPV_5-TIPS-CHO in $C_2D_2Cl_4$.

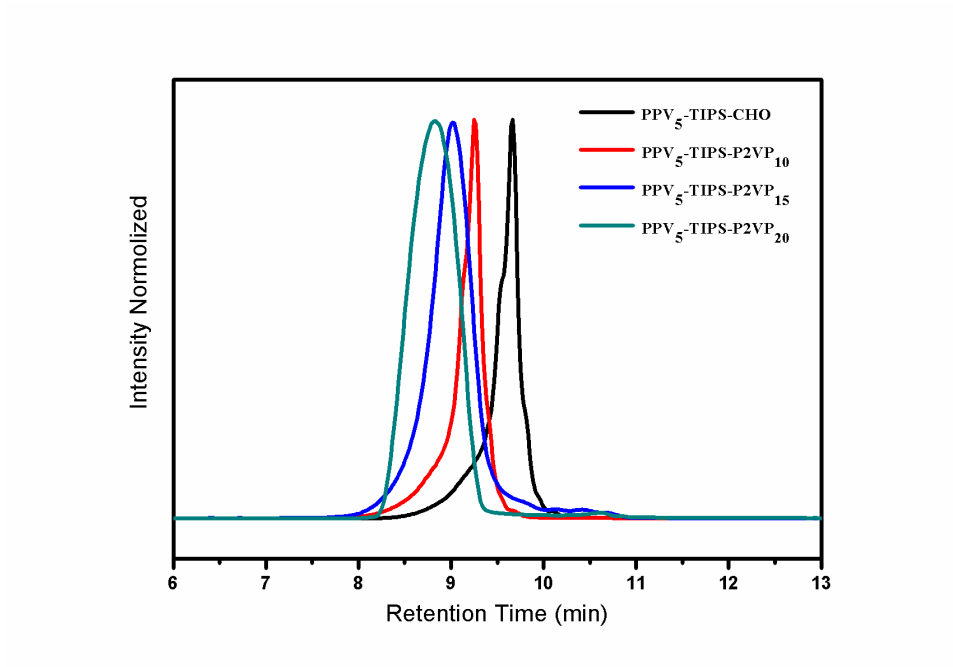

Figure B.5. GPC traces (UV-Vis) of PPV_5-TIPS-*b*-$P2VP_n$.

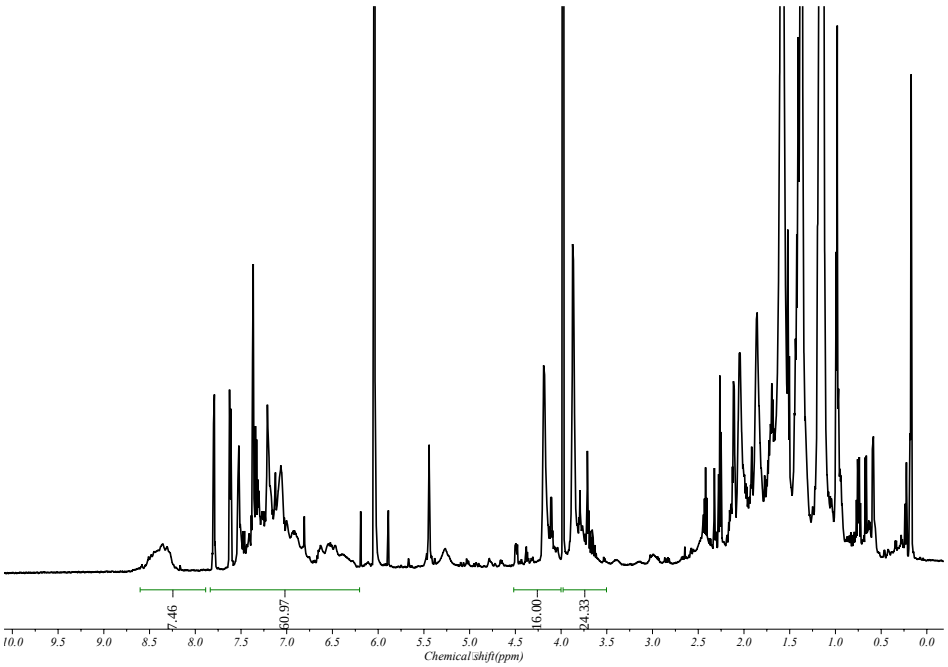

Figure B.6. ^{1}H NMR spectra of PPV_5-TIPS-*b*-$P2VP_{10}$ in $C_2D_2Cl_4$.

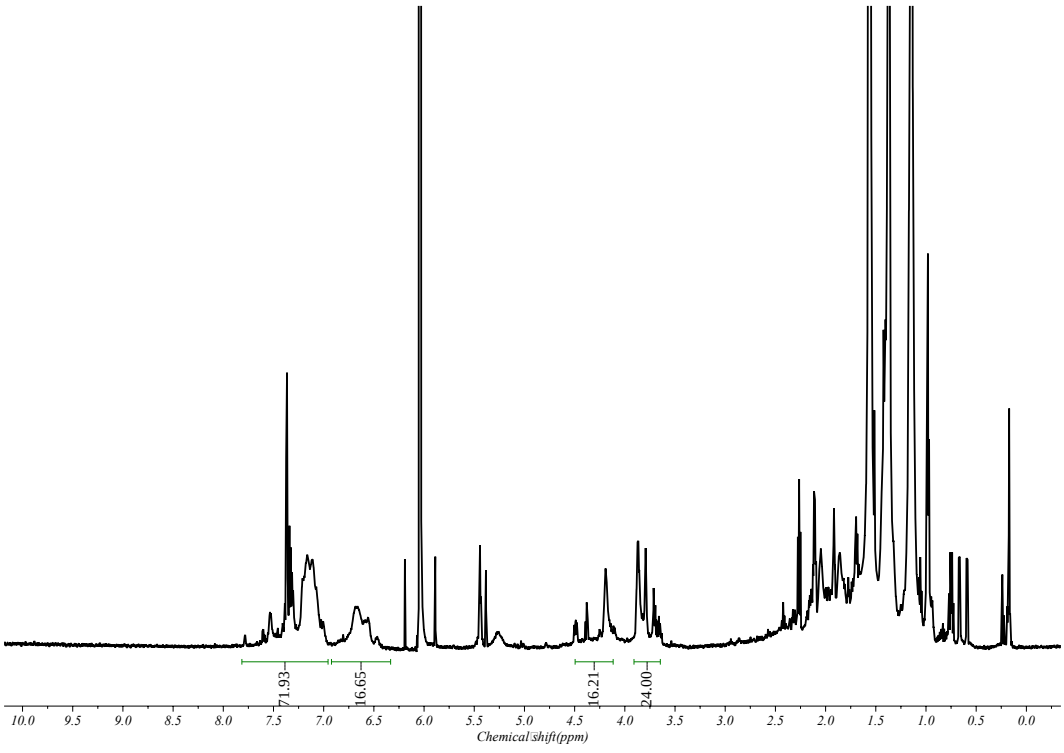

Figure B.7. ^{1}H NMR spectra of PPV_5-TIPS-*b*-$P2VP_{15}$ in $C_2D_2Cl_4$.

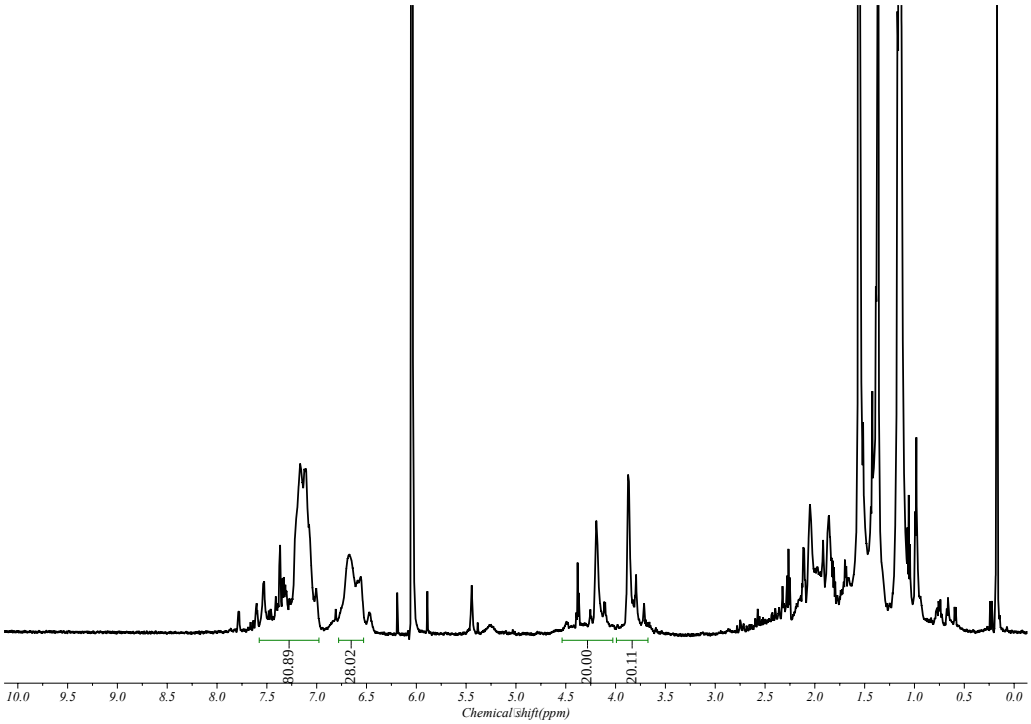

Figure B.8. ^{1}H NMR spectra of PPV_5-TIPS-*b*-$P2VP_{20}$ in $C_2D_2Cl_4$.

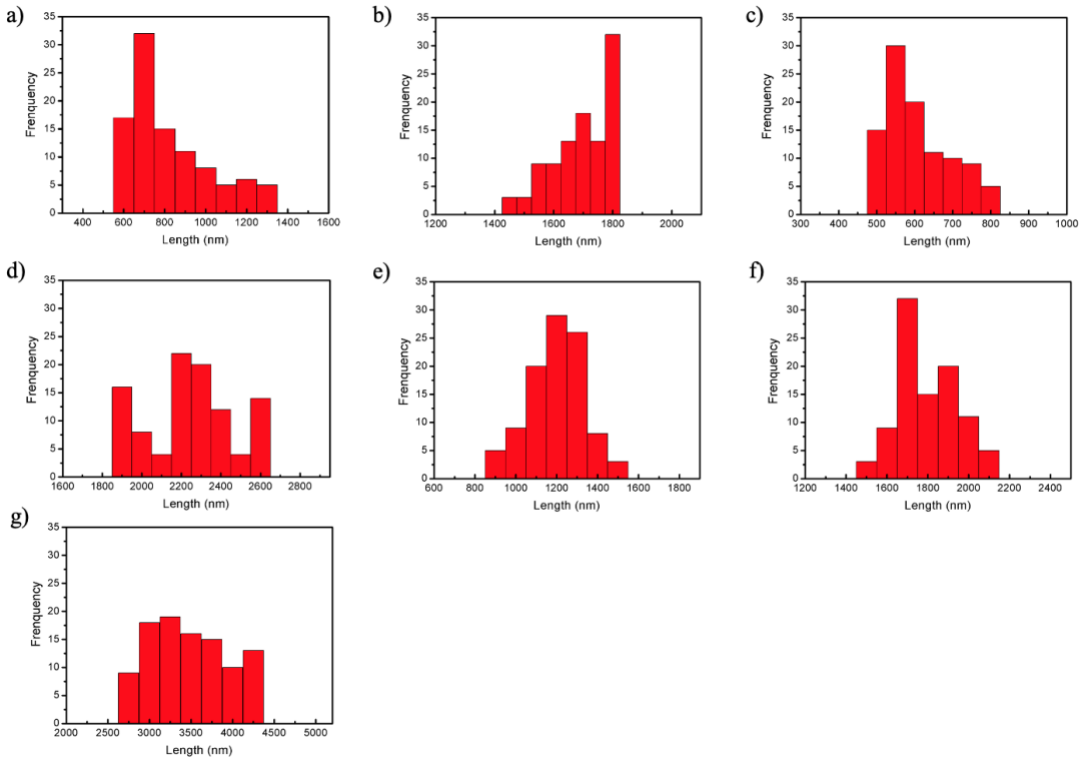

Figure B.9. contour length distributions of the number-average length of correspondent micelles formed from PPV_5-TIPS-*b*-$P2VP_n$ at different concentrations. **a. b.** PPV_5-TIPS-*b*-$P2VP_{10}$ in 0.005 and 0.01 mg ml^{-1} isobutanol solution; **c. d.** PPV_5-TIPS-*b*-$P2VP_{15}$ in 0.005 and 0.01 mg ml^{-1} isobutanol solution; **e. f. g.** PPV_5-TIPS-*b*-$P2VP_{20}$ in 0.001, 0.005 and 0.01 mg ml^{-1} isobutanol solution.

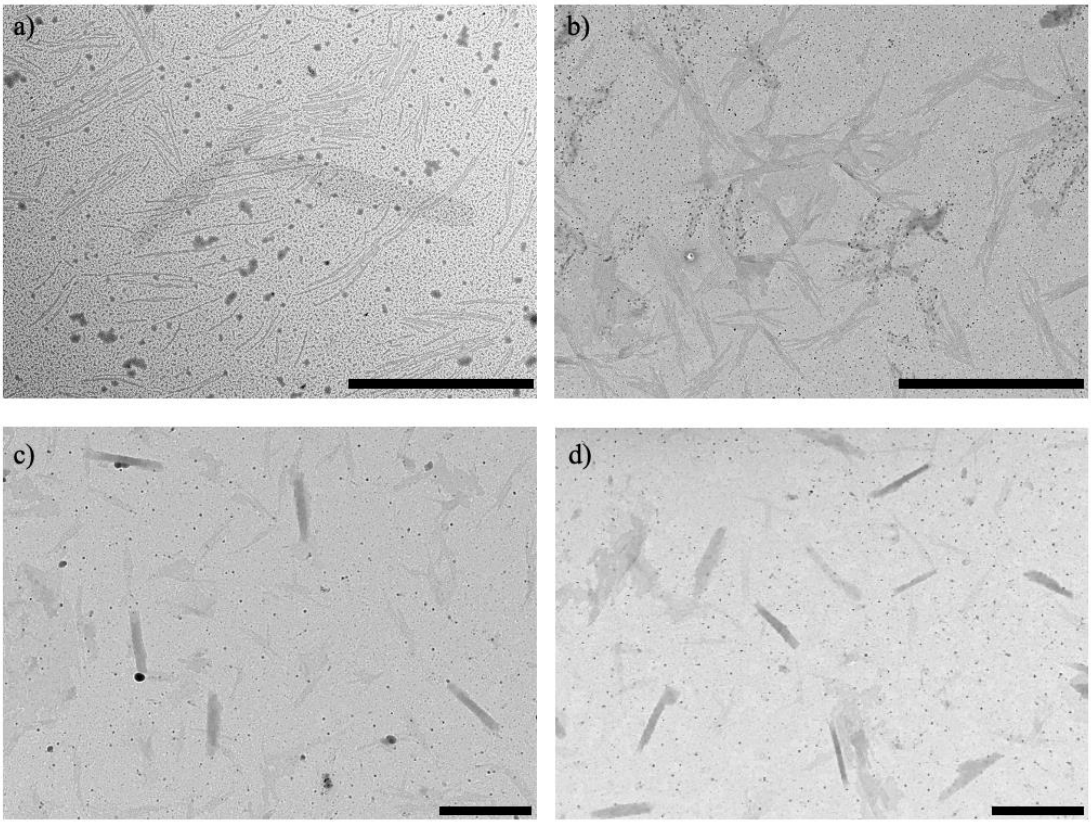

Figure B.10. TEM images of growth process of rectangular micelles formed from at 80 °C after aging for (a) 24 h; (b) 36 h; and (c, d) 48 h. Scale bars in TEM photos are 2 μm.

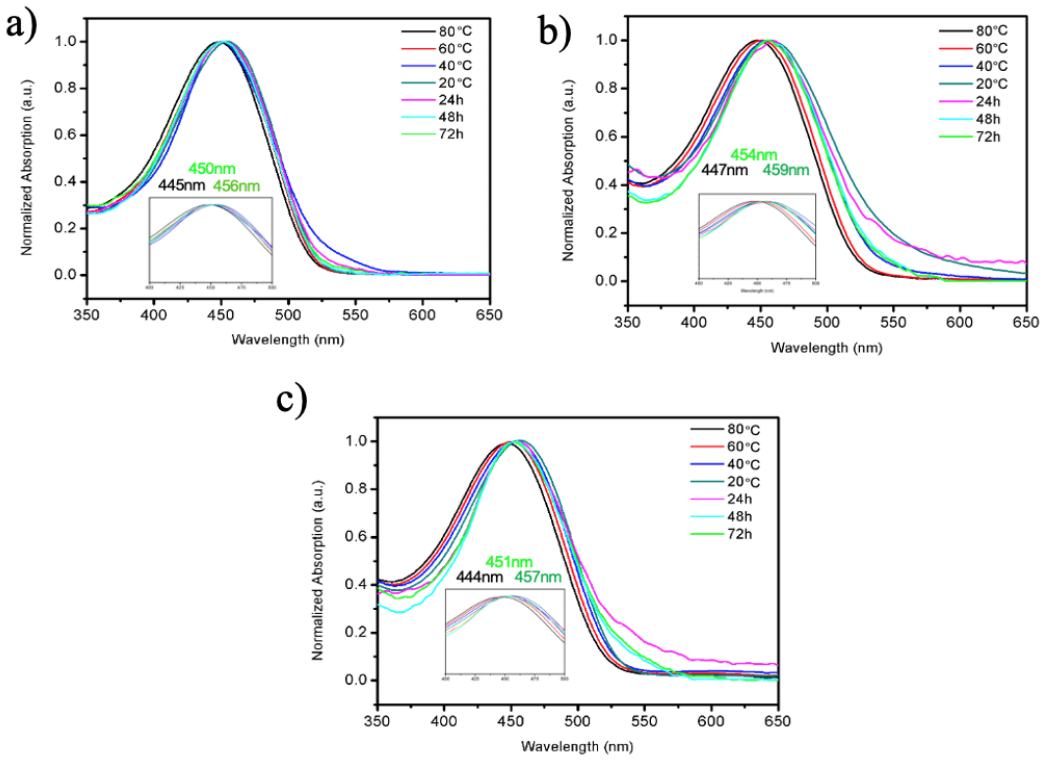

Figure B.11. UV-Vis absorption changes of 2D micelles formed from (a-c) PPV_5-TIPS-*b*-$P2VP_{10}$, PPV_5-TIPS-*b*-$P2VP_{15}$ and PPV_5-TIPS-*b*-$P2VP_{20}$ in 0.005 mg ml^{-1} isobutanol solution;

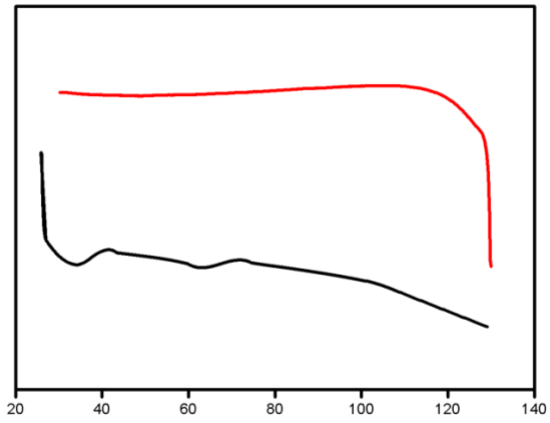

Figure B.12. DSC curves of PPV_5-TIPS-CHO. The measurements were carried under N_2 at a heating rate of 10 °C min^{-1} for twice scan, and the represented curves are recorded for the second heating scan.

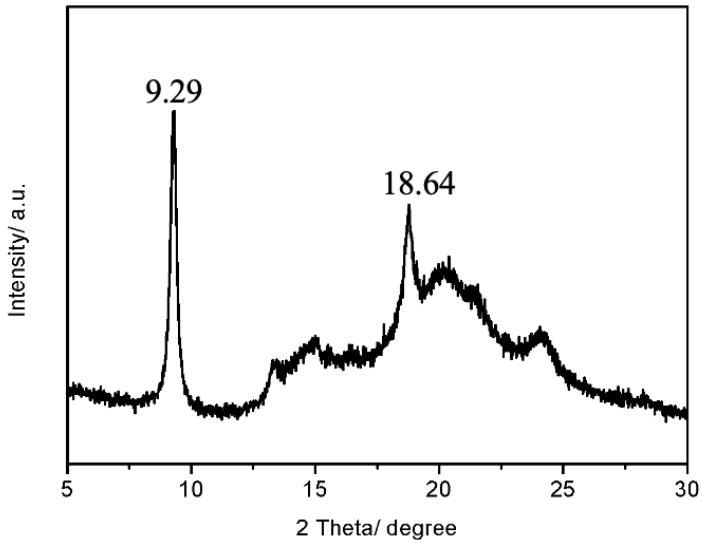

Figure B.13. XRD patterns of PPV-EH-CHO.

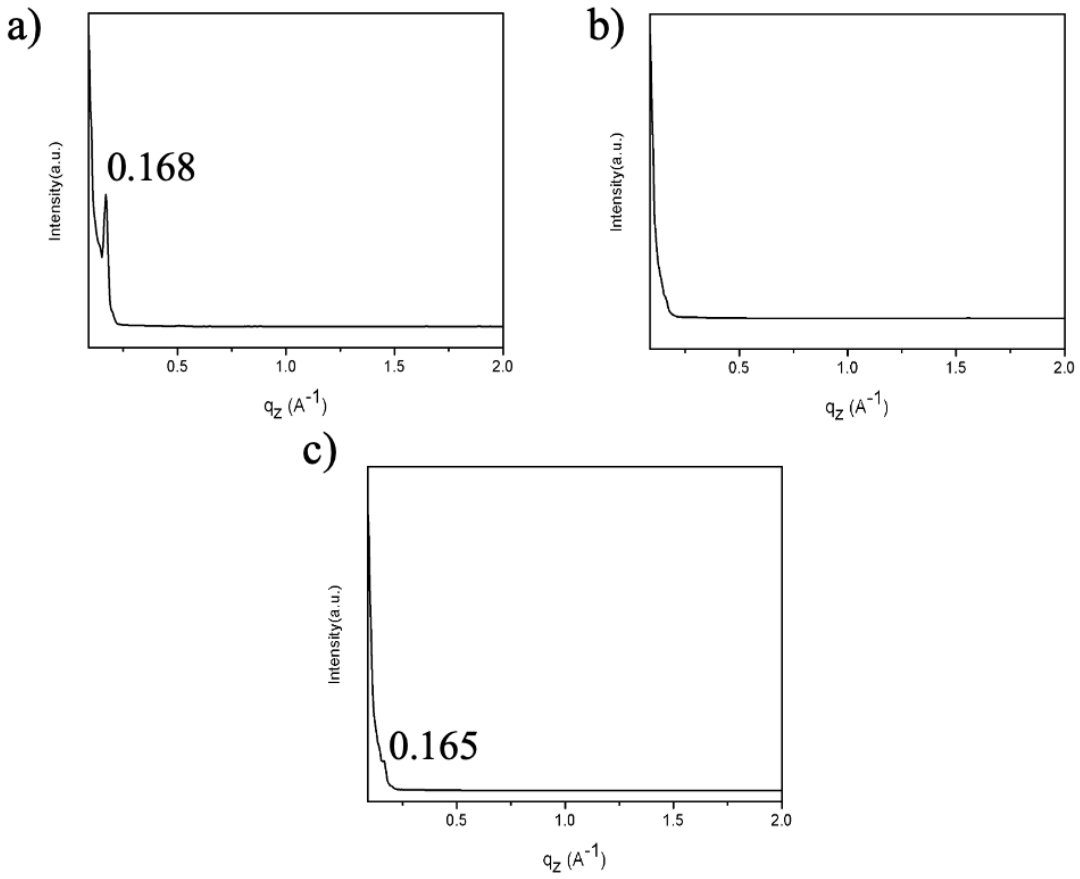

Figure B.14. GIWAXS profiles along the out-of-plane direction of platelet 2D square or rectangular micelles obtained from (a) PPV_5-TIPS-b-$P2VP_{10}$, (b) PPV_5-TIPS-b-$P2VP_{15}$ and (c) PPV_5-TIPS-b-$P2VP_{20}$.

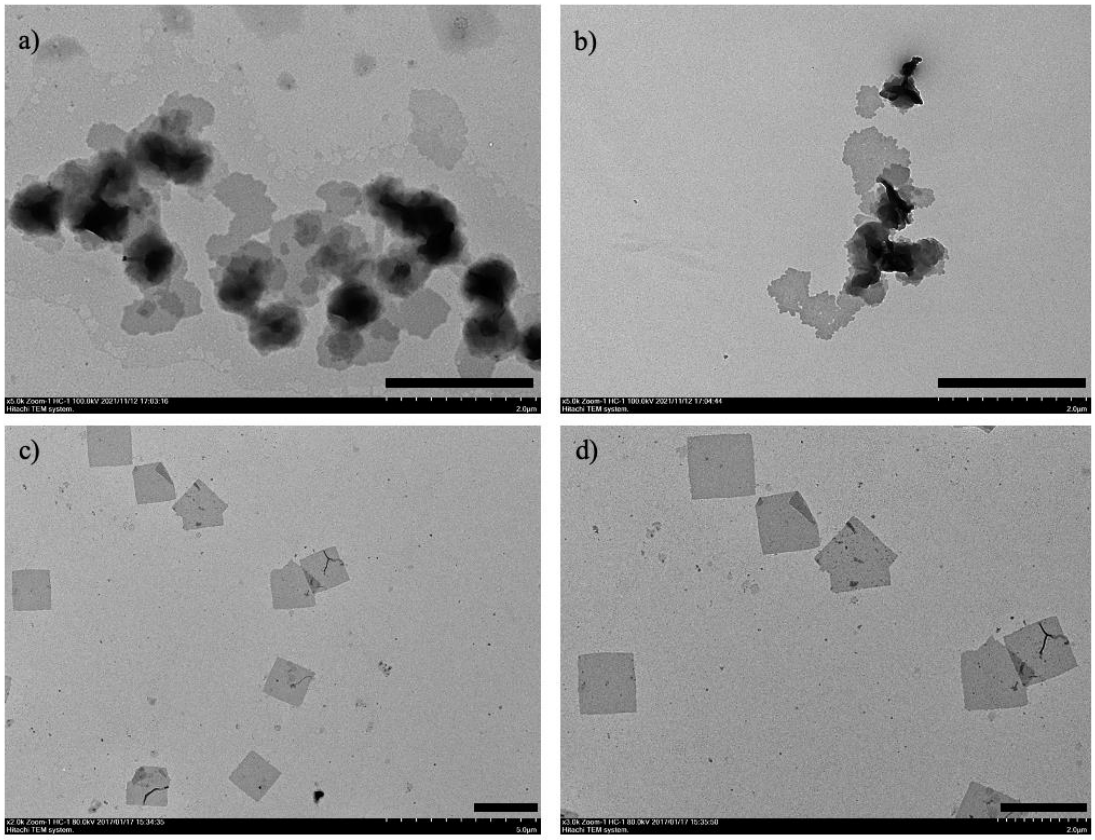

Figure B.15. TEM images of (a, b) 2D micelles based on co-assembly with PPV_{12}-*b*-$P2VP_{12}$ and PPV_5-TIPS-*b*-$P2VP_{20}$ at a 0.005 mg·ml^{-1} solution. (c, d) 2D square micelles based on assembly with PPV_{12}-*b*-$P2VP_{12}$ at a 0.005 mg·ml^{-1} solution. Scale bars in TEM photos are 2 μm.

APPENDIX C Supplementary information for chapter 4

C.1 Supplementary data

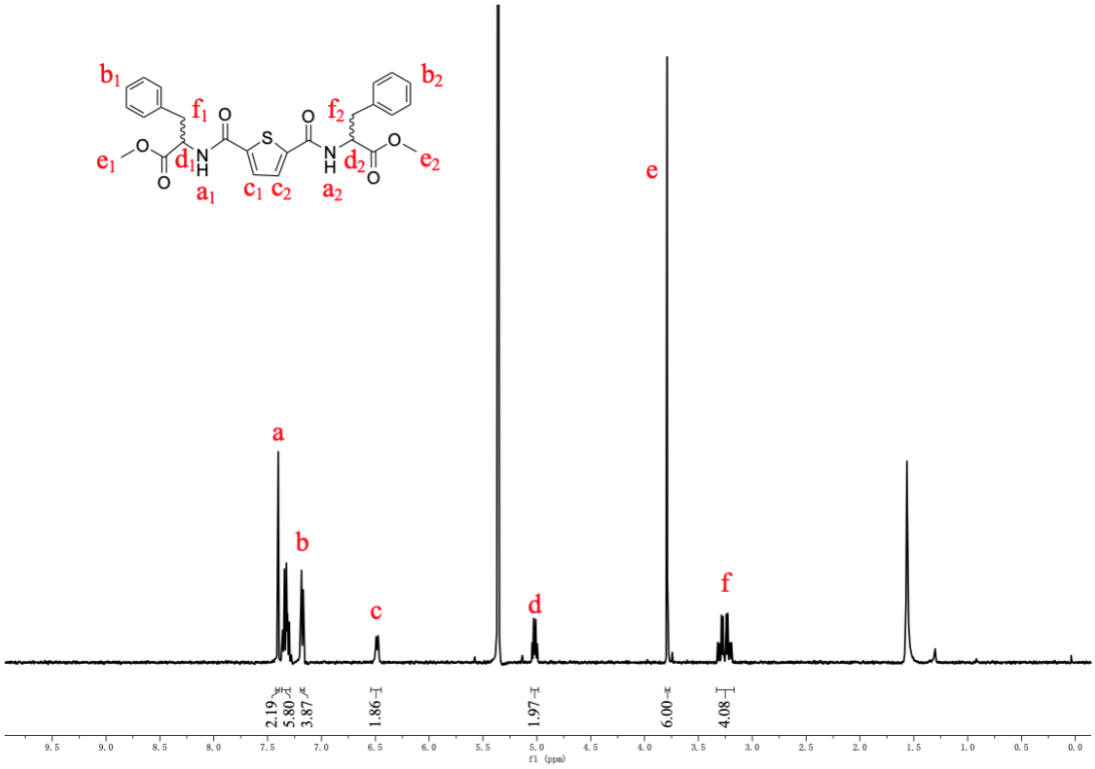

Figure C.1. ^{1}H NMR spectrum of TDAP in CD_2Cl_2.

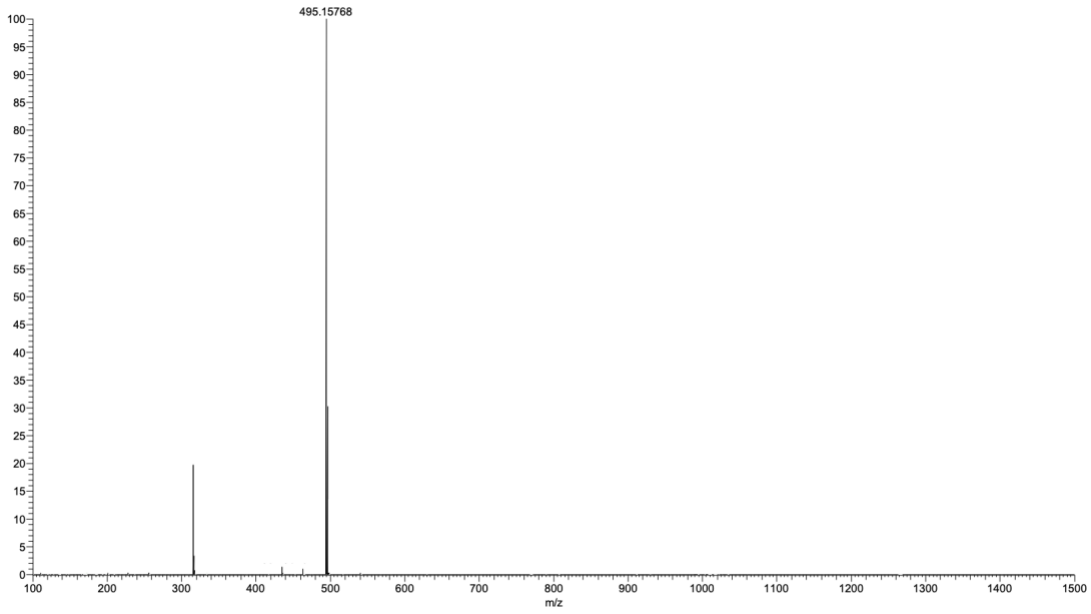

Figure C.2. Mass spectrum of *R*-TDAP.

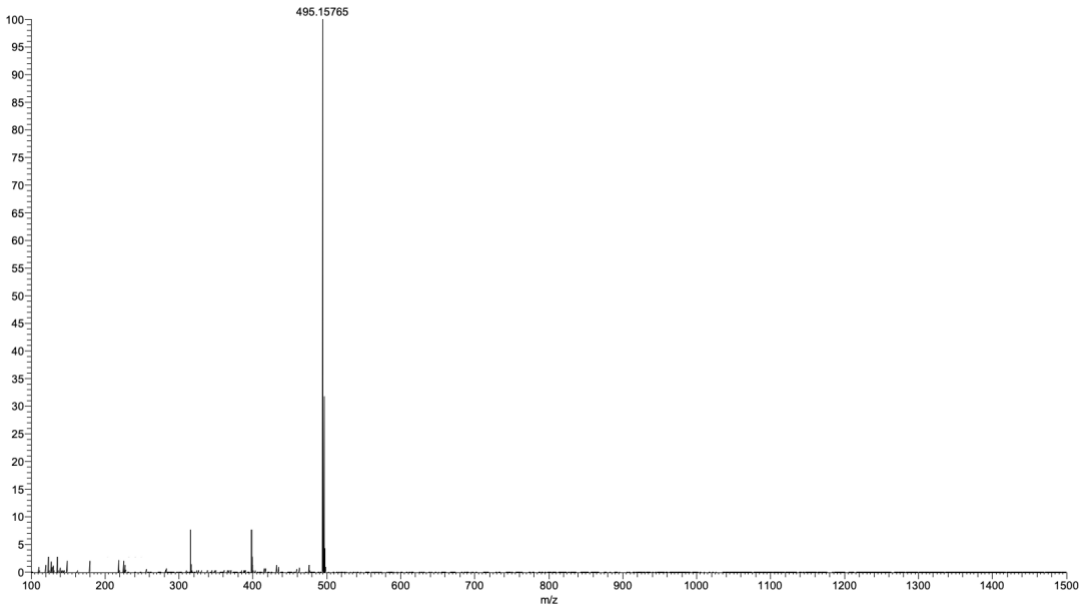

Figure C.3. Mass spectrum of *S*-TDAP.

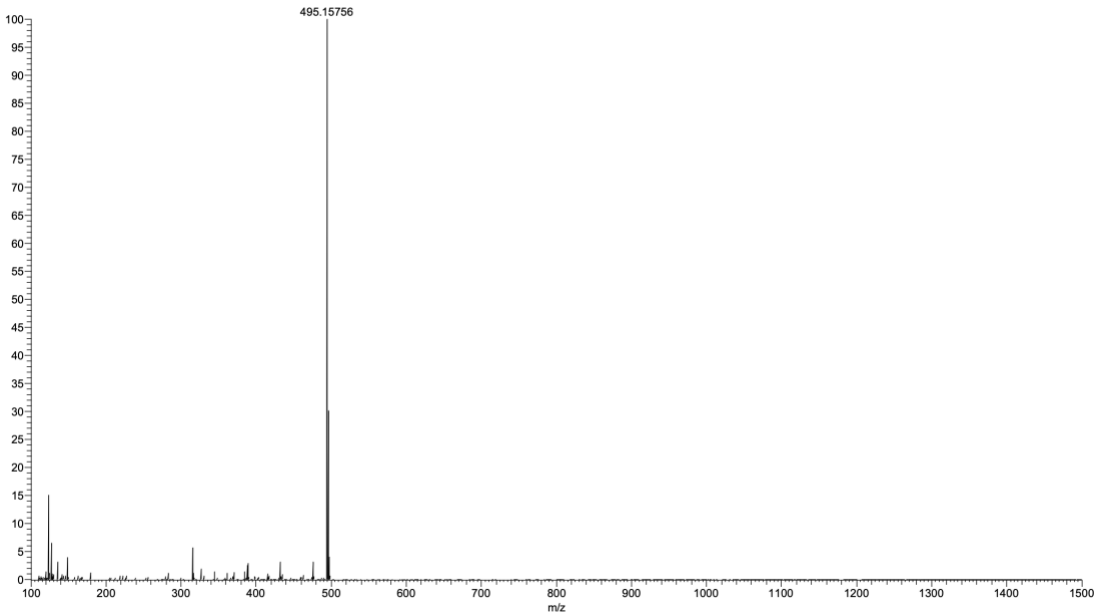

Figure C.4. Mass spectrum of TDAP.

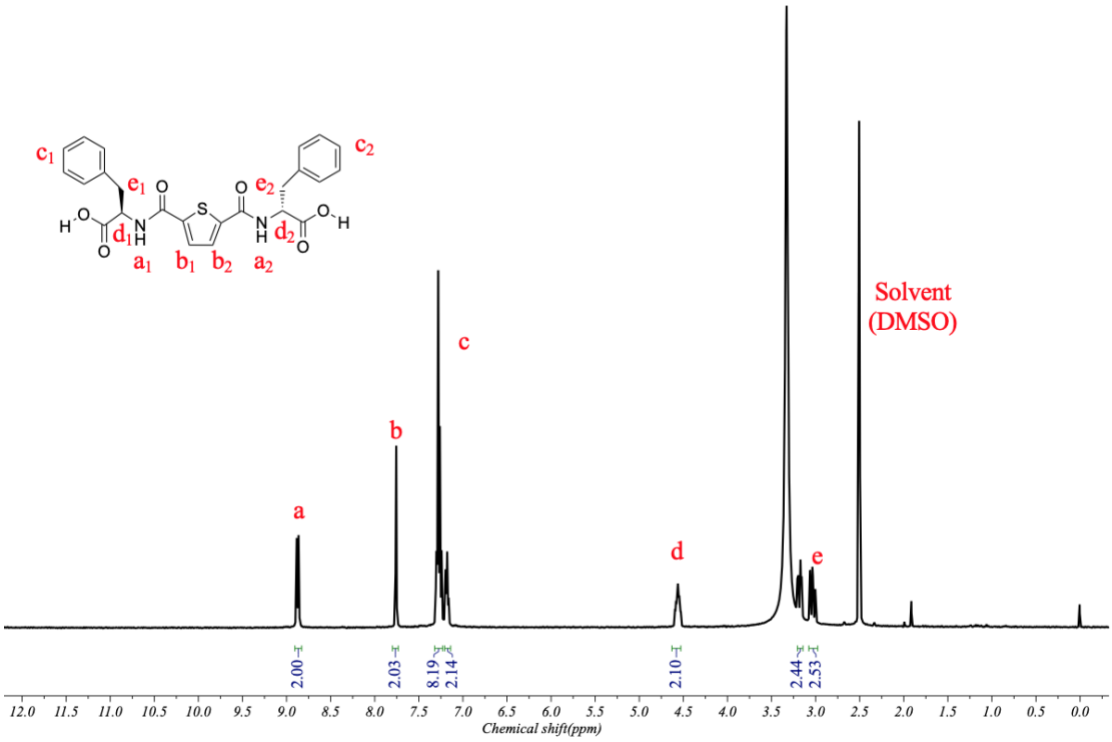

Figure C.5. ^{1}H NMR spectrum of *R*-TDAP-COOH in DMSO.

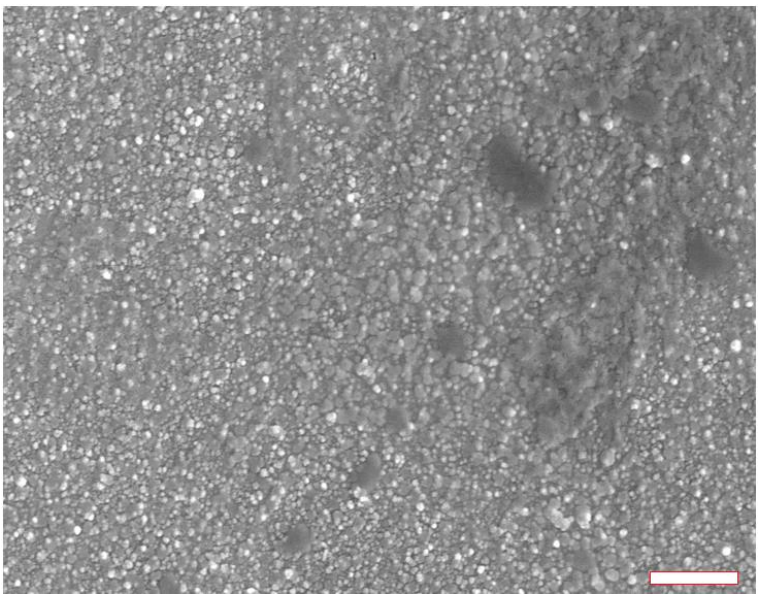

Figure C.6. SEM images of TDAP assembled architectures prepared from H_2O. Scale bars in the SEM images are 1 μm.

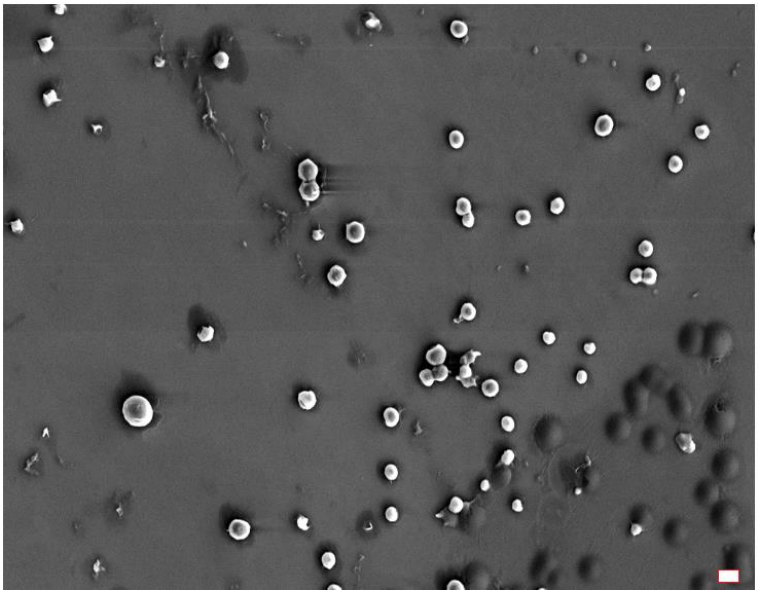

Figure C.7. SEM images of TDAP assembled architectures prepared from methanol/H_2O (1:1) mixtures. Scale bars in the SEM images are 1 μm.

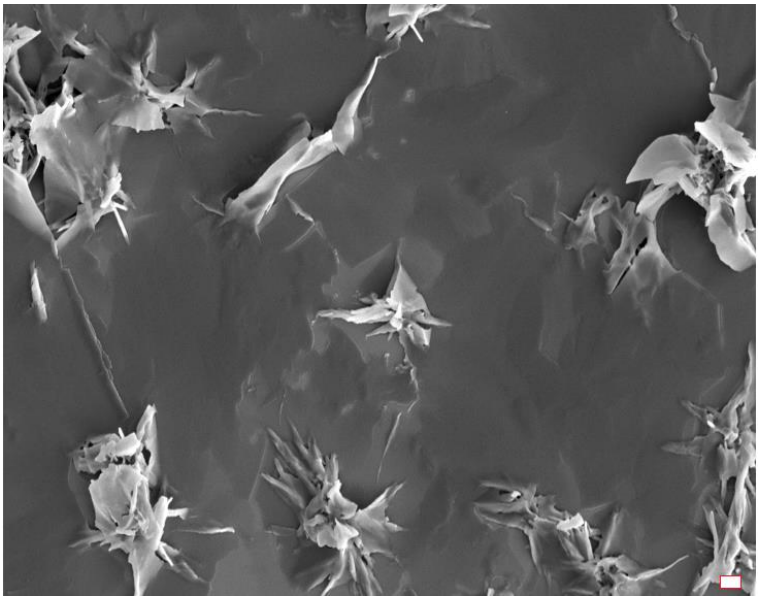

Figure C.8. SEM images of TDAP assembled architectures prepared from ethanol/H_2O (1:1) mixtures. Scale bars in the SEM images are 1 μm.

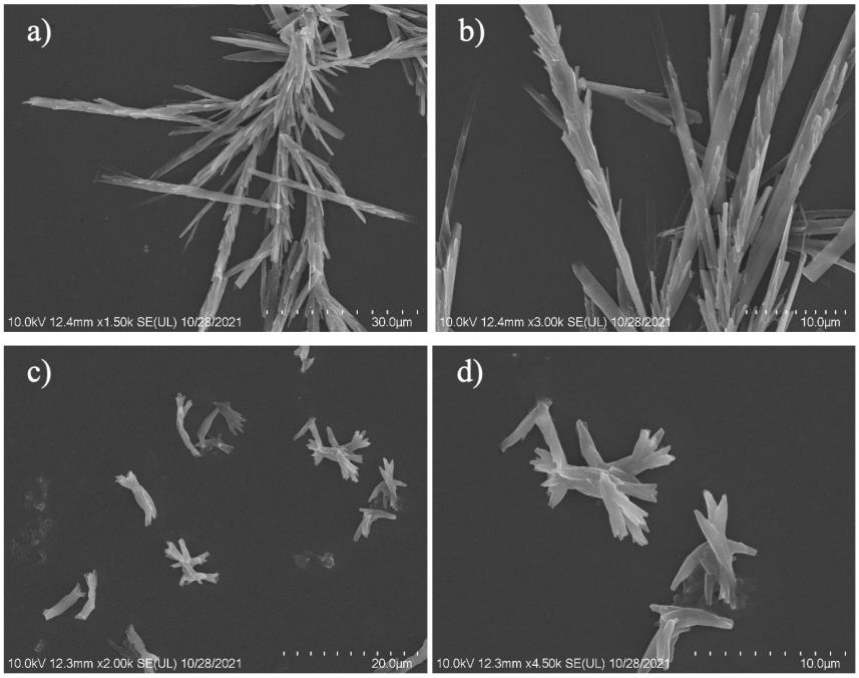

Figure C.9. SEM images of *R*-TDAP assembled architectures prepared from (a, b) methanol/H_2O (1:1); (c, d) ethanol/H_2O (1:1) mixtures.

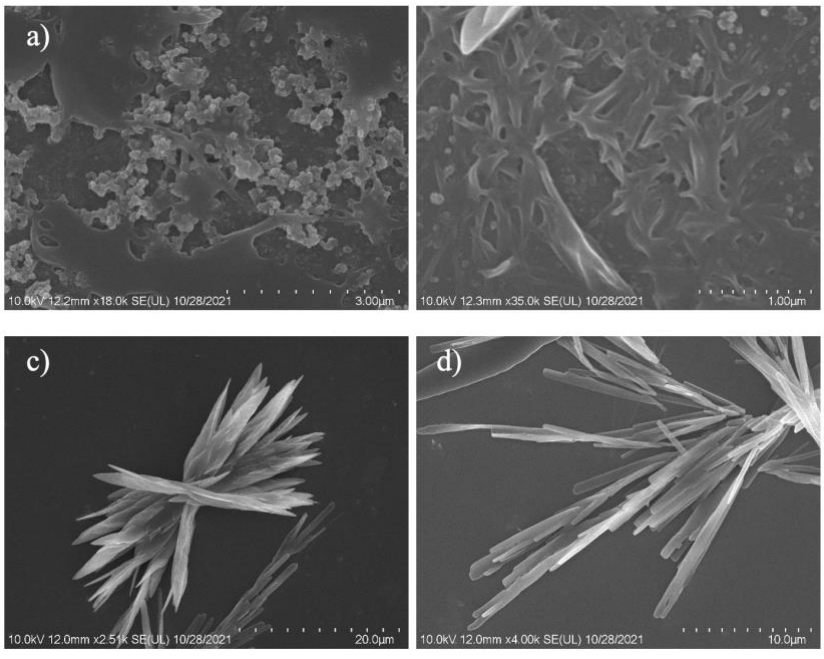

Figure C.10. SEM images of *S*-TDAP assembled architectures prepared from (a, b) methanol/H_2O (1:1); (c, d) ethanol/H_2O (1:1) mixtures.

Table C.1. Summary data of structural features.

Structural features	*R*-TDAP Helical fiber	*S*-TDAP Helical fiber	*Racemic*-TDAP Sphere	*R*+*S*-TDAP Sheet
Helical pitch (nm)	815	646	-	-
Diameter (nm)	326	237	871	-
Length (nm)	Longer than 4000	Longer than 4500	-	Longer than 3500
Width (nm)	-	-	-	689

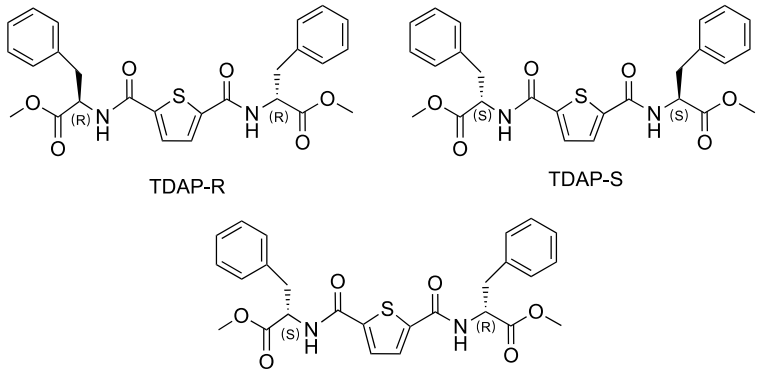

Figure C.11. Three different molecular configurations in racemate TDAP.

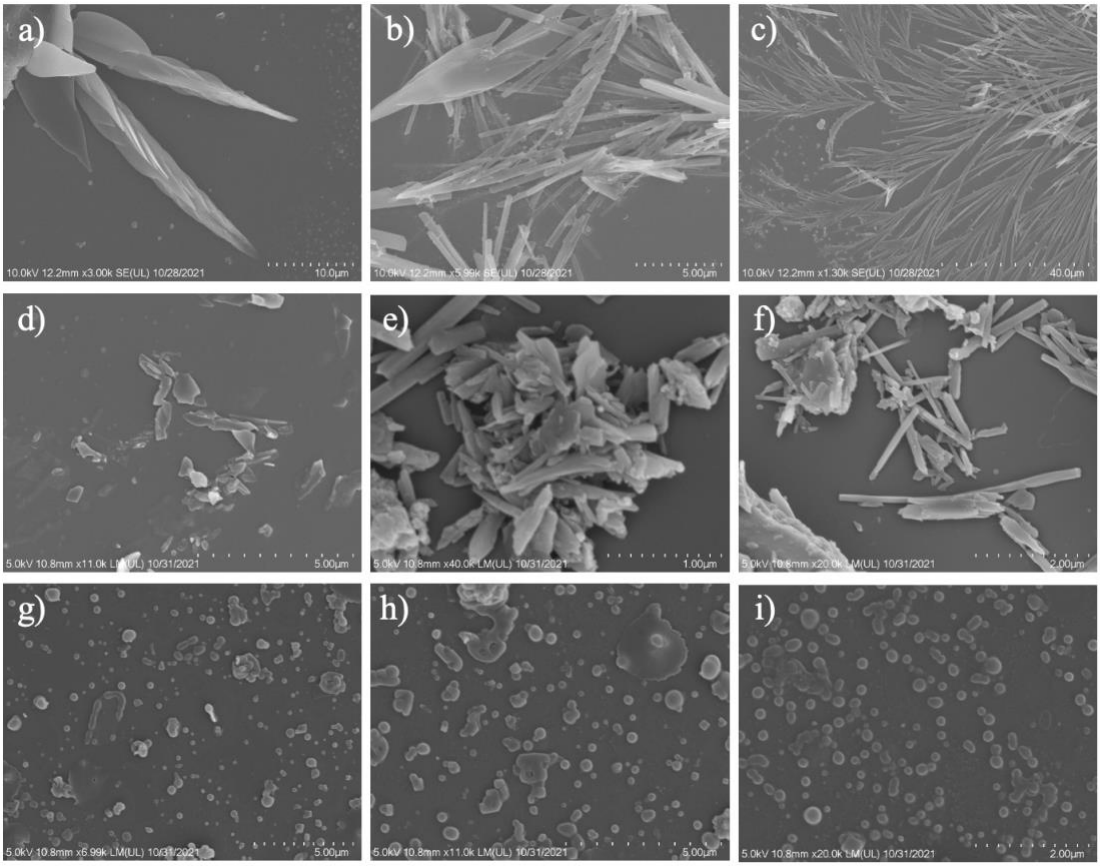

Figure C.12. Morphological changes of (a-c) R-, (d-f) R+S-, and (g-i) racemic-TDAP in the cooling assembly process at 80, 60, and 40 ℃.

Table C.2. Summary of crystal data.

Crystal data	***R*-TDAP**	***S*-TDAP**
Empirical formula	$C_{26}H_{26}N_2O_6S$	$C_{26}H_{26}N_2O_6S$
Color	colorless	colorless
Space group	$P\ 2_12_12_1$	$P\ 2_12_12_1$
Hall group	*P* 2ac 2ab	*P* 2ac 2ab
Crystal system	orthorhombic	orthorhombic
a (Å)	8.1251(4)	8.0945(11)
b (Å)	11.6987(5)	11.6955(15)
c (Å)	29.8910(13)	29.919(4)

Volume ($Å^3$)	2841.2(2)	2832.4(7)
Z	4	4
Dcalc. (g/cm^3)	1.297	1.301
F(000)	1176	1176
Temperature (K)	111	100

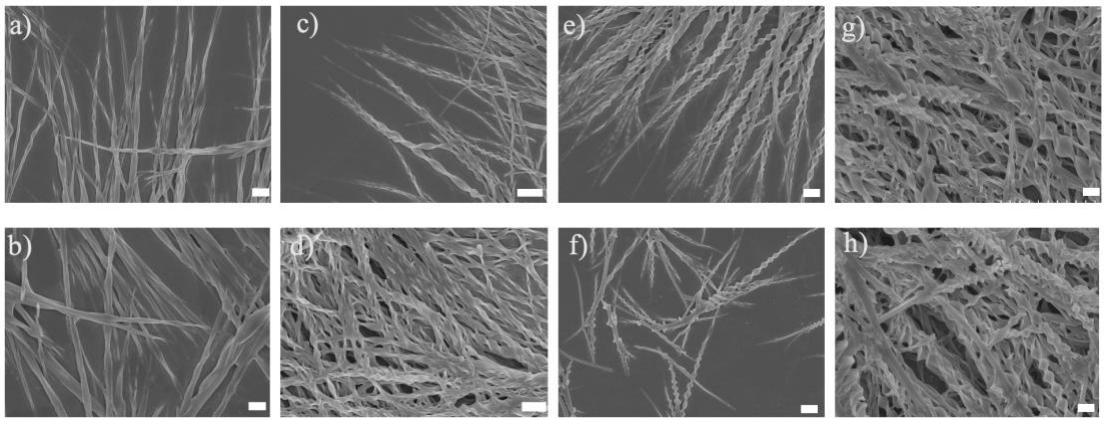

Figure C.13. SEM images of TDAP/MA at molar ratios of (a-b)1: 0.5, (c-d) 1:1, (e-f) 1:2, and (g-h) 1:3 co-assembled architectures. The concentration of *R*-TDAP-COOH in all samples was 0.5 mg mL^{-1}. Scale bars in the SEM images are 1 μm.

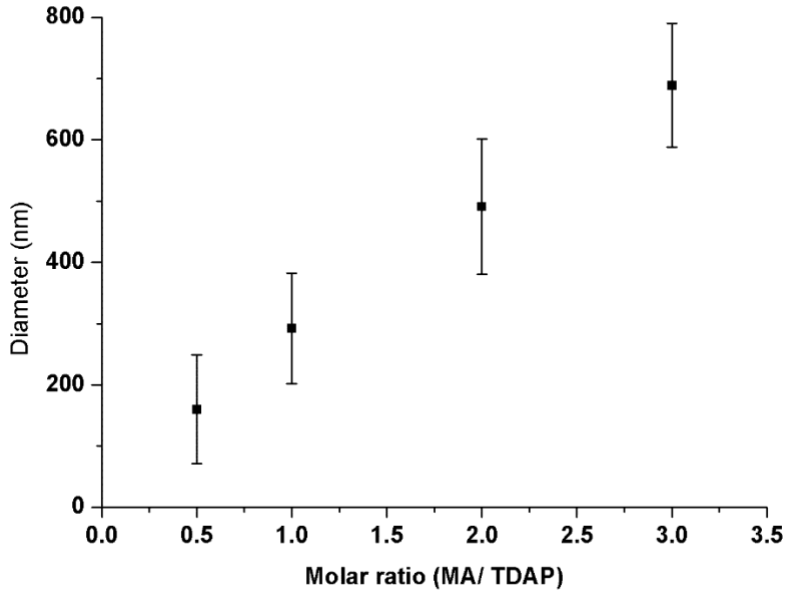

Figure C.14. Twist diameter of helical fibers of detecting system vs molar ratio of MA/TDAP formed in water.

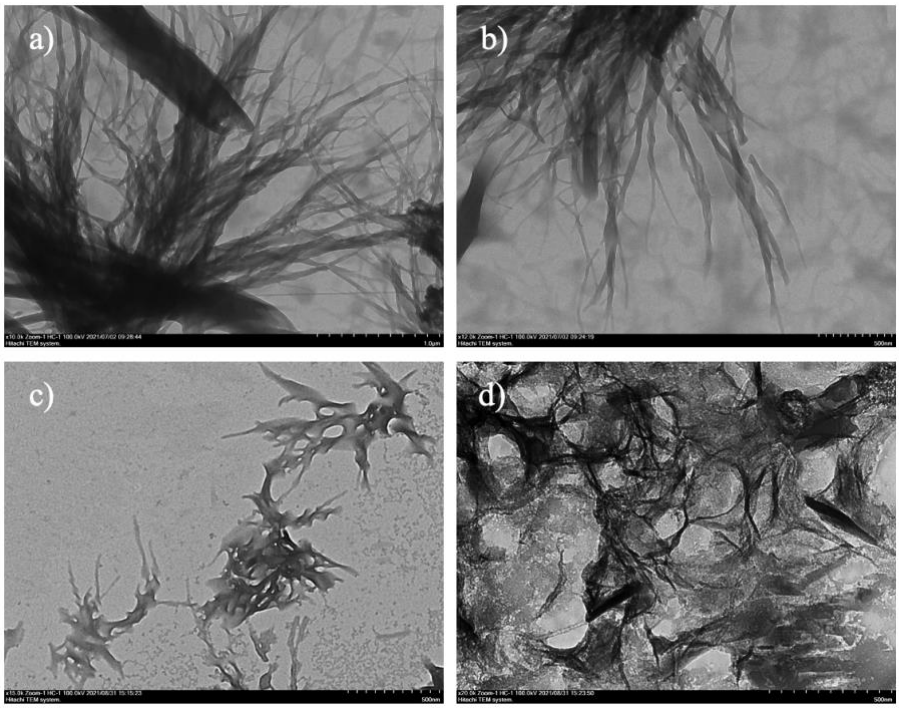

Figure C.15. TEM of SEM images of TDAP/MA co-assembled architectures formed at different concentrations. (a) 0.25 mg mL^{-1}, (b) 0.1 mg mL^{-1}, (c) 0.05 mg mL^{-1}, and (d) 0.01 mg mL^{-1}.

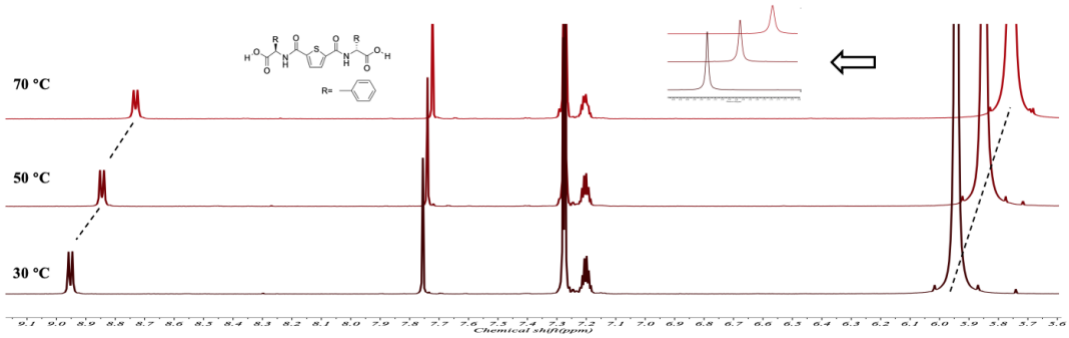

Figure C.16. Temperature-dependent ^{1}H NMR spectra of 1:1 MA/*R*-TDAP-COOH.

APPENDIX D Supplementary information for chapter 5

D.1 Supplementary data

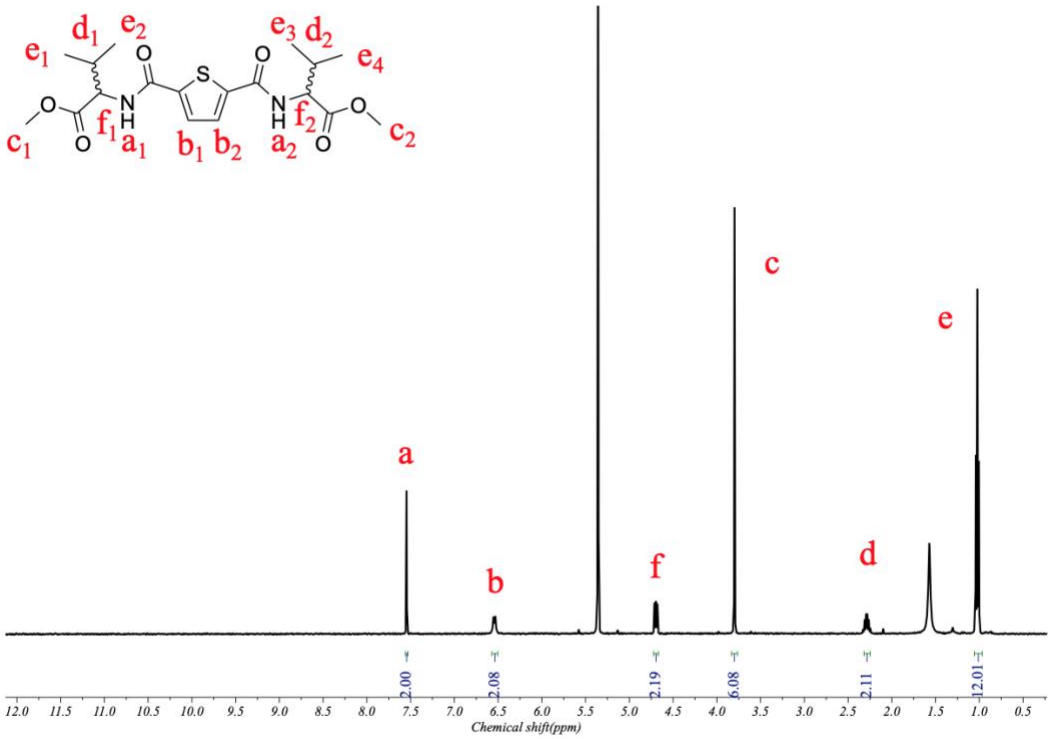

Figure D.1. ^{1}H NMR spectrum of TDAV in CD_2Cl_2.

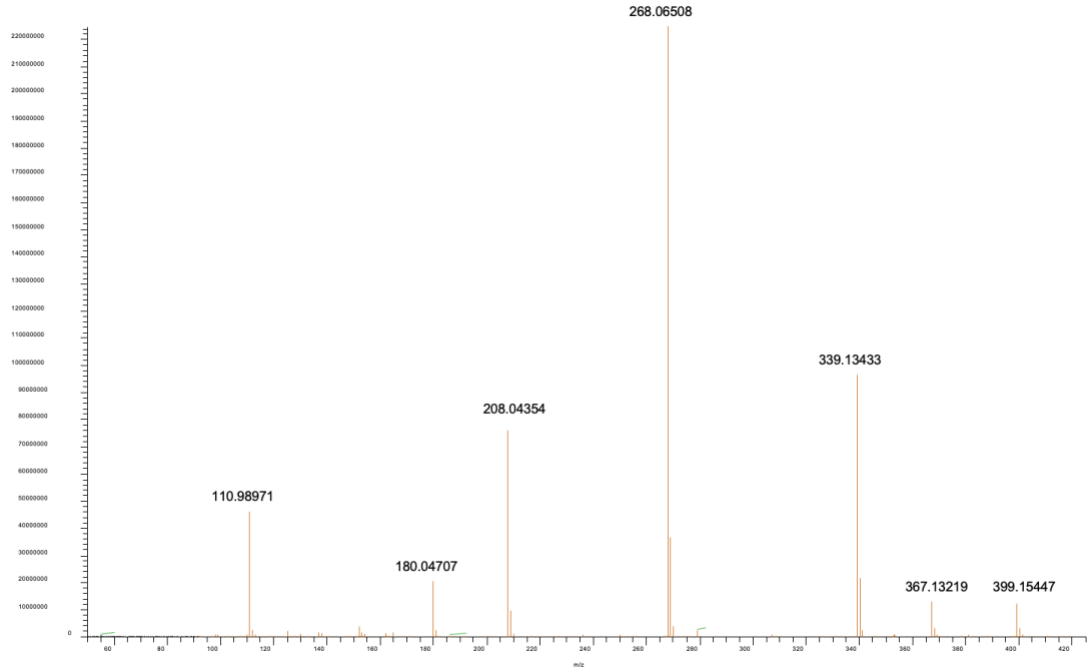

Figure D.2. Mass spectrum of *R*-TDAV.

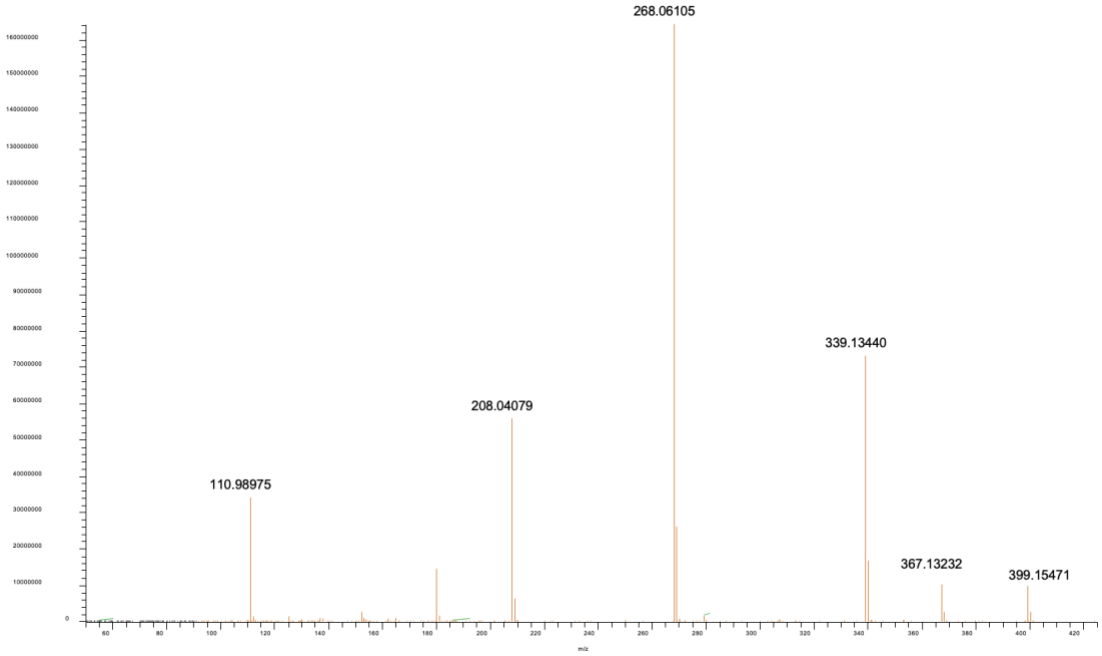

Figure D.3. Mass spectrum of *S*-TDAV.

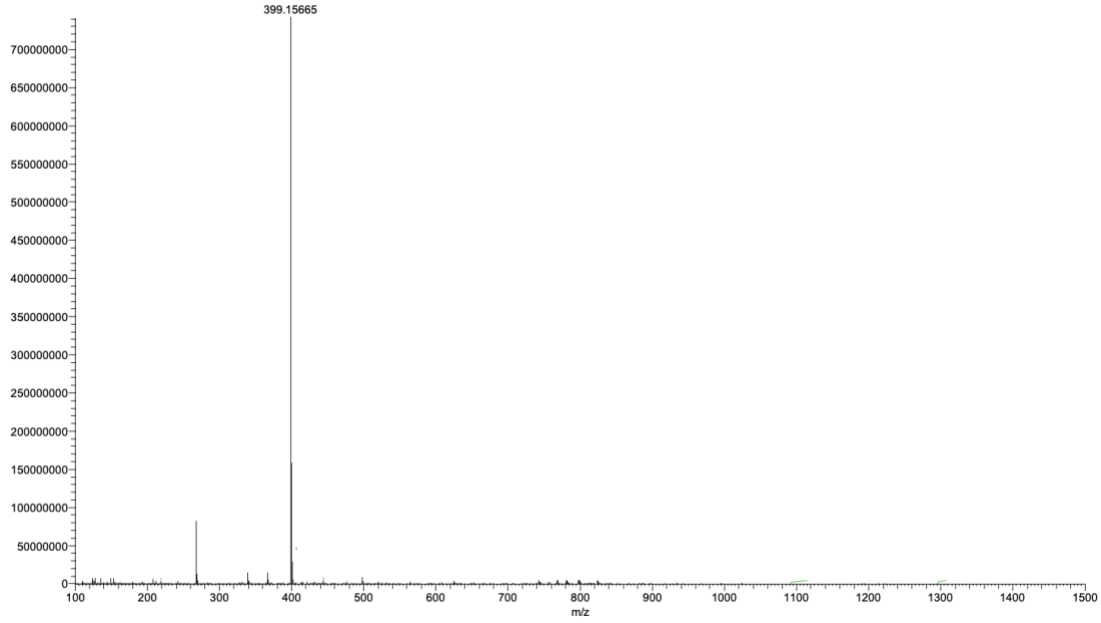

Figure D.4. Mass spectrum of TDAV.

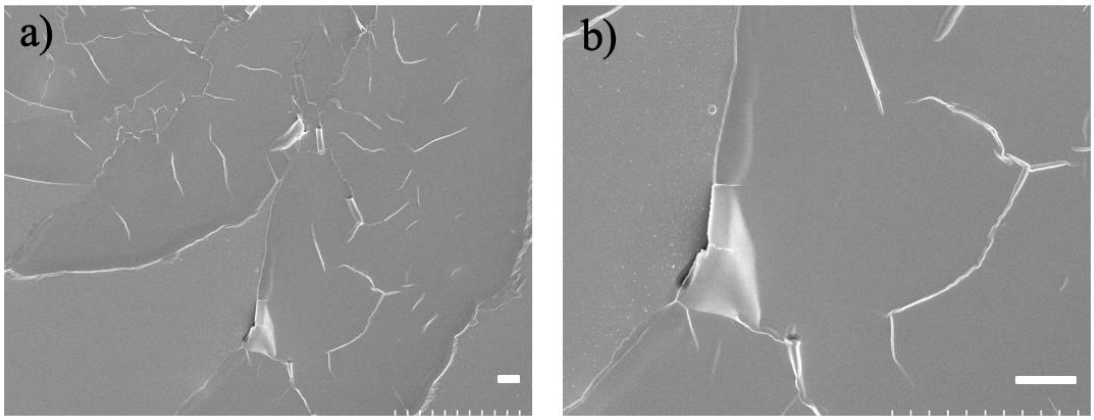

Figure D.5. SEM images of layer-like micelles prepared from *RS*-TDAV at 0.5 mg ml^{-1} cosolvent of methanol/H_2O (1:1). Scale bars in SEM photos are 10 μm.